MOLECULAR DYNAMICS STUDIES OF NANOSCALE EVAPORATION AND POOL BOILING HEAT TRANSFER ON MODIFIED SURFACES

By

RICARDO DIAZ

A dissertation submitted to the

School of Graduate Studies

Rutgers, The State University of New Jersey

In partial fulfillment of the requirements

For the degree of

Doctor of Philosophy

Graduate Program in Mechanical and Aerospace Engineering

Written under the direction of

Professor Zhixiong Guo

And approved by

_____

_____

_____

_____

New Brunswick, New Jersey

May 2018

ABSTRACT OF THE DISSERTATION

Molecular Dynamics Studies of Nanoscale Evaporation and Pool Boiling Heat Transfer on Modified Surfaces.

by RICARDO DIAZ

Dissertation Director:
Dr. Zhixiong Guo

Phase change has long been known to be an efficient method of heat transfer, due to the latent energy released at constant or near-constant temperature. Pool boiling in particular has been previously used to remove heat fluxes in excess of 1 MW/m^2. As technological advances continue to reduce the footprint of high power devices it is critical to investigate boiling heat transfer processes on the nanoscale, so that more efficient heat flux removal can be achieved. In the present work molecular dynamics (MD) is used to simulate various pool boiling scenarios in order to gain a better understanding of the critical factors affecting nanoscale heat transfer. In the first study the effect of hetero- and homogeneous wettability on nanostructured substrates is investigated to understand evaporation and heat flux characteristics. Results reveal that the substrates modified with hydrophilic nano-posts produce larger heat fluxes than heterogenous nanostructure/base wall combinations, due to enhanced kinetic energy transfer. A new coordination number criterion for liquid argon is developed to aid in tracking vapor atoms. The second study details the effect of contact angle and nanostructure pitch on maximum heat flux. Heat flux is found to increase with increasing pitch and decreasing contact angle, reaching an overall maximum of 159 MW/m^2. For larger pitches the superheat at which the peak heat flux occurs increases with both contact angle and pitch. In the final study single-layer graphene (SLG) topped substrates were simulated in the pool boiling of water. Results show improvements over plain substrates of 2-10x in heat flux values, which are on the order of 10 MW/m^2. CHF was also found to increase by as much as 14% with the addition of SLG, with lower superheats required to attain the CHF condition.

Acknowledgements

I would firstly like to thank my advisor, Dr. Zhixiong Guo, whose assistance allowed me to become a better researcher and more impactful communicator of ideas. His advice and guidance were invaluable and contributed greatly to the completion of this work. I would also like to thank the Rutgers Mechanical & Aerospace Engineering Department for the award of the Leeds Fellowship, which allowed me to conduct my studies and research. As well I would like to thank all the Professors in the MAE Department who, perhaps unknowingly, imparted their knowledge and passion to learn and grow onto me during my time here. Also, part of the material is based upon the work supported by the National Science Foundation under Grant No. ECCS-1505706, for which I am thankful. Much gratitude goes to my parents, Mr. and Mrs. José and Morbila Díaz, as well as my parents-in-law Drs. William and Maryam Hastings, for their continued moral (and sometimes child-care) support. Finally, I would like to dedicate this work to my family: my sons Miles and Kian, who find new ways to both challenge and delight me every day with their intelligence, humor, and curiosity, and my wife, Dr. Shirin Hastings, without whom I could not have achieved this. Her strength, drive, selflessness and compassion leave me constantly in awe, and I am truly lucky to have her by my side on our life's journey.

Table of Contents

List of Tables

List of Figures

Nomenclature

Symbol

A	Numerical constant
A_n	Constraint matrix
a, a_i	Acceleration, acceleration of atom *i*
B_{ij}	Bonding strength
b	3rd order derivative of position
C	Numerical constant
$C_{s,f}$	Empirical constant
c	Numerical constant
$c_{p,l}$	Saturated liquid specific heat at constant pressure
D	Vibrational density of states (VDOS)
d	Constant (±1)
d_{ij}	Bond strength
d_n	Number of dimensions
e_i	Per atom energy
F_i	Force on atom *i*
$F_{i,a}$	Angular constraint force on atom *i*
f	Frequency
f_c	Cutoff function
g	Gravitational constant
$g(r)$	Radial distribution function
g_d	Degrees of freedom

H	Hamiltonian function
h	Heat transfer coefficient
h_{fg}	Latent heat of vaporization
I	Identity matrix
KE	Kinetic energy
K_{ij}	Spring constant between atoms *i* and *j*
k	Thermal conductivity
k_{ijk}	Force constant between a triplet of atoms
k_B	Boltzmann constant
l_C	Lattice constant
M	Total system mass
N	Number of atoms
n	Integer constant
n_a	Active nucleation site density
P	Pressure
Pr_l^s	Saturated liquid Prandtl number
p	Momentum
Q	Thermostat strength
q'', q''_{max}	Heat flux, maximum attainable heat flux
q_i	Atomic point charge
R	Ideal gas constant
R_c	Cavity radius
r_c	Cutoff radius

r_i	Position of atom *i*
r_{ij}	Separation distance between atoms *i* and *j*
r_0	Equilibrium bond length
S	VDOS overlap
$S(r_{ij})$	Switching function
S_i	Per atom stress tensor
s	Empirical constant
s_t	Time-scaling variable
T, T_{sat}, T^0	Temperature, saturation temperature, desired temperature
t, δt	Time, timestep
U, U_a, U_b, U_i	Potential, angular, bond, and site potential energies
u_1	Generalized potential function
V	Volume
V_{ij}	Interaction energy
v	Velocity
W_{TC}	Tail correction energy

Greek Symbol

α	Stiffness parameter
Γ	Friction
ε	Potential well depth
ε_0	Dielectric constant
$\eta_i(t)$	Randomized force

θ, θ_0	Triplet angle, triplet equilibrium angle
λ_k	Lagrange multiplier
μ_l	Saturated liquid viscosity
ν	Hardness parameter
ρ_l, ρ_v	Liquid, vapor density
σ	Potential characteristic length
τ_T	Rise time
Φ_{ijkl}, Φ_0	Dihedral angle, dihedral equilibrium angle

Chapter 1

Introduction

1.1 Motivation

Heat transfer on both small and large scales is a vital area of research due to the ever-decreasing size of electro-mechanical components/devices and the accompanying increases in power density resulting from the rapid technological advances, especially of the last decade.[1-3] As applications requiring large power densities increase it is extremely important to remove excess heat as efficiently as possible.[4] As such a multitude of methods of large heat flux removal have been explored, including fin/pin heat sink designs, circulating liquids, etc. Heat removal involving phase change has long been another method under investigation[5] due to its ability to achieve fluxes on the order of 1 MW/m^2 and greater.[6] The phase change process, due to latent energy considerations, can store or release a large amount of energy over very small temperature variations. Thus boiling heat transfer, especially on the micro/nanoscale, is an excellent candidate for high power density applications, and merits further research in order to better understand the heat transfer process at these scales.[7] In particular, pool boiling heat transfer enhancement has long been investigated theoretically, experimentally, and numerically as a means of meeting the high heat flux removal requirements. Pool boiling is attractive due to its efficacy (ability for flux removal) and simplicity (ease of implementation).

1.2 Literature Review

Though the phenomenon of boiling has been observed and studied for at least hundreds of years (as early as Leidenfrost in the 18th century), it was not until more recently, the 1930's,[8] that its potential for large heat transfer at relatively low superheats was recognized and more actively pursued as an avenue of inquiry. Since then countless papers have been written on the subject, many of which concern the specific area of pool boiling heat transfer. Pool boiling occurs when an otherwise stagnant liquid is brought to the point of phase change by a submerged, heated surface. The phase change occurs when the liquid is superheated, i.e. the heating surface is maintained above the saturation temperature of the liquid ($\Delta T_{excess} = T_{surf} - T_{sat}$). Nukiyama[9] was the first to explicitly study the relation between heat flux and superheat, and generated some pseudo-boiling curves based on water boiling on various surfaces at atmospheric pressure. Later Farber and Scorah[10] provided an in-depth look at the different stages of pool boiling as related to Newton's Law of Cooling:

$$q'' = h\Delta T_{excess} \tag{1.1}$$

where q'' is the heat flux, h is the heat transfer coefficient (HTC), and ΔT is the excess temperature. The accompanying boiling (q'' vs. ΔT_{excess}) curve they produced was split into different stages:

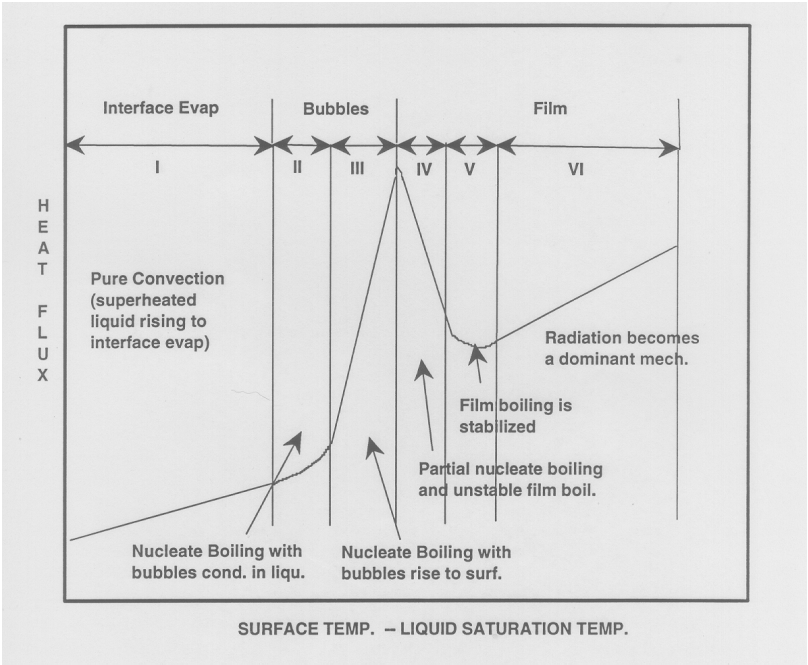

Figure 1.1: Pool boiling curve showing the different physical regimes.[11]

These different stages were observed by using a submerged cylindrical wire to heat water at various pressures. The first stage of boiling is characterized by low heat fluxes, where liquid near the heated wall rises to the top of the liquid and evaporates. In the next two stages (Nucleate Boiling) bubbles begin to form on the heated surface, then eventually coalesce and rise to the surface as jets or columns of gas. During these stages the heat flux rises exponentially until it reaches a maximum, or critical heat flux (CHF). As the superheat increases past the CHF point, the heat flux begins to drop rapidly due to the onset of film, or explosive, boiling. During these later stages the high superheat causes areas of the liquid nearest the heating surface to vaporize, inhibiting heat transfer and resulting in a heat flux minimum. Increasing the superheat past this point results in a stable vapor layer that blankets the entire heater surface, and the flux resumes its monotonic increase with superheat. With these stages now known, it was clear that the most useful (from an engineering standpoint) part of the curve was the area near the CHF,

whereby large heat fluxes could be achieved at low superheats. Thus it became important to be able to characterize the heat transfer between different heater surfaces and liquids. Rohsenow[12] presented one of the first and most successful correlations in 1951:

$$\Delta T = \frac{h_{fg}}{c_{P,l}} \mathrm{Pr}_l^s C_{sf} \left[\frac{q''}{\mu_l h_{fg}} \left(\frac{\sigma_{st}}{g(\rho_l - \rho_v)} \right)^{1/2} \right]^{1/3} \tag{1.2}$$

where h_{fg} is the latent heat of evaporation, $c_{P,l}$ is the saturated liquid specific heat at constant pressure, Pr_l^s is the saturated liquid Prandtl number, μ_l is the saturated liquid viscosity, σ_{st} is the surface tension, g is the gravitational constant, and ρ is the density, and C_{sf} and s are empirical constants. This correlation has its theoretical underpinning in bubble dynamics, i.e. the heat transferred by the bubbles that form on and then depart from the heater surface. Factors including bubble diameter, contact angle, and vapor pressure are important in the analysis, and are encompassed by the surface tension, density, viscosity, and specific heat values. Fritz' early work[13] on bubble departure diameter contributed greatly to Rohsenow and others' work of describing the nucleate boiling regime. Since nucleate boiling is dominated by bubble growth and departure, many subsequent works aimed to detail these processes directly. Plesset and Zwick[14] formulated an empirical expression for the growth rate of a spherical bubble in a superheated liquid layer before departure. This, however, could not fully describe heterogeneous bubble nucleation, as bubbles attached to a heater surface are not perfectly spherical and in fact change shape continuously, which alters the surrounding temperature field. Thus later work by Mikic et. al[15] attempted to correct this through use of a geometric factor, which correlates the actual bubble shape to a sphere. Correlations continued to be proposed for different geometries, most notably including horizontal and

vertical flat surfaces as well as cylinders. An early, useful relation for determining the critical heat flux also was presented by Lienhard and Dhir:[16]

$$q''_{chf} = 0.149 h_{fg} \rho_v^{1/2} [\sigma_{st} g(\rho_l - \rho_v)]^{1/4} \tag{1.3}$$

This correlation is not purely empirical, and uses dimensional analysis[17] and hydrodynamic stability analysis[18] as its theoretical basis. Tien[19] also worked to produce a hydrodynamic model for nucleate pool boiling based on stagnation flow. Two main assumptions/approximations of the model were that: 1) both isolated and non-isolated bubble columns produce an inverted axisymmetric stagnation flow field, and 2) the thermal boundary layer is uniform over the entire heating surface. Taking these approximations into account and fitting to previous experimental results for boiling water, the resulting correlation was:

$$q'' = 61.3 \cdot \mathrm{Pr}_l^{0.33} k \cdot n_a^{0.5} \Delta T \tag{1.4}$$

Here k is the fluid thermal conductivity and n_a is the active nucleation site density.

The work on bubble growth and departure is necessarily related to work that was simultaneously being done on bubble nucleation. Hsu[20,21] was able to describe the conditions for bubble nucleation over active cavities, as well as estimate the waiting period between bubble departure and new bubble nucleation. The cavity size limits for bubble nucleation were found to be dependent upon system pressure, thermal boundary layer thickness, degree of subcooling, and physical properties. At around the same time, Cooper and Lloyd[22] very importantly confirmed the existence of a liquid microlayer underneath nucleated bubbles, whose evaporation is important to the bubble growth/departure cycle and overall heat transfer. Many studies have gone on from this initial finding to look at microlayers, as well as the adjacent macrolayer and non-

evaporative film regions, and how their relationship with capillarity, disjoining pressure,[23] and bubble cycles[24] affect overall heat transfer. Demiray and Kim[25] used a microheater array to obtain temporally and spatially resolved heat transfer data, and found that bubbles departing the heated surface gain the most energy from the superheated liquid layer as opposed to the wall. They also found that transient conduction (during rewetting) and microconvection were the dominant mechanisms of heat transfer. Myers et al.[26] also used a microheater array and investigated heat transfer under a constant flux boundary condition. A finite-difference numerical simulation was also used in order to determine the instantaneous temperature distribution in the substrate, which facilitated the computation of substrate conduction. Corroborating Demiray and Kim, they found that most of the energy necessary for bubble growth was drawn from the superheated liquid layer, and that only ~23% of the heat transferred from the substrate could be attributed to three-phase contact line heat transfer and microlayer evaporation. Once again transient conduction was determined to be a major mechanism for heat transfer, during the rewetting process after bubble departure. Kim et al.[27] determined a similar result when the bulk liquid was superheated, determining the ratio of measured wall heat transfer to energy required to grow the bubble to be ~0.5. However as the bulk temperature was decreased to saturated and subcooled conditions the ratio increased to a maximum of ~3.6, meaning that below saturation temperature the wall supplies more than enough heat to promote bubble growth.

In line with Hsu's work on bubble nucleation over cavities, many investigations have sought to correlate the related concepts of surface roughness and contact angle (both of a liquid droplet and vapor bubble) to overall heat flux q''. Costello and Frea[28]

measured the heat flux on submerged cylinders covered in different levels of mineral deposits, and found that the presence of deposits led to as much as a 50% increase in CHF over the clean cylinders. Gaertner[29] performed boiling experiments on surfaces covered in varying levels of grease, as well as a non-wetting fluorocarbon film (~180° contact angle). The nucleated bubbles were found to remain on the heated surface (instead of departing) and eventually coalesce, blanketing the surface in vapor. Thus hydrophobic surfaces (i.e. increasing contact angles) were found to dramatically lower CHF values, while more hydrophilic surfaces increased them. This effect was eventually incorporated into other models, including a theoretical model proposed by Kandlikar[30] in 2001 that includes both hydrodynamic and non-hydrodynamic effects. Later experiments have continued along this line to characterize nanoporous surfaces,[31] which also tend to increase heat transfer while reducing the superheat required. This is because of their increased number of small cavities, which are able to trap vapor and improve bubble nucleation rates. This was also found to be the mode of heat transfer enhancement in nanofluids.[32,33] As a fluid with suspended nanoparticles is boiled, many of the nanoparticles are deposited onto the heater surface and form a porous layer. After boiling, these nanoparticle-deposited surfaces were found to have increased wettability characteristics (reduced contact angle, increased surface roughness), which in turn improved CHF characteristics.

When the capabilities of small-scale manufacturing techniques were improved enough to reliably create micro/nanostructures, pool boiling could be carried out on these surfaces to determine their effects on wettability, CHF, etc. Mitrovic and Hartmann[34] created a surface covered in cylindrical microstructures to boil R141b, and found an

increase in heat transfer for all microstructured surfaces over the plane surface. Wei et al.[35] investigated the boiling of FC-72 on a Si substrate covered in square cross-section micropin arrays. They found that CHF increased with pin height, and obtained a ~4x increase in CHF over a smooth substrate. Vapor bubbles nucleated at the base of the micropin and grew within the confined region before moving to the top of the pin to grow further, and finally depart. Cooke and Kandlikar[36] also investigated pool boiling on Si chips, but with structured microchannel surfaces, and found a >3x enhancement of the HTC. Bubbles were found to nucleate at the bottom of the channels before moving to the top of the channel to grow and depart. The geometry allowed the bottom of the microchannels to remain flooded with water preventing dryout. Ahn et al.[37] investigated pool boiling on Si substrates covered with multi-walled carbon nanotubes. They found that the addition of nanotube forests enhanced CHF, as well as the amount of superheat required (over the bare substrate case). They also found that 25-μm forests increased flux values more than 9-μm forests, across all regimes of boiling. Hendricks et al.[38] looked at nanostructured Al and Cu surfaces and found increased CHF values, while superheat values were decreased. This, along with other studies,[39] went against conventional pool boiling theory, which predicted an increase in the superheat required to nucleate bubbles when surface cavities reached sizes on the order of nanometers. For example, the relation given by Theofanous et al.:[40]

$$R_c = \frac{2\sigma_{st} T_{sat}}{\rho_v h_{fg} T_{surf}} \tag{1.5}$$

where R_c is the cavity radius, ends up requiring >300 K superheat for a 100 nm cavity size. This does not reflect empirical results, however, as nanobubbles have been observed at low superheats in previous experiments.[41] It has also been found that the

introduction of nanocavities and/or nanostructures reduces the bubble departure diameter and increases the bubble nucleation rate. This has the overall effect of enhancing heat dissipation from the surface and reducing wall superheat.[42] Weibel et al.[43] characterized evaporation and boiling on sintered Cu powder wick surfaces. They achieved fluxes greater than 500 W/cm^2 without dryout, and found that there was an optimum particle size that reduced thermal resistance due to a balance of heat transfer area and resistance to vapor flow out of the wick.

Closely related to surface roughness is the issue of contact angle, or wettability. Chowdhury and Winterton[44] tested the effect of contact angle on pool boiling of various Cu and Al specimens. They found that heat transfer increased with decreasing contact angle (as well as increasing microscale surface roughness). However, they found that most of the increase occurred in the transition region (between the CHF and minimum flux points). Maracy and Winterton[45] confirmed the increase of CHF with decreasing contact angle, and observed a heat flux hysteresis between heating and cooling, with heating producing higher fluxes. Wang and Dhir[46] investigated boiling on vertical Cu surfaces with microscale roughness. Interestingly, they found that an increase in wettability led to a decrease in active nucleation sites on the surface. This is a similar result to Grigoriev et al.,[47] who when boiling cryogenic liquids observed a reduction in HTC. Because cryogenic liquids have a near zero contact angle they almost completely wet the surface and therefore reduce the possible number of nucleation sites. Only making the surface significantly rougher can reduce this effect. Ahn et al.[48] investigated water boiling on surfaces with micro, nano, and both micro- and nanostructures, and found an increase of CHF with decreasing contact angle. This was attributed to the

increased wettability as well as improved liquid spreading due to the structured surface. The combined micro- and nanostructured substrate showed the greatest overall CHF. The Hendricks study mentioned previously,[38] which looked exclusively at nanostructured surfaces, found that there was an optimal contact angle ~20° that maximized CHF, while moving to lower contact angles actually decreased heat transfer. Thus it is clear that contact angle and surface roughness are interlinked, but the way in which they work in tandem to affect heat transfer and the heat transfer coefficient is complex. Taking some of these results into account, Betz et al.[49] combined hydrophilic and hydrophobic zones (with different pitches) on a surface, to try to take advantage of the properties of both. They found that the hydrophilic (SiO_2) surfaces topped with hydrophobic (Teflon) islands had a significantly higher CHF than the hydrophobic surfaces topped with hydrophilic islands. The mostly hydrophobic surfaces even showed lower CHF than the plain SiO_2 (purely hydrophilic) wafer in certain cases. In addition, increasing wettability improved CHF across all cases. However, the mostly hydrophobic surfaces exhibited the highest HTC values, followed by the mostly hydrophilic surfaces, and finally the plain wafer. In general the bubble nucleation occurred at the interface between hydrophilic and hydrophobic areas, as these regions would aid in both initial vapor nucleation as well as rewetting after bubble departure. Jo et al.[50] also looked at boiling water on mixed hydrophilic and hydrophobic zones, and compared the results to those of purely hydrophobic and hydrophilic substrates. The mixed surface (hydrophilic base covered with hydrophobic dots) had an improved heat transfer coefficient over both pure substrates with a CHF as large as that of the hydrophilic surface. At low fluxes the pitch and diameter of the hydrophobic dots play a significant role in heat transfer, while at high

fluxes the diameter and number of dots dominate. The ratio of hydrophobic area to total heating area was found to be insignificant. Also, increased dot diameter resulted in earlier onset of nucleate boiling, while decreased pitch distance increased bubble interaction and coalescence.

Most recently works have sought to expand upon earlier heat transfer results via numerical simulation. Given the micro/nanoscale nature of many aspects of boiling heat transfer (bubble nucleation, microlayer evaporation, surface roughness, etc.) design and observation of experiments can be difficult. Numerical simulation has proven a valuable tool in investigating these small-scale phenomena, and can offer flexibility of system setups and control that would be hard to reproduce experimentally. As computational power and efficiency has advanced, Molecular Dynamics (MD) has become one of the most often used simulation techniques, and the capabilities of MD simulation will continue to expand as computing power advances.

Maruyama et al.[51] numerically simulated pool boiling, and by using the experimental variation of initial thickness of the macrolayer with wall superheat, was able to reproduce the boiling curve. By assuming a random initial spatial and size pattern of vapor stems, they were able to simulate vapor growth and macrolayer decay with a 1-D heat conduction model. Later, Maruyama et al.[52] used MD to simulate heterogeneous bubble nucleation on a solid surface. To nucleate a vapor bubble, ~5500 liquid Ar atoms were first placed between two parallel solid walls and brought to equilibrium. After equilibrium the walls were slowly expanded until the pressure was reduced enough to nucleate a bubble, after which the wall expansion was stopped in order to view the equilibrium structure and properties of the bubble. They found increased bubble size and

nucleation pressure with decreasing surface wettability. Son et al.[53] also simulated a growing and departing bubble on a horizontal surface. They used a finite-difference scheme to solve the mass, momentum, and energy equations and divided the domain into micro and macro regions. The microlayer was found to contribute ~20% to the overall heat flux, and the predicted bubble growth matched well with experimental data. A related study by Son et al.,[54] using the same simulation technique, simulated the vertical bubble merging process from a single nucleation site. They found that bubble merging does not significantly influence the wall heat flux or bubble departure diameter. Also, the vapor removal rate tended to decrease as the waiting period between nucleation events decreased, due to bubble merging. Finally, the vapor removal rate increased linearly with superheat. Mukherjee and Dhir[55] simulated lateral bubble merging, by solving the incompressible Navier-Stokes, mass, and energy equations, and found that lateral merging resulted in a larger vapor removal rate than single bubble nucleation. A liquid layer was found to be trapped between the vapor bases during merging, and as the bubbles departed this liquid provide rewetting, resulting in higher overall heat transfer. A study by Maruyama et al.[56] looked at the nanoscale solid-liquid contact of a liquid droplet on a horizontal surface via MD. They found a layered structure in the droplet parallel to the solid surface, and that the density at the core of the droplet approached that of the macro bulk liquid density. The solid wall was seen to have little or no influence at the liquid-vapor interface, though the solid-liquid interaction potential influenced the nanoscale contact angle, as would be expected.

Sarkar and Selvam[57] used MD to simulate the thermal conductivity of nanofluids. The thermal conductivity of a base (Ar) fluid and nanofluid (Cu, under varying particle

loads) was computed, and it was found that conductivity increased with volume percentage of nanoparticle loading. The conductivity enhancement was more pronounced at low volume fractions (0.4%) before becoming more linear at higher loadings. The conductivity enhancement was attributed to an increase in liquid atom motion due to the nanoparticle presence. A similar result was found by Li et al.,[58] however they observed adsorbed liquid particles at the solid-liquid interface, which results in liquid layering. This layer around the nanoparticle was more ordered and had a higher density than the bulk liquid, which was thought to have contributed to the increase in thermal conductivity. Merabia et al.[59] also found this liquid layering for nanoparticles heated moderately above the surrounding liquid boiling temperature. The temperature profile, however, was relatively steep near the nanoparticle surface, corresponding to a drop in local effective conductivity. At higher temperatures the layering and liquid density near the particle decreased significantly, while at the same time the pressure near the particle increased. Whereas on a flat surface the vapor layer formed after CHF has a pressure at or near the surrounding system pressure, the increased pressure in the nanoparticle case prevents the formation of a vapor sphere around the particle. This essentially delays the CHF condition, and the CHF value for the nanoparticle case was found to increase by a factor of 4 over the flat wall case.

In addition to bubble nucleation and nanofluid heating, many MD simulations have been performed to study phase change heat transfer, including pool boiling under various conditions, and on various substrates. Yasuoka and Matsumoto[60] simulated homogeneous nucleation (of liquid droplets from the vapor phase) in water with a heated carrier gas (Ar), and found a nucleation rate three orders of magnitude smaller than

classical nucleation theory. Water molecule cluster formation and size was also investigated, and seen to have a significant effect on surface tension. Yi et al.[61] simulated the vaporization of a thin (2 nm) Ar film on a Pt substrate. They found results in agreement with the general macroscopic pool boiling theory: at low wall superheat ($T_{surface}$ = 150 K) a normal evaporation process took place, while at high wall superheat (300 K) a vapor layer blanketed the Pt surface and forced the liquid film upwards. As it traveled upward the liquid film deformed and took on a more spherical droplet shape. Once the wall temperature was reduced the liquid condensed and reconstituted the original liquid film. Nagayama and Tsuruta[62] used MD simulation along with theoretical considerations to formulate a new expression for the condensation coefficient. In their simulations they found that the transition state for condensation occurs in the liquid-vapor interphase zone, and that an energy barrier exists in the condensation process. The evaporation coefficient was investigated via MD by Yang and Pan,[63] using 1000 water molecules. They found the interphase region thickness increased linearly with temperature, and that its mean temperature was lower than that of the bulk liquid, although with much greater temperature fluctuation. Also, hydrogen bonding within the interphase region was thought to reduce evaporation at low temperatures. Maroo and Chung[64] simulated a thin Ar film on a horizontal Pt surface to observe the evaporation process. The system was equilibrated at 90K, then the temperature of the Pt wall was raised to 130 K, and transient evaporation was allowed to occur. High heat flux (~600 MW/m^2) and evaporation rates (4200 kg/m^2s) were recorded, and a non-evaporating layer of Ar fluid was seen to have adsorbed on the Pt substrate. This layer was thought to have an insulating effect and inhibit heat transfer, and its thickness was dependent upon the

pressure and height of the domain, as well as the substrate temperature. Zou et al.[65] used MD to simulate the homogeneous vapor nucleation in explosive boiling induced by laser heating, in both water and liquid nitrogen. For water they found a 66-78% conversion ratio (i.e. heat added converted into potential energy for bubble nucleation), while the remaining heat raised the system temperature. Increasing the heating zone area, as well as the initial equilibrium temperature, increased bubble growth. Liquid nitrogen had a higher conversion ratio and thus a higher potential for bubble nucleation. The Coulombic interaction of water forms stronger bonds between molecules, which in turn makes bubble nucleation more difficult. Morshed et al.[66] simulated pool boiling of liquid Ar on a Pt substrate structured with nanoposts. Three different nanopost heights were investigated (in addition to an unstructured surface), and both evaporation and explosive boiling were considered. The evaporation rate increased for all nanostructured substrates, and the longest nanoposts resulted in the greatest overall heat transfer enhancement. During explosive boiling no non-evaporative film was observed, and the separation temperature (ie. the temperature at which the liquid film is ejected from the substrate due to vapor layer formation) was seen to depend significantly on nanopost height: when the nanoposts were at or above liquid level the separation temperature increased sharply (which implies a delay in the onset of the film boiling condition). Seyf and Zhang[67] studied normal and explosive boiling of an Ar film on a Cu plate with spherical nanostructures. The heat transfer was found to increase due to the increased surface area of the nanostructures. During explosive boiling no adsorbed layer was left on the substrate, and the separation temperature once again increased with nanostructure size. Also, as the liquid was ejected from the substrate the smaller size nanostructures resulted

in larger ejected droplet sizes. Hens et al.[68] looked at various scenarios of liquid Ar boiling on a flat Pt substrate. In one scenario the wettability (hydrophilic, hydrophobic, or neutral) was altered and Ar was heated to both 150 K and 250 K. At 150 K, for the hydrophobic and neutral surfaces only evaporation was found to take place, while interestingly the hydrophilic surface resulted in more explosive boiling due to better heat transfer from substrate to liquid. More vigorous boiling occurred at 250 K, although the temperature rise was not enough to move the hydrophobic case out of the evaporative regime. In another scenario the substrate was divided into hydrophilic and hydrophobic halves, and used to heat Ar to various temperatures. At both low (100 K) and high (250 K) temperatures the substrate patterning appeared to have no effect, however at an intermediate temperature of 150 K atoms some effect was observed. On the hydrophilic half atoms were heated and began to boil in an explosive manner while atoms over the hydrophobic half showed less intense boiling, hinting at the role of heterogeneous wettability in vapor nucleation. Maximum fluxes in this study were found to be on the order of 10^8 W/m^2, in line with the predictions of kinetic evaporation theory. Wang et al.[69] simulated sub-cooled boiling of water on Cu substrates. Different superheats (ΔT_{excess} between 2 K and 52 K) as well as substrate shapes (flat, cuboid nanostructures, finger-shaped nanostructures) were investigated. For low superheats nanoscale vapor nuclei were found to generate randomly, but condense before bubble growth can occur. At higher superheats the nanobubbles aggregate and coalesce through different processes, depending on the surface structure. For flat surfaces nanobubbles merged horizontally without hindrance, leading to earlier formation of the heat transfer inhibiting vapor layer. When nanostructures were present, however, a vertical nano-convection was observed

that delayed vapor layer formation and affected the hydrodynamic instability of the vapor, leading to higher overall heat flux. The maximum heat flux for the nanostructured surfaces was ~13 GW/m^2, while the flat surface only reached 9 GW/m^2.

By now it is clear that pool boiling (and related phenomena) has a long and rich history of research and investigation. Over the course of many decades countless theoretical, experimental, and numerical studies have been carried out in order to gain further insight into the phase change process. As with all scientific endeavors, as experimental and computational capabilities improve the knowledge previously gained can continue to be built upon and refined. At the same time, as technological advances are made, especially in the MEMS/NEMS and high power electronics realms, the physical volumes of interest for heat flux removal continue to trend toward the micro- and nanoscales. This trend means it is ever more important to study nanoscale pool boiling so that we can better understand the physical characteristics and mechanisms of heat transfer on small scales. This will allow us to better design small-scale heat removal systems, and can also help provide links between nanoscale heat transfer and macro-scale phenomena to form a more holistic understanding of boiling processes. Within nanoscale boiling heat transfer there are still many issues to address and build upon, including the nature of nanoscale bubble nucleation, critical heat flux, vapor layer formation, contact angle, etc. In pool boiling these issues are necessarily dependent upon substrate characteristics such as wettability, nanostructure size/pitch, thermal conductivity, and thermal resistance, amongst others. This work attempts to discern relevant trends and provide clarity on many of these issues in order to meaningfully contribute to the ever-growing body of research of pool boiling.

Chapter 2

Molecular Dynamics

2.1 Overview

Molecular dynamics (MD) simulation is a powerful method used for investigating the behavior of atoms and molecules. Beginning from a framework of either quantum or classical Newtonian mechanics, the velocities and trajectories of atoms can be determined and used to calculate various properties (pressure, temperature, density, etc.) of systems. With the improvements in processor speeds and parallel processing that have come about in recent years the capabilities of MD simulations has also improved, allowing for larger (greater number of particles), longer (greater number of timesteps), and/or more complex simulations with higher fidelity. Applications of MD are wide-ranging, with many in the fields of materials science, biophysics/chemistry, fluid mechanics/heat transfer, etc. The atomic length scale of MD also naturally lends itself very well to emerging nanoscale fields, allowing investigation of both short length and timescales difficult (or impossible) to reproduce experimentally. Much like scientific experimentation, MD simulation also allows different system parameters and controls to be specified in order to focus on particular properties of interest, though in the case of MD the control can be more finely tuned. In general, MD is an extremely useful computational tool that serves as a bridge between the theoretical and experimental domains, both able to use theoretical formulations to reliably simulate natural processes, and mimic experimental setups/use empirical data to refine theoretical models.

Ab initio (quantum) MD begins from the Schrödinger equation, whereas classical MD uses Newtonian mechanics (as the investigations in this work use classical MD, only

these formulations will be discussed). Thus for classical MD the starting point is the following equation:

$$\mathbf{F}_i = m_i \mathbf{a}_i = m_i \frac{d^2 \mathbf{r}_i}{dt^2} \tag{2.1}$$

which is the equation of motion for particle i. F_i is the atom force vector, m_i the atomic mass, a_i the atom acceleration, and r_i the atom position. The atomic positions and velocities at the beginning of a simulation are generally handled via setting of initial conditions, which leaves forces between atoms in need of calculation. To do this we first need a potential function in order to describe the interactions between atoms. The total potential U of a system is given by:

$$U = \sum_i u_1(\mathbf{r}_i) + \sum_i \sum_{j>i} u_2(\mathbf{r}_i, \mathbf{r}_j) + \sum_i \sum_{j>i} \sum_{k>j>i} u_3(\mathbf{r}_i, \mathbf{r}_j, \mathbf{r}_k) \ldots \tag{2.2}$$

where u_1, u_2, etc. are generalized potential functions based on atom positions. The first term captures any external effects (e.g. boundary wall interaction), while the remaining terms represent atom-atom interactions. Recalling the relation

$$\mathbf{F_i} = -\nabla_i U \tag{2.3}$$

and combining with Eq. 2.1 we have for each atom:

$$-\frac{dU}{d\mathbf{r}_i} = m_i \frac{d^2 \mathbf{r}_i}{dt^2} \tag{2.4}$$

From this basic framework the forces, positions, velocities, and acceleration of all atoms in a simulation can be calculated, and used to extract other properties of the system (e.g. density, pressure, temperature).

2.2 Potential Functions

2.2.1 Two-Body Potentials

The most commonly used potential is the two-body (or pairwise) potential, since as potentials take larger and larger numbers of atoms into account they become more computationally expensive. Some of the first and simplest approximations used were the hard sphere and square-well potentials, shown in Figure 2.1:

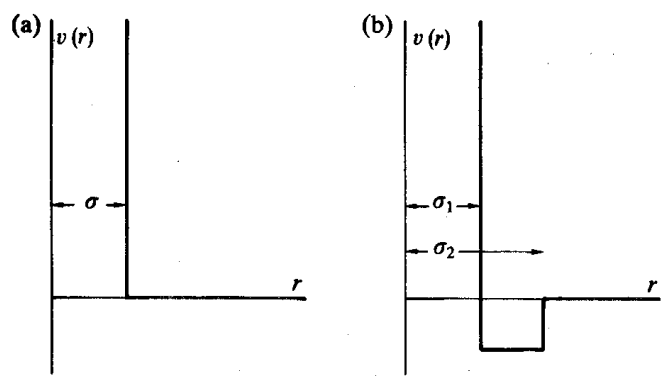

Figure 2.1: (a) Hard sphere and (b) square-well potentials.[70]

These simple models are very convenient to program and computationally efficient to execute. They take the mathematical form

$$u_{hs} = \begin{cases} \infty \ (r < \sigma) \\ 0 \ (r \geq \sigma) \end{cases}; \ u_{sw} = \begin{cases} \infty \ (r < \sigma_1) \\ -\varepsilon \ (\sigma_1 \leq r < \sigma_2), \\ 0 \ (r \geq \sigma_2) \end{cases} \tag{2.5}$$

respectively. Here r is the distance between a pair of atoms, σ is the characteristic length at which the potential goes to zero, and ε is the potential well depth. Although highly idealized, they were a good first approximation and could be used to qualitatively describe simple systems. Soft-sphere potentials followed, which introduced a parameter v to further describe the repulsive interactions:

$$u_{ss} = \varepsilon\left(\frac{\sigma}{r}\right)^{v} \tag{2.6}$$

As v is increased the "hardness" (i.e. repulsive energy) also increases, more closely resembling the hard sphere potential. To further refine this model, one would need to add an attractive term to capture long-range interactions. One of the most popular and widely used two-body potentials, the Lennard-Jones (LJ) 12-6 potential, does just this, and takes the form:

$$u_{ij} = 4\varepsilon\left[\left(\frac{\sigma}{\mathbf{r}_{ij}}\right)^{12} - \left(\frac{\sigma}{\mathbf{r}_{ij}}\right)^{6}\right] \tag{2.7}$$

The r^{-12} term describes short-range repulsive forces due to Pauli repulsion, while the r^{-6} encompasses longer acting forces (e.g. van der Waals forces). This potential has been used for many different types of systems and tends to work best for noble gases and certain liquids, though it can also be used to describe interactions with solids. In order to estimate LJ interaction parameters between different types of atoms, mixing rules can be applied. A common approach is the Lorentz-Berthelot mixing rule:

$$\begin{aligned} \sigma_{ij} &= \frac{1}{2}\left(\sigma_i + \sigma_j\right) \\ \varepsilon_{ij} &= \sqrt{\varepsilon_i \varepsilon_j} \end{aligned} \tag{2.8}$$

In order to add Coulombic interaction contributions to the LJ potential an additional term is required:

$$u_{ij} = 4\varepsilon\left[\left(\frac{\sigma}{\mathbf{r}_{ij}}\right)^{12} - \left(\frac{\sigma}{\mathbf{r}_{ij}}\right)^{6}\right] + \frac{C q_i q_j}{\varepsilon_0 \mathbf{r}_{ij}} \tag{2.9}$$

This adds minimal complexity to the potential while expanding the types of atoms/molecules (e.g. NaCl, H_2O) that can be simulated. In Eq. (2.9) $q_{i,j}$ are the atomic point charges, ε_0 is the dielectric constant, and C is a constant ($1/4\pi$).

Other notable pairwise potentials in use are the Buckingham, Stockmayer, and Morse potentials. The Buckingham potential[71] is similar to the 12-6 LJ potential, however the r^{-12} term is replaced by an exponential term ($e^{-r/r0}$). The Stockmayer potential[72] also uses the LJ potential as a base but adds a term to account for embedded point dipoles. The Morse potential[73] is useful for modeling diatomic molecules and atom/surface interactions, and is exponential in nature.

2.2.2 Many-Body Potentials

When certain materials are not adequately described by pairwise interactions many-body potentials can be introduced to achieve greater fidelity, though at greater computational cost. Popular examples in heat transfer applications include the Embedded Atom Method (EAM), Tersoff, and Stillinger-Weber (SW) potentials. EAM[74] is derived from density functional theory and is often used to model metals. The potential is a function of pairwise interactions as well as an "embedding function" that takes the electron charge density of surrounding atoms into account.

The Tersoff potential[75] is a three-body potential that takes the form:

$$U = \sum_i U_i = \frac{1}{2}\sum_{i \neq j} V_{ij}$$
$$V_{ij} = f_c(\mathbf{r}_{ij})[A_{ij}e^{-\lambda_1 \mathbf{r}_{ij}} - B_{ij}e^{-\lambda_2 \mathbf{r}_{ij}}] \tag{2.10}$$

Here the total energy U is split into multiple site energies U_i that are related to the interaction energy V_{ij}. The first term in the V_{ij} equation represents the repulsive energy

(where A_{ij} is an atom-specific interaction energy parameter) while the second term represents bonding, where the bonding strength between two atoms (B_{ij}) decreases as the local density (and thus number of competing bonds) increases. In this way the Tersoff potential is able to take the local environment of any given atom into account. It is often used to model Si and Ge (which have a diamond lattice structure) and certain forms of C, and has been modified for use with many other atoms/molecules.

Another potential used to approximate Si is the SW[76] potential. Generally, the SW potential uses pairwise and triplet interactions:

$$\begin{aligned} U &= \sum_{i<j} \upsilon_2(\mathbf{r}_{ij}) + \sum_{i<j<k} \upsilon_3(\mathbf{r}_i, \mathbf{r}_j, \mathbf{r}_k) \\ \upsilon_2 &= \varepsilon A\left(\frac{B}{\mathbf{r}_{ij}^p} - \frac{1}{\mathbf{r}_{ij}^q}\right) e^{\frac{1}{\mathbf{r}_{ij} - a}}, \quad r < a \\ \upsilon_3 &= \varepsilon[h(\mathbf{r}_{ij}, \mathbf{r}_{ik}, \theta_{jik}) + h(\mathbf{r}_{ji}, \mathbf{r}_{jk}, \theta_{ijk}) + h(\mathbf{r}_{ki}, \mathbf{r}_{kj}, \theta_{ikj})] \end{aligned} \tag{2.11}$$

The pairwise υ_2 term has a similar form to the LJ potential, while the h term in υ_3 uses a combination of exponential and cosine terms to describe the bond bending between triplets (via atom separation r and triplet angle θ). By varying the parameters of υ_2 and υ_3 the SW potential has been fit to many other atoms and molecules.

Another potential of note is the Adaptive Intermolecular Reactive Bond Order (AIREBO) potential,[77] which built upon the REBO[78] potential to calculate the potential energy of covalent bonds and, importantly, intermolecular forces in carbon and hydrocarbon systems.

$$U = \frac{1}{2}\sum_i \sum_{j \neq i} \left[U_{ij}^{REBO} + U_{ij}^{LJ} + \sum_{k \neq i,j} \sum_{l \neq i,j,k} U_{kijl}^{torsion} \right] \tag{2.12}$$

In Eq. (2.12) U^{REBO} is the short-range bond order term that allows for the formation and breaking of covalent bonds, U^{LJ} handles pairwise interactions, and $U^{torsion}$ is a four-body potential that describes dihedral angle preferences of the system.

As can now be seen, there are various methods of modeling interactions between atoms. Some are derived from classical or quantum theoretical frameworks (e.g. DFT), while others are fitted to empirical results and/or optimized to recreate certain properties (e.g. bonding, phonon, etc.). There are many considerations, such as the tradeoff between accuracy and computational efficiency, which should be taken into account when choosing a potential to describe a given system.

2.2.3 Potential Modifications

Other important aspects regarding interaction potentials are the cutoff distance used, and any discontinuities that may occur at said cutoff point. A cutoff (r_c) must be used in order to reduce computation time, by excluding any atoms outside the cutoff range. This reduces the number of force calculations that need to be carried out each timestep, effectively truncating the potential.

$$U(\mathbf{r}_{ij}) = \begin{cases} U(\mathbf{r}_{ij}) & r < r_c \\ 0 & r \geq r_c \end{cases} \tag{2.13}$$

This, however, can result in problems because there is a sudden jump in energy at r_c that produces errors in the energy term. For certain potentials that decay quickly toward a zero value (e.g. LJ 12-6), selection of a large enough cutoff radius can minimize these errors. Parameters of interest are also an important consideration when choosing r_c. Using the LJ potential as an example, quantities like density and vapor pressure show less sensitivity to r_c, whereas surface tension is more dependent on the tail of the potential and

thus requires a larger cutoff.[79] For the LJ potential r_c should generally be above a minimum of 2.5σ, at which the potential is 1.6% of the well-depth[70]

Other methods of dealing with the potential discontinuity at r_c involve either shifting the potential, or using a switching function. Shifting does not affect the forces at r≠r_c, though it does alter the total energy. The simplest method of shifting the potential takes the form:

$$U(\mathbf{r}_{ij}) = \begin{cases} U(\mathbf{r}_{ij}) - U(r_c) & r < r_c \\ 0 & r \geq r_c \end{cases} \tag{2.14}$$

This simple shift, visualized in Figure 2.2, is convenient to implement, however there is still a discontinuity in the force F at r=r_c which will cause errors, especially when using large timesteps.

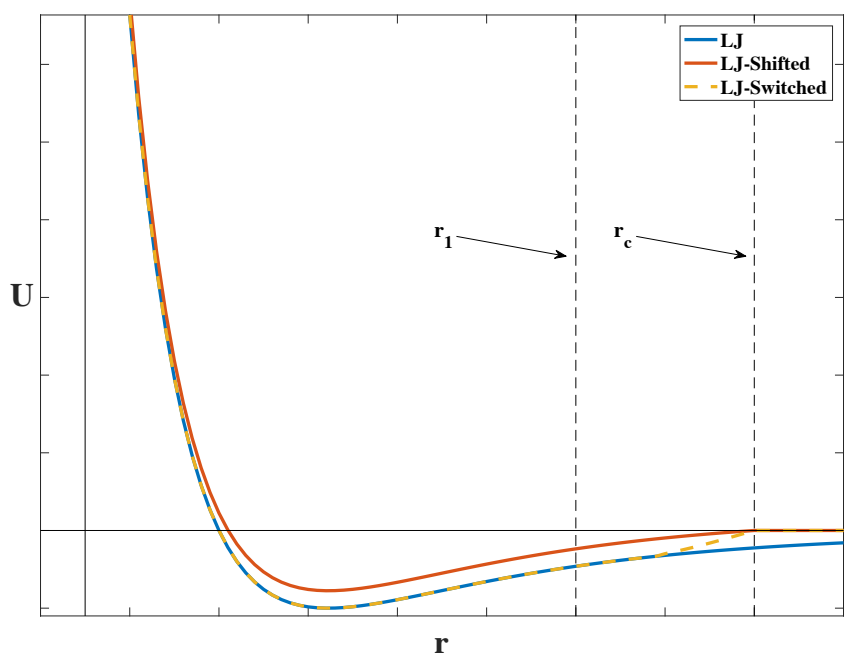

Figure 2.2: Comparison of full LJ potential with shifted and switched LJ potentials.

Thus various other shifts, including polynomial- and exponential-based functions, have been introduced to deal with the issues previously mentioned. One relatively popular shift takes the following form:

$$U(\mathbf{r}_{ij}) = \begin{cases} U(\mathbf{r}_{ij}) - U(r_c) - U'(r_c)(\mathbf{r}_{ij} - r_c) & r < r_c \\ 0 & r \geq r_c \end{cases} \tag{2.15}$$

This is known as a force-shifted potential[80] due to the $U'(r_c)$ term, which ensures a zero force at r=r_c and makes the force continuous. However it makes the potential well-depth more shallow (similar to the shifted potential shown in Figure 2.2), and requires more computational resources.

Finally, a switching function $S(r_{ij})$ can be multiplied with the potential to smoothly bring the potential to zero in an interval near r_c.

$$U(\mathbf{r}_{ij}) = \begin{cases} U(\mathbf{r}_{ij}) & r < r_1 \\ S(\mathbf{r}_{ij})U(\mathbf{r}_{ij}) & r_1 \leq r < r_c \\ 0 & r \geq r_c \end{cases} \tag{2.16}$$

The switching function should smoothly go from 1 to 0 on the interval $[r_1, r_c]$, and have continuous first and second derivatives:

$$\begin{array}{ll} S(r_1) = 1 & S(r_c) = 0 \\ S'(r_1) = 0 & S'(r_c) = 0 \\ S''(r_1) = 0 & S''(r_c) = 0 \end{array} \tag{2.17}$$

For this reason S is usually a polynomial function, though this is not necessary. A switched LJ potential is also shown in Figure 2.2. The switched function has the advantage of maintaining the potential well depth, being continuous and differentiable, and only deviating from the full potential within the short interval $[r_1, r_c]$. The forces, however, will be altered within the interval, contributing more overall error.

Another method used to minimize errors due to potential truncation is to add a tail (long-range) correction. This refers to corrections applied to system parameters (energy, pressure, density, etc.) in order to compensate for the truncated portion of the potential. Corrections usually take the general form:

$$W_{TC} = cN\rho \int_{r_c}^{\infty} g(r)W(r)r^2 dr \tag{2.18}$$

where W_{TC} is the tail correction portion of the desired parameter, c is a constant, N is the number of atoms, $g(r)$ is the radial distribution function, and $W(r)$ is the full form of the parameter of interest (e.g. full LJ potential).[70] In many systems it is sufficient to assume an isotropic distribution past r_c so that $g(r>r_c)\approx 1$, simplifying the calculation. For the 12-6 LJ potential, the potential energy tail correction is:

$$U_{TC} = \frac{8}{3}\pi\rho\varepsilon\sigma^3\left[\frac{1}{3}\left(\frac{\sigma}{r_c}\right)^9 - \left(\frac{\sigma}{r_c}\right)^3\right] \tag{2.19}$$

These corrections can be discretized and applied at each timestep in order to more accurately obtain system properties. Many corrections have been developed for specific purposes, such as the proper calculation of surface tension, diffusion coefficients, dielectric constants, etc. For inhomogeneous systems, where the density distribution is non-uniform (i.e. $g(r>r_c)\neq 1$), special care must be taken when applying long-range corrections, as additional equations and/or methods may be required. For example, inhomogeneous systems with planar interfaces can be treated by dividing the domain into thin slabs (provided each slab is homogeneous), and summing the contribution from each to determine the full tail correction.[81]

2.2.4 Additional Potentials

In addition to the interaction potential, more complex molecules may require additional potentials to describe certain intra-molecular interactions. These are most commonly the bond, angle, and torsion potential interactions. Sufficiently meeting these molecular constraints during time integration will be further detailed in Section 2.3.2.

The bonded potential describes a molecule's covalent bonds. The most common bond model is the harmonic bond potential:

$$U_b(\mathbf{r}_{ij}) = K_{ij}(\mathbf{r}_{ij} - r_0)^2 \tag{2.20}$$

where U_b is the bond energy, K_{ij} is the force (or spring) constant, and r_o is the equilibrium bond length. From this relation the force on an atom i from a bonded atom j (F_{ij}) can be determined. Only the value for one atom of the pair has to be stored, since from Newton's Third Law we know the other atom will have a force (in this case F_{ji}) equal in magnitude and opposite in direction. In general, the harmonic potential is used when deviations from r_0 are expected to be small, with no possibility of bond breaking.

A more realistic bond stretching potential that can handle large deviations from r_0 is the Morse bond potential:[82]

$$U_b(\mathbf{r}_{ij}) = \varepsilon[1 - e^{-\alpha(\mathbf{r}_{ij} - r_0)}]^2 \tag{2.21}$$

where ε is the potential well depth, and α is a stiffness parameter. This potential better approximates the anharmonicity of molecular vibrations and explicitly takes bond dissociation into account.

There are other anharmonic bond potential models,[83] as well as potentials modeled for specific molecules. One such potential is the finite extensible nonlinear

elastic (FENE) potential,[84] which uses a bead-spring model to approximate coarse-grained, flexible polymer molecules.

For a set of two bonds that share a common (center) atom, an angular potential is required to define interactions between the triplet of atoms. For atoms *i, j,* and *k* (where *j* is the center atom), θ_{ijk} defines the angle between them. Taking the bond vectors as $r_{ij}=r_i-r_j$ and $r_{kj}=r_k-r_j$, it follows that:

$$\cos(\theta_{ijk}) = \frac{\mathbf{r}_{ij} \cdot \mathbf{r}_{kj}}{r_{ij} r_{kj}} \tag{2.22}$$

The force can then be calculated in the usual way:

$$F_{i,a} = -\nabla_i U_a = -\frac{\partial U_a}{\partial \theta_{ijk}} \frac{\partial \theta_{ijk}}{\partial \mathbf{r}_i} \tag{2.23}$$

where $F_{i,a}$ is the force on atom *i* due to angular constraints, and U_a is the angular potential. As with the bond potential, the harmonic angle potential is one of the most often used in simulations due to its simplicity and ease of implementation:

$$U_a(\theta_{ijk}) = k^h_{ijk}(\theta_{ijk} - \theta_0)^2 \tag{2.24}$$

In Eq. 2.23 k_{ijk} is a force constant that represents the strength of the angle, and θ_0 is the equilibrium angle. The harmonic potential works well for more rigid molecules that have angle deformations within a close range of the equilibrium angle. For simulations of biological molecules a popular potential (used in the CHARMM program) includes an additional term:

$$U_a(\theta_{ijk}, \mathbf{r}_{ik}) = k^h_{ijk}(\theta_{ijk} - \theta_0)^2 + k^{UB}_{ik}(\mathbf{r}_{ik} - r^{UB}_0)^2 \tag{2.25}$$

Where k^{UB}_{ik} is the Urey-Bradley force constant, $r_{ik}=r_i-r_k$, and r^{UB}_0 is the equilibrium distance between atoms *i* and *k*.[85] This effectively introduces a bond between the atoms. Other popular angle potentials are the cosine angle and cosine harmonic potentials:

$$U_a(\theta_{ijk}) = k^c_{ijk}[1+\cos(\theta_{ijk})]$$
$$U_a(\theta_{ijk}) = k^{ch}_{ijk}[\cos(\theta_{ijk})+\cos(\theta_{ijk})]^2 \tag{2.26}$$

which have the advantage of being more computationally efficient, since computation of inverse cosine functions are not required to solve for the forces.

Finally, torsional potentials describe the rotation/bending of quartets of atoms, and can be separated into either dihedral or improper interactions. Dihedral interactions describe the torsion of four consecutively linked atoms and are used to constrain rotation around a bond. The configuration of atoms *i, j, k,* and *l* are described by the angle (Φ_{ijkl}) between two planes passing through the molecule. The first plane passes through *i, j,* and *k* while the second plane passes through *j, k,* and *l* (Figure 2.3), and the angle can be calculated from the bond vectors.

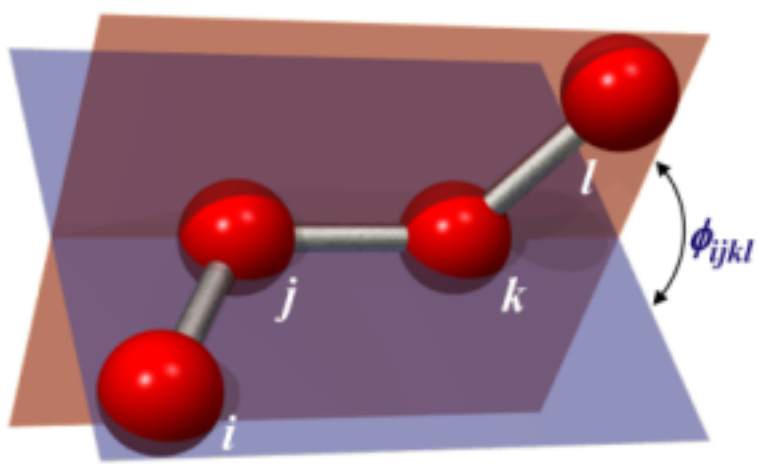

Figure 2.3: The planes and angle used to describe dihedral interactions (from http://cbio.bmt.tue.nl/pumma/index.php/Theory/Potentials).

The harmonic and phase-shifted harmonic dihedrals potential takes the form:

$$U_d(\phi_{ijkl}) = k_{ijkl}^{h,d}[1 + d\cos(n\phi_{ijkl})]$$
$$U_d(\phi_{ijkl}) = k_{ijkl}^{ps}[1 + d\cos(n\phi_{ijkl} - \phi_0)] \tag{2.27}$$

where d is either -1 or +1 depending on the interaction potential used, and n is an integer ≥0 that represents the number of minima in one 360° rotation. Φ_0 is a reference angle, usually used to shift the potential so that its minimum occurs at 180°.

As opposed to dihedral interactions, improper dihedral interactions describe those of quartets of atoms where three atoms (*j, k, l*) are all bonded to a common atom (*i*). This potential is used to maintain the planarity of a molecule, and the often-used harmonic improper potential is:

$$U_{imp} = k_{ijkl}^{imp}(\phi_{ijkl} - \phi_0^{imp})^2 \tag{2.28}$$

2.3 Time Integration

2.3.1 Solving Newton's Equations

After all potential considerations are complete and the forces between all particles can be computed, a time integration scheme is required to solve Newton's equations of motion to generate the evolution of any given system. There are several characteristics that an integration scheme should aim to achieve: time-reversibility, energy conservation, computational efficiency, ability to use longer timesteps, and requiring only one set of force calculations per timestep. Over the decades many integrators have been proposed and used, the most common being the Gear Predictor-Corrector, Verlet, and Velocity-Verlet algorithms.

The Gear Predictor-Corrector method solves the equations in two phases: First, a Taylor series expansion is used to predict the changes in position, velocity, and acceleration from time t to time $t+dt$. Next, the forces and accelerations are calculated from the predicted positions and used to calculate a corrective acceleration term, which is in turn used to calculate corrected positions:

$$\begin{aligned}
\Delta\mathbf{a}(t+\delta t) &= \mathbf{a}^{c}(t+\delta t) - \mathbf{a}^{p}(t+\delta t) \\
\mathbf{r}^{c}(t+\delta t) &= \mathbf{r}^{p}(t+\delta t) + c_0\Delta\mathbf{a}(t+\delta t) \\
\mathbf{v}^{c}(t+\delta t) &= \mathbf{v}^{p}(t+\delta t) + c_1\Delta\mathbf{a}(t+\delta t) \\
\mathbf{a}^{c}(t+\delta t) &= \mathbf{a}^{p}(t+\delta t) + c_2\Delta\mathbf{a}(t+\delta t) \\
\mathbf{b}^{c}(t+\delta t) &= \mathbf{b}^{p}(t+\delta t) + c_3\Delta\mathbf{a}(t+\delta t)
\end{aligned} \tag{2.29}$$

where a is the acceleration, r is the position, v is the velocity, b is the 3rd order derivative of the position, t is the time, δt is the timestep, and the c and p superscripts denote corrected and predicted, respectively. Gear[86] calculated coefficients c_0 through c_3 for optimum stability and accuracy. Though there is little energy fluctuation, the algorithm is not time reversible and does not conserve energy.

The Verlet algorithm[87] uses Taylor expansions of $r(t+\delta t)$ and $r(t-\delta t)$, which are added together and simplified to produce:

$$\mathbf{r}(t+\delta t) = 2\mathbf{r}(t) - \mathbf{r}(t-\delta t) + \delta t^2\mathbf{a}(t) + O(\delta t^4) \tag{2.30}$$

The velocity is completely removed from the equation by addition of the Taylor expansions, and thus is computed from a first-order central difference equation with an error of $O(\delta t^2)$. Although the algorithm is simple and stable, the velocity errors can be problematic, and knowledge of two prior timesteps is required to calculate a new position. The velocity-Verlet algorithm,[88] which is the algorithm used in all

investigations presented in this work, attempts to correct this by incorporating velocity explicitly via the expansions:

$$\begin{aligned} \mathbf{r}(t+\delta t) &= \mathbf{r}(t) + \mathbf{v}(t)\delta t + \frac{1}{2}\mathbf{a}(t)\delta t^2 + \ldots \\ \mathbf{v}(t+\delta t) &= \mathbf{v}(t) + \frac{1}{2}\delta t[\mathbf{a}(t) + \mathbf{a}(t+\delta t) + \ldots \end{aligned} \tag{2.31}$$

The algorithm is then carried out as follows:

$$\begin{aligned} &1.\ \textit{Calculate}\ \mathbf{v}(t+\frac{1}{2}\delta t) = \mathbf{v}(t) + \frac{1}{2}\mathbf{a}(t)\delta t \\ &2.\ \textit{Calculate}\ \mathbf{r}(t+\delta t) = \mathbf{r}(t) + \mathbf{v}(t+\frac{1}{2}\delta t)\delta t \\ &3.\ \textit{Calculate}\ \mathbf{a}(t+\delta t)\ \textit{from Potential and}\ \mathbf{x}(t+\delta t) \\ &4.\ \textit{Calculate}\ \mathbf{v}(t+\delta t) = \mathbf{v}(t+\frac{1}{2}\delta t) + \frac{1}{2}\mathbf{a}(t+\delta t)\delta t \end{aligned} \tag{2.32}$$

This algorithm is stable, conserves energy, and its error is of the same order as the original Verlet scheme. Also, since the velocity at each timestep is known quantities such as kinetic energy and temperature can easily be calculated.

More recently multi-timescale integrators such as the reversible reference system propagator algorithm (rRESPA)[89] have been introduced, which allows for flexibility in timescale choice. The system can effectively be divided, so that components that move more slowly can use a longer timestep, while faster varying components use a shorter step. This improves efficiency, which allows investigation of larger systems and longer simulation times.

2.3.2 Constraints

Once a suitable potential and integrator is chosen, attention can be turned to the related consideration of constraining parts of the system, if applicable. This requires the use of

additional iterative calculations, adding computational complexity, but allows for the use of larger timesteps, and is necessary for maintaining a physically sound system. For example, any molecule or rigid body that consists of multiple atoms requires some constraint algorithm to be solved during normal time integration that sufficiently maintains its molecular shape. Several algorithms have been developed in order to solve constraint equations, including the SHAKE, RATTLE, and LINCS algorithms.

The SHAKE algorithm[90] was first developed for use with the Verlet integrator, and is used to constrain (often large) molecules with internal degrees of freedom. In Cartesian coordinates the positions of the unconstrained system are first determined, then successively modified to meet bond and/or angle constraint requirements. The unconstrained positions are used to first compute Lagrange multipliers (λ_k) for each constraint. Positions are then updated through addition of a "restorative" force (proportional to λ_k). These steps are iterated until the change in each λ_k value is less than some predetermined tolerance (usually only a few iterations). The iteration is necessary to deal with atoms that have multiple bond or angle constraints, and thus coupled λ_k values.

The RATTLE algorithm[91] extends the SHAKE algorithm for use with the velocity-Verlet integrator. Since the algorithm computes velocities directly, a second set of restorative forces is required to eliminate atom velocity components along the bond itself. The constraints are modeled as follows:

$$\begin{aligned} \mathbf{r}_{ij}(t+\delta t)\cdot\mathbf{r}_{ij}(t+\delta t) &= d_{ij}^2 \\ \mathbf{v}_{ij}(t+\delta t)\cdot\mathbf{r}_{ij}(t+\delta t) &= 0 \end{aligned} \tag{2.33}$$

where d_{ij} is the bond length. The SHAKE algorithm satisfies the first (position) constraint, while RATTLE satisfies the second (velocity) constraint. RATTLE is of

course a bit more computationally expensive than SHAKE due to the additional constraint. Another algorithm, SETTLE, is a specialized analytical, non-iterative solution of SHAKE/RATTLE. Though limited to three-body molecules, its exact nature makes it faster than SHAKE.

The LINCS algorithm[92] is also non-iterative and faster than SHAKE. As with the previous algorithms, it begins with solving the unconstrained system. The constraint equations and their first and second derivatives are set to zero in order to determine the constrained equations of motion. After adding some corrective terms to deal with rotation and accumulation errors the new constrained positions can be solved via matrix algebra. In order to save computational time a matrix inverse is approximated using a series expansion:

$$(I - A_n)^{-1} = I + A_n + A_n^2 + A_n^3 + \ldots \tag{2.34}$$

where I is the identity matrix, and A is a sparse, symmetric matrix (with zeros on the diagonal) that contains the mass and constraint information. Because this approximation is only valid for eigenvalues of A less than 1, the LINCS method is only suitable for systems with so-called low connectivity. A system with only bond constraints has low connectivity and is thus valid, however large molecules with both bond and angle constraints (e.g. pentane) could be problematic. In this case an alternative method of matrix inversion would need to be applied.

2.4 Thermostats

Thermal control is often required in molecular dynamics, thus several different thermostatting methods have been designed to regulate the temperature of atoms in a

simulation. The simplest thermostat method is direct velocity rescaling. From statistical mechanics, for a system of particles we have:

$$\begin{aligned} \langle KE \rangle &= \frac{1}{2} M \left\langle \sum_i^N \mathbf{v}_i^2 \right\rangle = \frac{3}{2} N k_B T \\ \Rightarrow T &= \frac{M}{3Nk_B} \left\langle \sum_i^N \mathbf{v}_i^2 \right\rangle \end{aligned} \tag{2.35}$$

Here the left-hand side of the first equation is the ensemble average of the kinetic energy, M is the total mass of the system, v_i is the particle velocity, N is the number of particles, k_B is the Boltzmann constant, and T is the temperature. Relating the current temperature T to the new (desired) temperature T_0 we then have:

$$v_i^{new} = v_i \sqrt{\frac{T^0}{T}} \tag{2.36}$$

where T^{t+1} is the goal temperature of the thermostat. In this way the velocity can explicitly be scaled every certain number of timesteps in such a way that the average temperature of the particles in question (usually with a uniform or Gaussian distribution) reaches the desired T. Velocity rescaling is a direct temperature control used in conjunction with the microcanonical (NVE) ensemble, and it should be noted that as velocity-scaling thermostats are somewhat unphysical it is usually relegated for use only for initialization and equilibration purposes.

The Berendsen thermostat[93] is another velocity scaling technique for use with the NVE ensemble that simulates weak coupling to a virtual external heat bath. Its formulation corresponds to the thermostatted particles repeatedly colliding with virtual particles in a heat bath at T_0:

$$v_i^{new} = v_i \sqrt{1 + \frac{dt}{\tau_T}\left(\frac{T^0}{T} - 1\right)} \tag{2.37}$$

In Eq. 2.36 *dt* is the timestep and τ_T is called the rise time. The rise time is a tunable parameter, and determines the strength of coupling to the heat bath (larger τ_T means weaker coupling).

The Langevin thermostat[94] controls the temperature of a group of atoms by simulating interactions with an implicit solvent. Every timestep each thermostatted particle has two forces added to it (in addition to the force calculated from the interatomic potential):

$$m_i \mathbf{a}_i = -\nabla U - m_i \Gamma \mathbf{v}_i + \eta_i(t) \tag{2.38}$$

In this equation Γ is a friction (with units s^{-1}), so that the second term on the right-hand side represents the force due to frictional drag or viscous damping as the system moves through the implicit solvent (thus the negative sign). $\eta_i(t)$ is a random force due to solvent atoms bumping into particle *i*. The force has a Gaussian distribution, and is proportional to the following:

$$\eta_i(t) \propto \sqrt{\frac{m k_B T}{\Gamma dt}} \tag{2.39}$$

The resulting trajectories sample the canonical (NVT) ensemble. The stability of Langevin dynamics allows the use of a larger timestep, which is helpful when simulating more complex systems.

Finally, the Nosé-Hoover thermostat[95] explicitly adds a degree of freedom to produce alternate Hamiltonian equations of motion. The additional (and dimensionless) degree of freedom acts as an explicit heat bath to control particle velocities. The Nosé-Hoover version of the Hamiltonian is as follows:

$$H_{N-H} = \sum_{i=1}^{N} \frac{\mathbf{p}_i^2}{2m_i s_t^2} + U(\mathbf{r}) + g_d k_B T \ln(s_t) + \frac{p_s^2}{2Q} \tag{2.40}$$

Here p_i is the momentum, s is a time-scaling variable for the additional degree of freedom, p_s is its conjugate momentum, Q is a mass-like parameter that determines the strength of the thermostat, and g_d is the number of degrees of freedom of the system. The resulting equations of motion are deterministic, time-reversible, and still sample the NVT ensemble. To improve ergodicity the thermostat can also be implemented as a chain, where one thermostatting variable is thermostatted by another, and so on, thus multiple heat baths are linked together. All of these advantages explain the thermostat's frequent use in MD. It should also be mentioned that the Nosé-Hoover framework can also be used to reliably produce isobaric-isothermal (NPT) and isobaric-isenthalpic (NPH) ensembles.

2.5 Boundary Conditions

There are several options for boundary conditions when running MD simulations, and care must be taken to select boundaries applicable to the system being investigated.

A commonly used fixed boundary is the specularly reflective, adiabatic wall. Any particle that would cross the boundary during a timestep is instead placed back inside the simulation domain and has the sign of its relevant velocity component reversed. For example, considering this type of boundary at the top of a simulation domain, if some particle i's trajectory would have it pass the wall by 2Å in the z-direction it would simply be placed back inside the domain at a z distance 2Å from the wall, and have the sign of $v_{z,i}$ reversed. With this boundary there is no force or momentum transfer, and effectively has a slip condition. For a non-slip condition both the normal and tangential components

of velocity can be reversed or sampled from a Gaussian distribution and assigned randomly.

Other fixed boundaries can exert forces on nearby particles, based on an interaction potential of choice. The simplest case is flat and purely repulsive, e.g. the repulsive portion of the LJ 12-6 potential:

$$U_{wall}(z) = 4\varepsilon\left(\frac{\sigma}{z}\right)^{2n} \qquad z < 2^{1/n}\sigma \tag{2.41}$$

where in this case z is the perpendicular distance from the wall. The $2^{1/n}\,\sigma$ cutoff distance (which is the minimum point of the standard LJ potential) ensures a purely repulsive interaction. With more complex formulations other wall potentials can simulate wall texture, such as the LJ 10-4-3 potential:

$$U_{wall}(\mathbf{r}) = 2\pi\varepsilon\left[\frac{2}{5}\left(\frac{\sigma}{r}\right)^{10} - \left(\frac{\sigma}{r}\right)^{4} - \frac{\sqrt{2}\sigma^{3}}{3\left[r + \left(0.61/\sqrt{2}\right)\sigma\right]^{3}}\right] \tag{2.42}$$

Many other potentials (harmonic, LJ 9-3, etc.) can be used for this type of boundary condition.

Although common, boundary walls do not necessarily have to be fixed. In certain cases (e.g. membrane permeability studies) it may be advantageous to have one or more walls move with a constant or piston-like motion to exert pressure and drive the dynamics of the system. In an NVT ensemble this type of boundary could be helpful in maintaining a target pressure. Similarly, if there are atoms continuously being added to a system or a strain is imposed that changes the length of a system, boundary walls may need the ability to move outward in order to encompass all particles.

One of the most important and often used boundary conditions in MD is the periodic boundary condition. When a particle moves some distance through a periodic boundary, it reappears on the other side of the domain the same distance from the opposite boundary (with unchanged velocity). I.e.,

$$\begin{aligned} &if\ x_i^{old} = x_{\max} + \delta x, \\ &\Rightarrow x_i^{new} = x_{\min} + \delta x \end{aligned} \tag{2.43}$$

where the boundaries are located at x_{min} and x_{max}. Importantly, particles near periodic boundaries also interact with the images of particles near the opposite boundary. This means that smaller domains (with smaller numbers of particles) can be used in simulations to represent more macroscopic systems, as the periodic images (Figure 2.4) help to reduce finite-size effects.

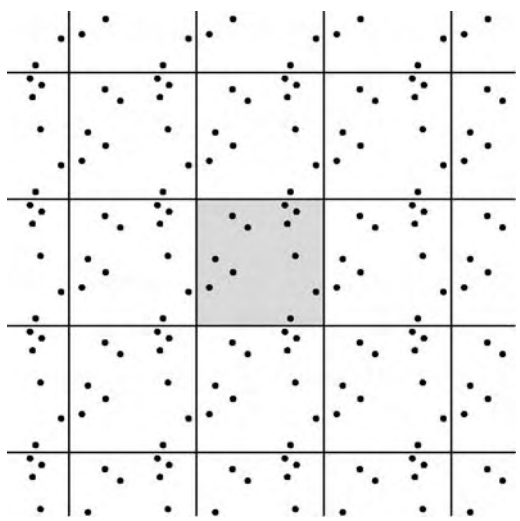

Figure 2.4: Two-dimensional example of a simulation domain (shaded gray) and its periodic images.[95]

When using periodic boundaries one must take care to prevent a particle from interacting with its own image. Minimum image conventions should also be followed: i.e., when an atom *i* interacts with the image of an atom *j*, only the image with the shortest distance from *i* should be used. We can ensure this by using a simulation box size of at least $2*r_c$,

thus each particle interacts with only one image of every other particle, at most. Periodic boundaries are a computationally efficient way to model macroscopic behavior, though system characteristics with wavelengths/mean free paths larger than the simulation box will not be captured adequately.

Chapter 3

Phobic/Philic Nano-Patterning Effects on Pool Boiling Heat Transfer

3.1 Introduction

Heat transfer on the micro- and nano-scales has quickly become an important area of research and development due to its implications for use in MEMS/NEMS devices and electronics cooling[96-99] in the past decade. Boiling heat transfer on micro/nanocale substrates has the capacity for rapid large heat flux removal, and as such has previously been implemented in small-scale devices,[100] although the mechanisms driving this type of nanoscale heat transfer are not well understood.

Advances in micro- and nanoscale manufacturing have made it possible to further enhance heat transfer at small scales via use of structured surfaces. Micro and nanostructured surfaces offer a good means of passively improving boiling heat transfer due to increased boiling surface area and nucleation sites formed by nano/microscale surface roughness.[7,31,38] Another interest that has recently been studied experimentally is the effect of hydrophobic and hydrophilic patterned surfaces on heat transfer. This patterning can affect bubble nucleation and increase CHF values.[6] With enhancement, pool boiling heat flux in these studies has reached values capable of removing ~1 MW/m^2 required for certain electronics cooling applications.

The parameters involved in employing such passive techniques could be hard to control experimentally, thus Molecular Dynamics (MD) simulations have been utilized to investigate the effect of phobic/philic patterning of a nano-structured substrate during both nucleate and explosive boiling. MD simulation is a powerful tool that can be used to investigate nanoscale phenomena with more flexible control than experimental

setups.[101] In this investigation, the substrate topology (roughness), temperature, and initial pressure were all controlled in order to more clearly view the effect of only the phobic/philic patterning. Previously many MD studies have been conducted on both homogeneous and heterogeneous systems in order to investigate heat transfer, phase change, flow properties, etc. Argon in liquid-vapor equilibrium has previously been studied[102] to aid in the prediction of density and surface tension. Interactions between liquid argon and channel walls in nanoscale flows have also been investigated[103,104] in order to determine flow properties with varying shear rates and surface roughness. Additionally, several studies have used flat substrates to investigate evaporation, effect of wettability, etc.[68,105,106] and there have recently been some studies focused on boiling/evaporation on nano-structured substrates using differently shaped nano-structures,[66,67,107] though to our knowledge no MD study has been conducted using a phobic/philic patterned surface.

In this study, four different scenarios were considered: 1) a flat argon-philic copper wall without nano-pillars, 2) an argon-philic copper wall with argon-philic pillar arrangement, 3) an argon-philic copper wall with argon-phobic pillar arrangement, and 4) an argon-phobic copper wall with an argon-philic pillar arrangement. A completely argon-phobic wall and pillar arrangement was not considered, as many previous experiments with this setup have shown reduced heat flux. Simulation of these four arrangements has allowed us to compare the heat flux and evaporation characteristics of a "standard" surface (homogeneous interaction potential) to surfaces with altered interaction potentials, and investigate mechanisms by which the heat transfer enhancements take place.

3.2 Simulation Method

The system used in the present simulations was comprised of a horizontal solid copper wall with or without four vertically oriented nano-pillars, a layer of liquid argon, and argon vapor molecules in a simulation box measuring 72.3 x 72.3 x 400 Angstroms (Å). Figures 3.1(a), (b) and (c) detail the overall configuration of the simulation box and the enlarged views of the copper wall and nano-pillars, respectively. The wall at the bottom of the simulation box consisted of a base of five monolayers of solid copper totaling 4,000 atoms. As in previous works, this was deemed enough to accurately act as a conduction layer for liquid heating.[52,108] For the cases that employed nano-pillars, four were arranged on the base wall in a symmetrical fashion. The nano-pillars were nine monolayers high and each measured 14.46 x 14.46 x 14.46 Å. The base wall and nano-pillars totaled 5,296 atoms, and were arranged in an FCC lattice structure corresponding to the (100) plane. For these copper atoms a lattice constant of 3.615 Å was used, corresponding to a density of 8.9 g/cm^3. Eleven monolayers of argon molecules were placed just above the copper base wall, covering both the wall and pillars. For the argon liquid atoms a lattice constant of 5.256 Å was used, corresponding to an initial density of 1.4 g/cm^3. Finally, 160 argon atoms (corresponding to a density of 5.77x10^{-3} g/cm^3) were placed above the liquid, filling the rest of the simulation box.

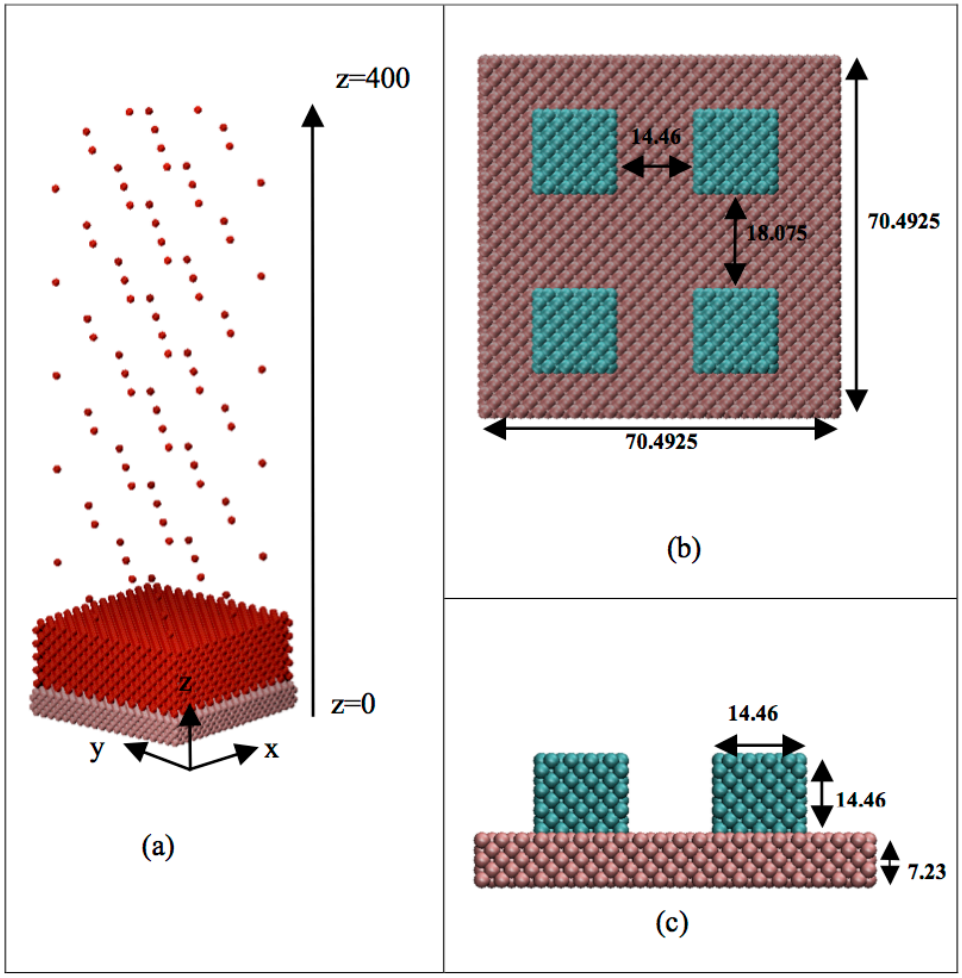

Figure 3.1: Sketch of the simulation model: (a) overall simulation configuration (b) and (c) enlarged views of the copper substrate and nano-pillars (Units: Å).

Interactions between all atoms were modeled with the standard 12-6 Lennard-Jones potential given by Equation 2.7. To reduce the computational cost an r_c equal to $6\sigma_{Ar\text{-}Ar}$ was employed. In order to study the effect of surface patterning, different Cu-Ar potential well depths and characteristic lengths were used in order to simulate 'argon-phobic,' and 'argon-philic' conditions. The phobic and philic cases are meant to simulate copper substrates with altered wetting characteristics (via surface modification, coatings, etc.), while the flat (pillar-less) case is used as a benchmark of normal Cu-Ar interaction.

Table 3.1 details the potential parameters for each type of interaction. The σ and ε Cu-Ar interaction values for the philic condition were calculated via normal Lorentz-Berthelot mixing rules of Equation 2.8. These values, based on previous work, are considered to produce a philic interaction between copper and argon (i.e. $\varepsilon_{\text{Cu-Ar philic}}$ = 0.0653 eV). To simulate argon-phobic Cu atoms, the $\varepsilon_{Cu\text{-}Ar\ philic}$ value was artificially halved in order to weaken the Cu-Ar interaction.

Table 3.1: Lennard-Jones potential parameters.

Atom Interaction	**σ (Å)**	**ε (eV)**
Cu-Cu	2.33[a]	0.4096[a]
Ar-Ar	3.405[a]	0.010423[a]
Cu-Ar (philic)	2.8675	0.0653
Cu-Ar (phobic)	2.8675	0.0327

[a] from Reference 67.

For simplicity, the different interaction cases will be referred to as follows: Flat Philic Case – philic Cu base wall, no nano-pillars; Philic Wall/Phobic Post Case - philic base wall, phobic pillars; Phobic Wall/Philic Post Case - phobic base wall, philic pillars; All Philic Case – philic base wall and nano-pillars.

The heat flux into the argon liquid was calculated using the following equation:

$$q'' = \frac{1}{V}\left[\sum_{i=1}^{N}(e_i - \mathbf{S}_i)\mathbf{v}_i\right] \tag{3.1}$$

where V is the volume, e_i is the per-atom energy (potential + kinetic), and S_i is the per-atom stress tensor. The heat flux fluctuates a great deal during the course of the

simulations, thus for clarity running average values of the heat flux are presented in the Results and Discussion (Section 3.4).

For each case the simulation is carried out in two phases. Phase I consists of initialization and system equilibration at 90K, at liquid-vapor equilibrium conditions. All atoms are initialized as an ensemble of velocities (with Gaussian distribution) corresponding to 90K. The system equilibration itself is split into two stages. The first stage uses a Langevin thermostat to maintain the temperature of all atoms, which are in the microcanonical (NVE) ensemble, while during the second stage the thermostat is removed and the entire system continues in the NVE ensemble. The Langevin thermostat models an interaction between the relevant particles and an implicit heat bath.[109] Interaction with this heat bath adds two corresponding forces to each particle, a friction force and a random force, which are discussed in greater detail in Section 2.4. The direction and magnitude of this force are altered via a uniform random number.[110] Once the system temperature and energy are stable Phase II commences, again using a Langevin thermostat to raise the temperature of the system to either 105K (low temperature case, representing evaporation/nucleate boiling) or 300K (high temperature case, representing explosive boiling). The thermostat is applied only to the second monolayer of the copper base wall, while the first layer is fixed to prohibit movement through the bottom of the simulation domain. The rest of the atoms are allowed to interact as they normally would, corresponding to the NVE ensemble. Both phases last a total of 9 ns (4 ns for Phase I, 5 ns for Phase II) and use the velocity Verlet algorithm for integration, with a time step of 5 fs.

The simulation domain is periodic in the four sidewalls of both the *x* and *y* directions, which helps to prevent finite size effects of the small simulation domain. As an additional check some simulations with a larger domain size (and more than twice the number of atoms) were run, and no significant differences in pressure, temperature, or density profiles were found. The top of the simulation domain is a fixed, adiabatic boundary. This means that an atom which moves outside the boundary by any distance is placed back inside the boundary at that same distance, while having the sign of its *z* velocity reversed (*x* and *y* velocities remain unchanged). All simulations were run using LAMMPS software (version 30 Oct 2014), a classical molecular dynamics code based on Plimpton's work,[111] while system visualization was performed with VMD v1.9.1.[112]

3.3 Error Analysis

In order to gauge the impact of the cutoff radius, multiple runs of the All Philic case at high temperature were carried out using different cutoff radii. The results are shown in Figure 3.2, which shows the difference in total energy over time, and Figure 3.3, which details the difference in the average heat flux. The cutoff radii chosen were 2σ, 4σ, 6σ, and 8σ, respectively. Additionally, 2.5σ was included as it was often recommended as the minimum cutoff radius for MD simulations. From Figure 3.2 we can see that as σ increases the calculated energy values begin to converge toward the true value. There is a ~3.1% difference between the 2σ and 8σ energy values, a ~1.5% difference between the 2.5σ and 8σ values, a ~0.27% difference between the 4σ and 8σ values, and only a <0.05% difference between the 6σ and 8σ values. However, there exists greater disparity in the heat flux seen in Figure 3.3, where the 8σ heat flux value at the end of the

simulation is ~20.7% greater than the 2σ value, and ~8.7% greater than the 2.5σ value. There is a ~4.9% difference between the 4σ and 8σ values, and a ~2.4% difference between the 6σ and 8σ values. These differences were similar for the peak overall heat flux values barring the 2.5σ peak, which was ~20% lower than the 8σ peak value.

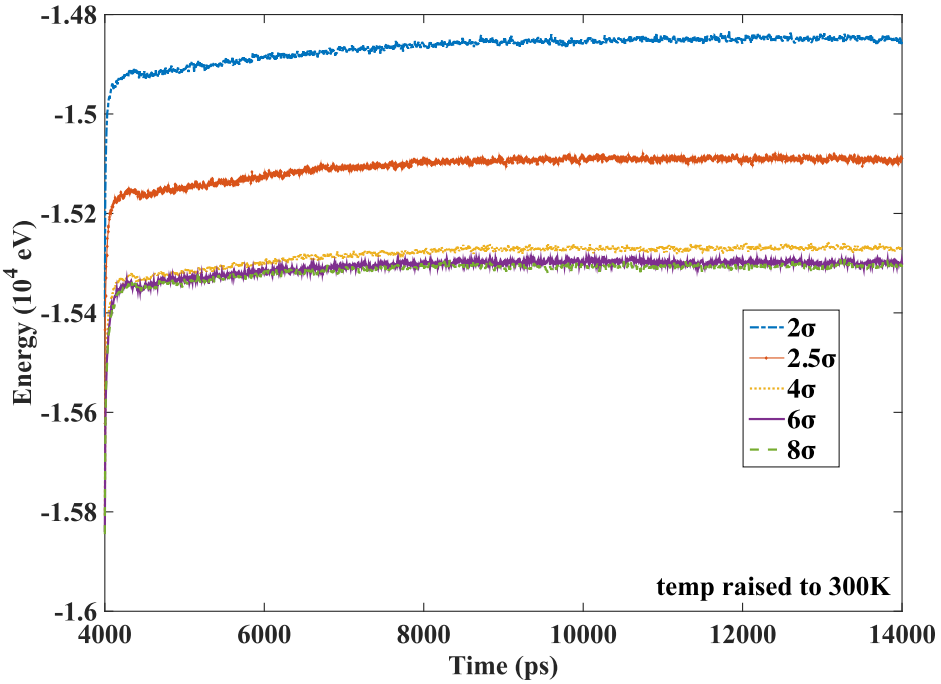

Figure 3.2: Total system energy based on cutoff radius (high temperature, All Philic cases).

Running on a workstation cluster of 80 2.6 GHz Intel Sandy Bridge 2670 CPUs each with 8 GB of RAM, the 2.5σ-cutoff simulation ran for a total of 4.6 hrs while the 4σ-cutoff simulation took a total of 11.4 hrs. The simulation using a 6σ cutoff ran for 30.3 hrs, while the 8σ-cutoff simulation ran for 62.3 hrs. All cutoff test simulations were performed using the high temperature, All Philic configuration, and used 6-7 MB of memory per processor. The 6σ cutoff was chosen in order to maintain high accuracy and save computation time thereafter.

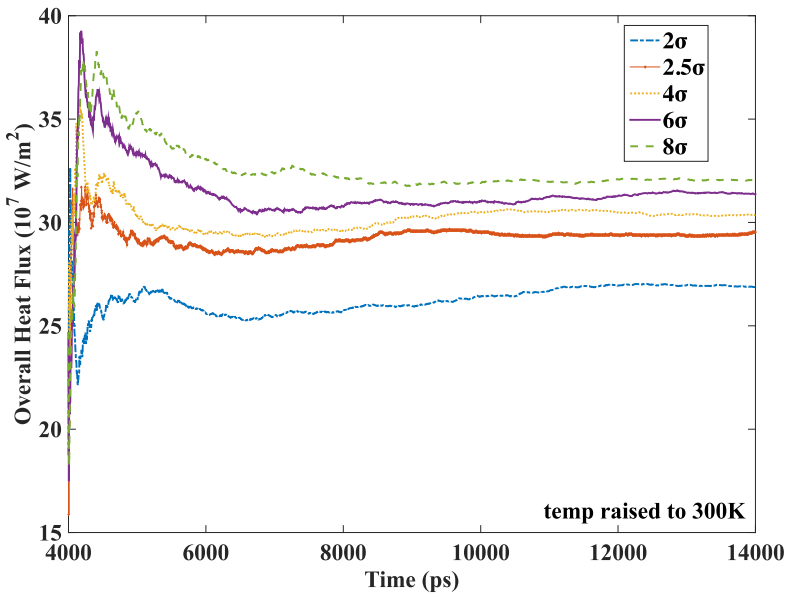

Figure 3.3: Overall heat flux based on cutoff radius (high temperature, All Philic cases).

3.4 Results and Discussion

3.4.1 System Pressure

During the minimization of Phase I for both the nucleate and explosive boiling studies, pressure was monitored to ensure a reasonable system setup. Figure 3.4 shows the average argon vapor pressure history for the four arrangements under both the low and high temperature conditions. The initial vapor pressure for all cases oscillated around 1.15 bar, which is slightly below the experimentally determined saturation vapor pressure for argon at 90K (~1.35 bar).[113] This deviation is reasonable given the small computational domain and relatively small number of atoms. From this initial state, the pressure was allowed to evolve during Phase II as it naturally would in a closed system.

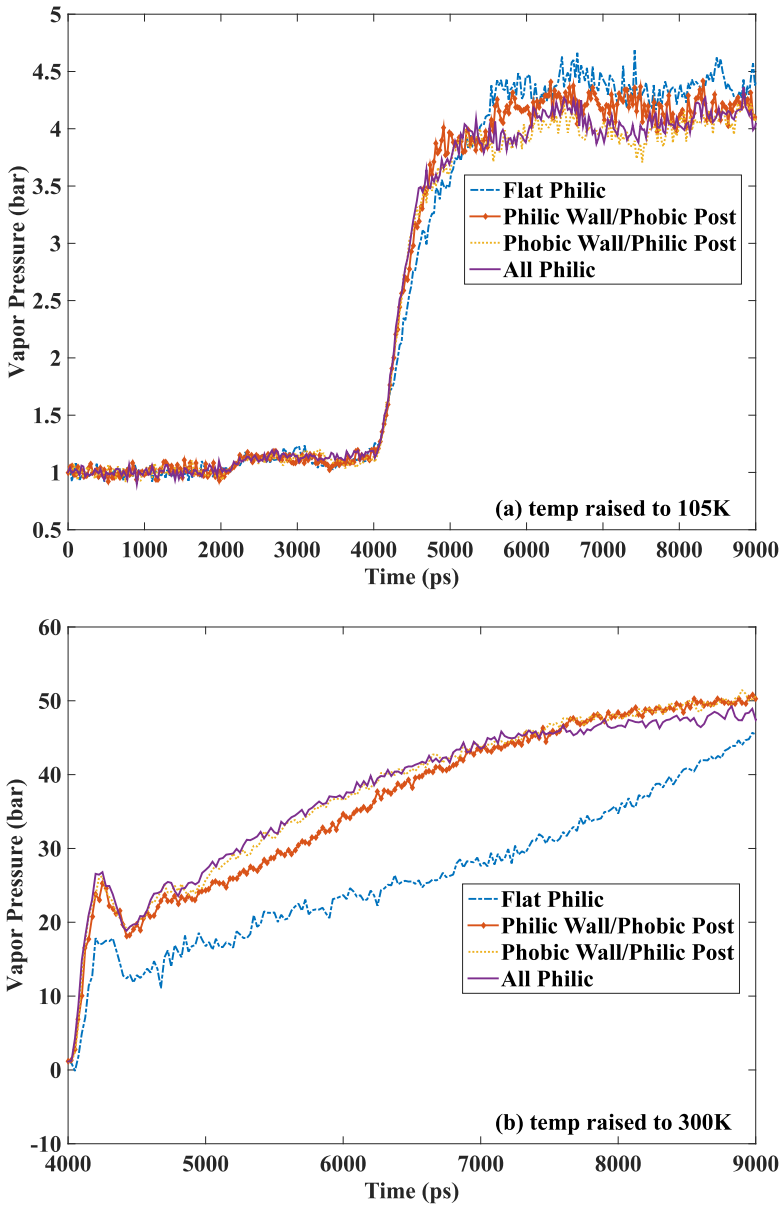

Figure 3.4: Evolution of Ar vapor pressure at a) 105 K and b) 300 K.

3.4.2 Evaporation/Nucleate Boiling

For Phase II of the low temperature boiling simulation, the copper monolayer Langevin thermostat was set to jump from 90K to 105K, resulting in the onset of evaporation/nucleate boiling. Figures 3.5(a) and (b) show the temperature history for Cu and Ar, respectively. For all four of the considered nano-patterned structures, it is seen

that the copper temperature reached equilibrium in roughly 30 ps. The argon molecules reached the target temperature quickly (~250 ps) and it can be seen in Figure 3.5(b) that the three cases with nano-pillars reached the target temperature more quickly than the Flat case, due to the extra surface area available for interaction.

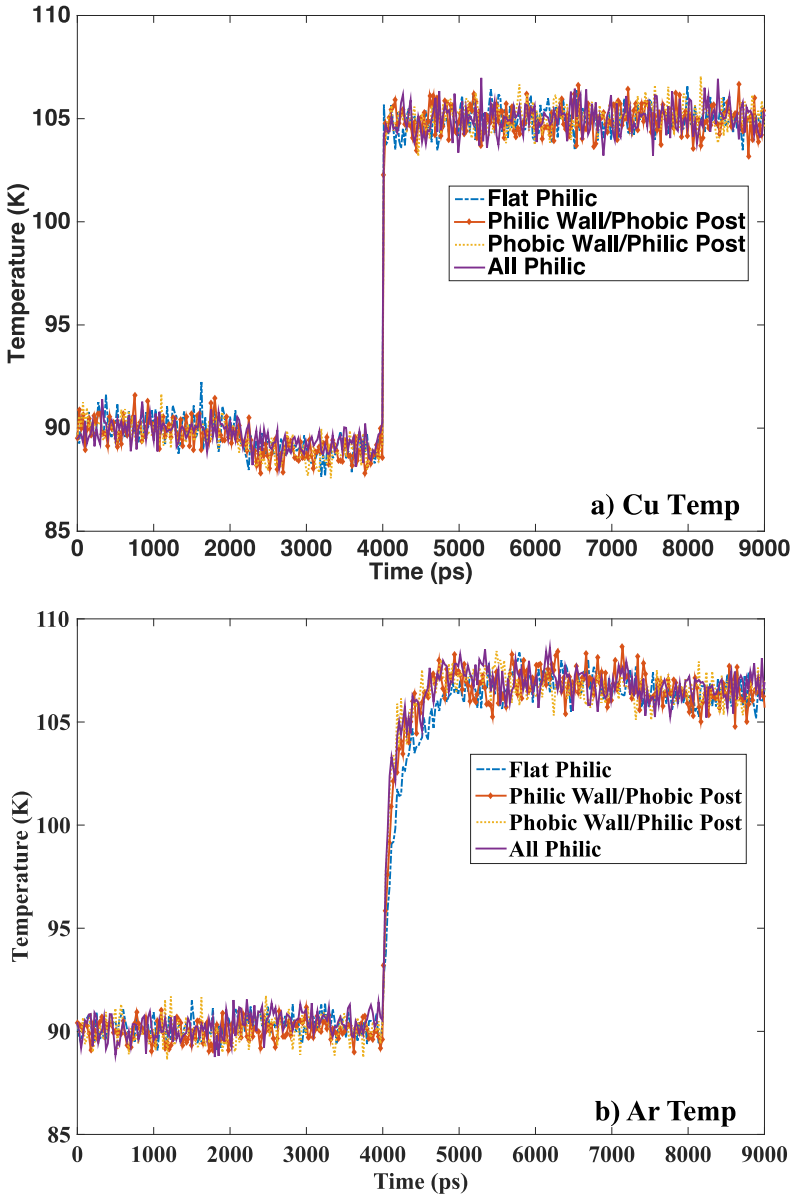

Figure 3.5: Nucleate boiling temperature history for a) Cu and b) Ar.

Figure 3.6 shows the density development for the liquid region near the copper substrate (z < 36 Å) for the low temperature case (105K), encompassing all four nanostructures. The liquid region was divided into several layers in the z-direction, and the density of each layer was recorded. The layer height used was ~1.5l_C, where l_C is the initial lattice constant for the argon liquid. Layer heights of 0.75l_C and 3.0l_C were also tested, and gave no change in density results. As can be seen, the Philic Wall/Phobic Post case has the lowest density in this region while the All Philic case has the highest (it should be noted that the density profiles shown omit the density layer encompassing the liquid surface, in order to eliminate liquid level effects). The steady-state density for the Philic Wall/Phobic Post case was 1.2596 g/cm^3, while for the Flat Philic, Phobic Wall/Philic Post, and All Philic cases the steady densities were 1.270, 1.2809, and 1.3053 g/cm^3, respectively. This could possibly be due to the argon-phobic nanostructures, which have a somewhat larger total surface area in contact with argon than the argon-philic base wall (~4,600 vs. ~4,400 Å^3, respectively). All cases follow nearly identical trends throughout the duration of the simulation.

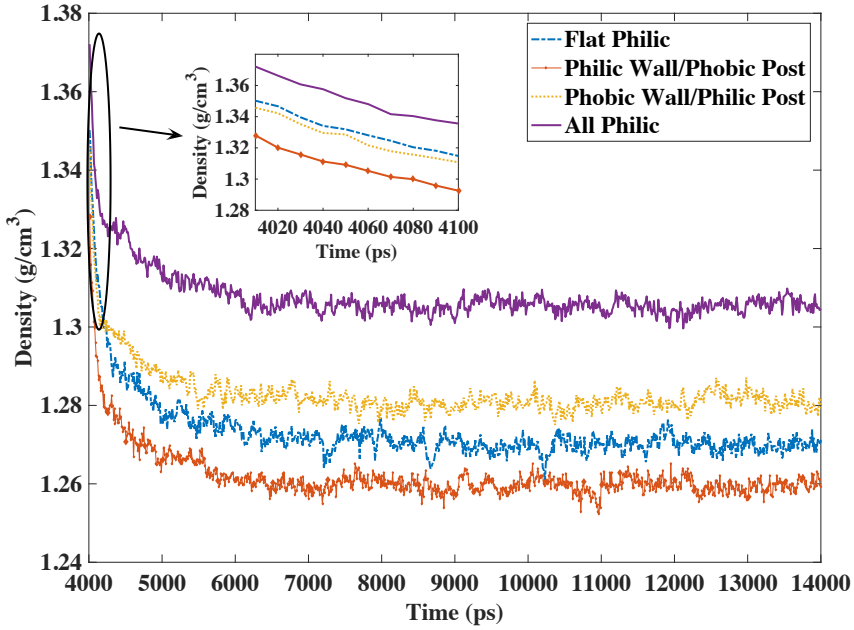

Figure 3.6: Ar density profiles (low temperature cases).

Due to the small scale of this study it is very difficult to visually and dynamically track any possible bubble formation, thus each argon atom was differentiated between liquid and vapor states. In order to determine the number of argon vapor atoms present in both the liquid and vapor regions of the simulation domain, a criterion was constructed based on atom coordination numbers. The threshold coordination number would serve as the demarcation point between an argon atom being either liquid or vapor. In order to determine this coordination number a separate simulation was run of 5,324 argon atoms in a 63.56 Å cubic simulation box (all dimensions were periodic). The simulation was run in an isothermal-isobaric (NPT) ensemble at liquid-vapor equilibrium conditions for argon at 90K, and an average coordination number of 12 atoms (within a cutoff distance of 5.3 Å) was determined in this study. This is considerably higher than the coordination number of 6 determined in Maroo and Chung's study.[64] However during the simulation

in our study equilibrium values for density (~1.37 g/cm^3) and pressure (~1.35 bar) at 90K were confirmed, giving confidence in the accuracy of our result. Thus, in the main boiling simulations if an argon atom has less than 12 neighbors within a radius of 5.3 Å it is considered a vapor atom, otherwise it considered a liquid atom. This number can be used in subsequent studies to monitor vapor formation in argon boiling, and improve simulation/detection of early bubble formation.

Based on this new criterion, an evaporation ratio was calculated. The ratio uses the number of vapor atoms at any given timestep and normalizes it by the the average number of vapor atoms present during the Phase I equilibration. Figure 3.7 shows the evaporation ratio in the vapor region (above the liquid film) for each case. This shows that the All Philic case has the highest share of Ar atoms within the vapor region, while the Flat Philic case by far has the lowest. The results for cases that include nanostructures correlate positively with the density data of Figure 3.6, i.e. the All Philic case has a higher evaporation ratio than the other cases as well as a higher liquid density. This makes sense, as a higher liquid density results from fewer vapor atoms within the liquid region and necessitates a greater amount of evaporated atoms. Although the Flat Philic case does not have the lowest density, it does have the lowest evaporation ratio due to the lack of additional surface area for heat transfer. Figure 3.8 shows the evaporation ratio in the liquid, and here we see that the Flat Philic case actually has the highest value. Combined with Figure 3.7, we can see that in the Flat Philic case the vapor atoms that lie within the liquid region are not able to escape into the vapor region, indicating reduced capacity for heat transfer. The All Philic case having the highest evaporation ratio in the vapor region (and the lowest in the liquid region) suggests greater heat flux due to the

higher capacity for kinetic energy transfer between the more densely packed liquid atoms.

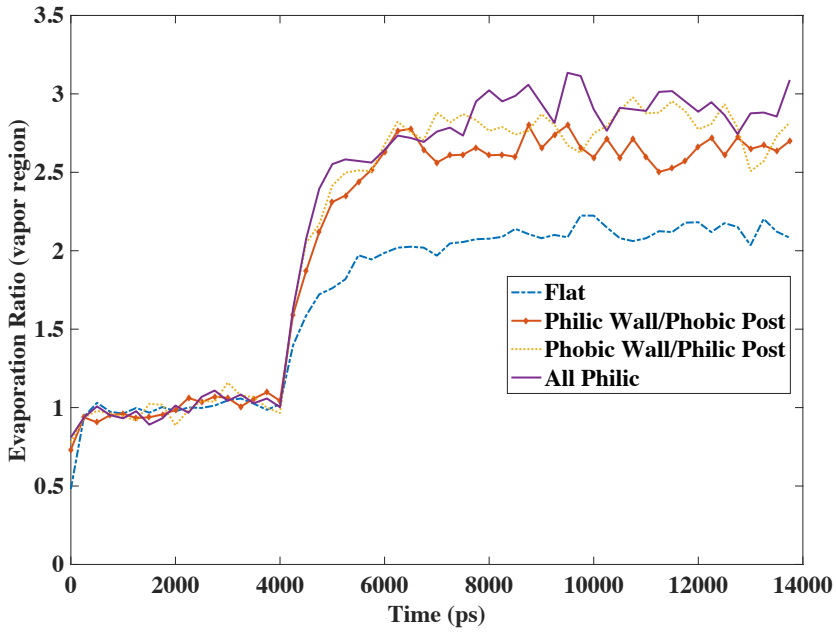

Figure 3.7: Evaporation ratio in vapor region (low temperature cases).

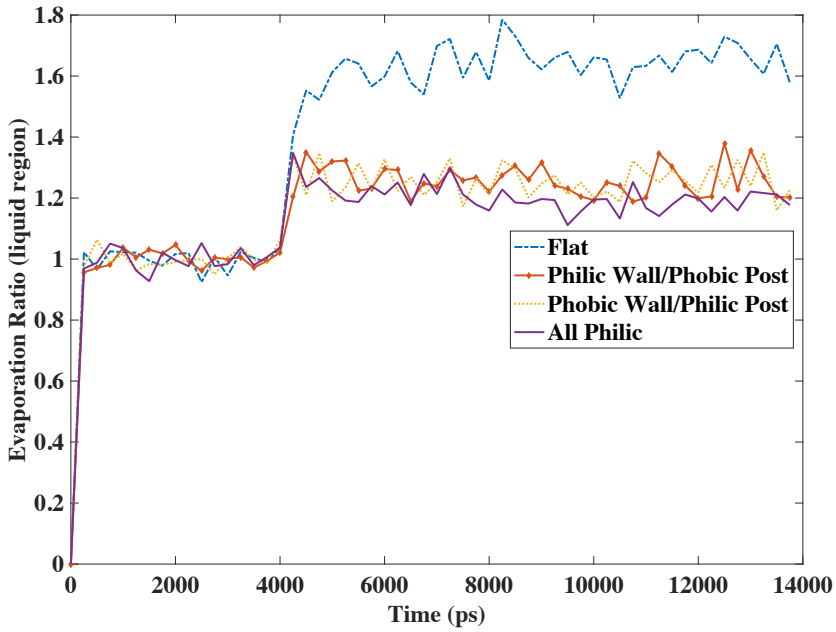

Figure 3.8: Evaporation ratio in liquid region (low temperature cases).

A higher initial peak and average heat transfer rate for the All Philic case are shown in Figure 3.9 (which shows a cumulative running average). As can be seen, after ~500 ps the initial average heat flux oscillation begins to flatten out and reach a quasi-steady state, with the All Philic case maintaining the highest value throughout the entire simulation. The increased surface area combined with the favorable interaction potential allows for better wetting and transfer of kinetic energy from wall to liquid. At the end of the simulation the heat flux in the All Philic was over 20% higher than that of the other cases. The initial peak for the Philic Wall/Phobic Post case rises more quickly than the Flat Philic case, while the Phobic Wall/Philic Post case shows the slowest rise.

A somewhat surprising result is that the average heat flux in the Flat Philic case was similar to or greater than those of the Philic Wall/Phobic Post and Phobic Wall/Philic Post cases. This is most likely due to the greater initial number of argon atoms in the Flat Philic case which can kinetically transfer more energy. At the end of the simulation the Flat Philic and Philic Wall/Phobic Post cases had nearly identical heat flux values ($\sim 7 \times 10^7$ W/m^2) while that of the Phobic Wall/Philic Post case was slightly lower ($\sim 6.5 \times 10^7$ W/m^2). This is contrary to previous experiments,[6,50] which found that hydrophobic islands (structures) situated on top of hydrophilic base walls give the best heat flux performance. However, it should be noted that these experiments considered 'flat' surfaces with maximum roughness heights on the order of tens of nanometers and microscale structures, which are much larger than the scale considered in these simulations. It is possible that on the nanoscale bubble formation plays a less important role than kinetic energy transfer due to the extremely small size of vapor nuclei and reduced opportunity for bubble coalescence.

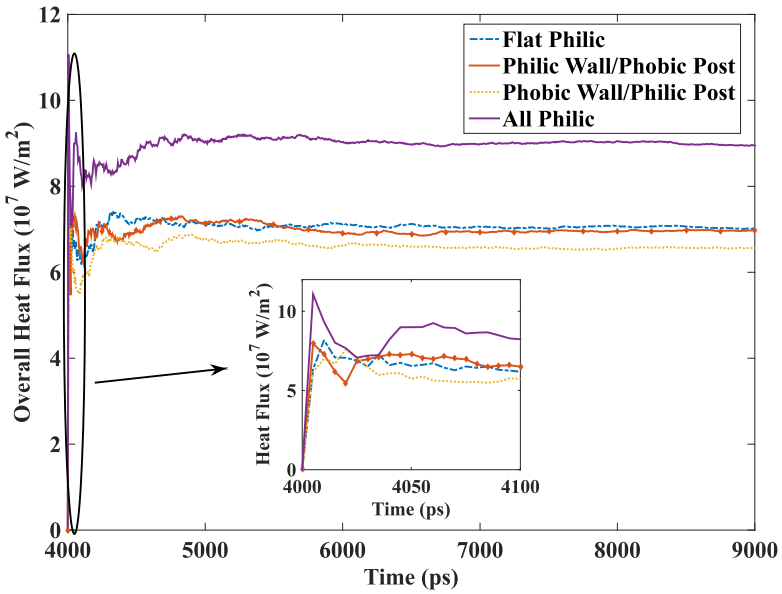

Figure 3.9: Average heat flux (low temperature cases).

In all cases, the maximum instantaneous heat flux values seen were on the order of 10^8 W/m^2, which is consistent with the simulation results of Maroo and Chung,[64] which showed a maximum instantaneous flux on the order of ~6x10^8 when heating argon liquid on a flat platinum substrate to 130K, as well as the work in[59] for low substrate temperatures. It is also in line with the predictions of evaporative kinetic theory.[114] Based on this theory the approximate limit of attainable heat flux is given by

$$q''_{\max} = \rho_v h_{fg} \sqrt{RT / 2\pi} \tag{3.2}$$

where ρ_v is the saturated vapor density, h_{fg} is the latent heat of vaporization, R is the ideal gas constant (per unit mass), and T is the absolute temperature. For argon at 105K, Equation 3.2 predicts a value of ~2x10^8 W/m^2, while the simulations presented here give maximum instantaneous fluxes between ~3-5x10^8 W/m^2.

3.4.3 Explosive Boiling

For Phase II of the high temperature boiling simulation the thermostat was set to jump from 90K to 300K, well above the boiling point of argon, to induce explosive boiling. Figure 3.10 shows the temperature profile for each case. The equilibration time for the copper wall was ~100-200 ps, while the argon did not reach equilibrium within 5 ns. This is because during explosive boiling, a high pressure vapor layer forms close to the copper wall, which acts to force the bulk argon liquid away from the substrate heat source (in the *z*-direction). This vapor is also insulating due to its low density, and restricts heat transfer. This can be seen as the temperature drop at around 200 ps (for all cases), before the steady climb toward the thermostat temperature. The rate of temperature change is similar for all cases, excluding the Flat Philic case, which has a much slower rate of temperature increase. This most likely indicates a slower rate of heat transfer, while the All Philic case (having the highest temperature), shows the highest heat transfer rate.

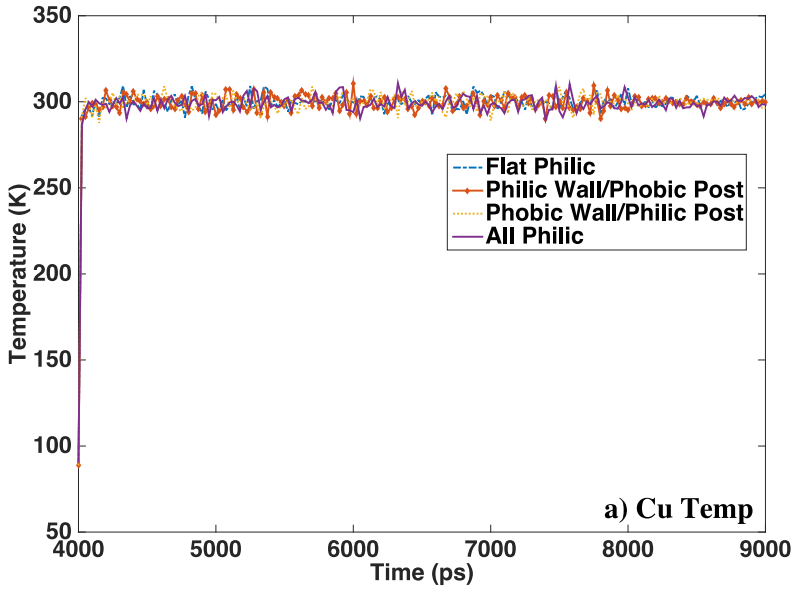

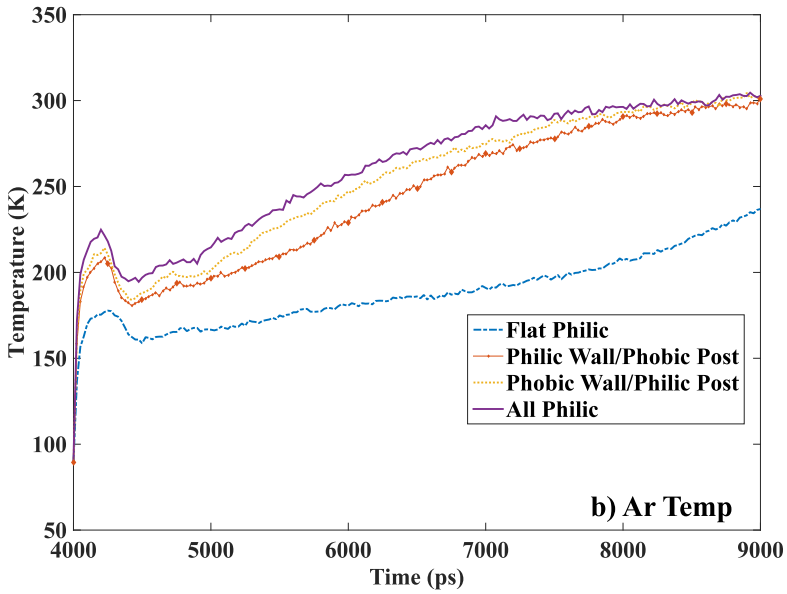

Figure 3.10: Temperature history of a) Cu and b) Ar (high temperature cases).

Figure 3.11 shows the coverage of argon atoms on the copper wall at the end of the simulation. As expected, the Flat Philic and All Philic cases exhibit the best coverage, while larger gaps in coverage can be seen in the Phobic Wall/Philic Post and Philic Wall/Phobic post cases. Since in the explosive boiling case the vapor layer forms quickly, having an argon-philic substrate would help maintain a number of argon atoms near the copper to increase the amount of kinetic energy transfer. This would especially hold true for the Phobic Wall/Philic Post and All Philic cases, as their argon-philic nanostructures extend higher into the simulation box and have a larger surface area than the base wall. Figure 3.12 shows the argon density profile at different times for the (a) Flat Philic and (b) All Philic cases. The movement of the peak density value in the positive *z*-direction confirms the upward movement of the bulk liquid due to the high-pressure vapor layer formation at the wall surface. In the Flat Philic case the density peak at 4,610 ps is lower in the simulation box than at 4,410 ps due to the bulk liquid

rebounding off of the top of the simulation box and subsequently traveling in the negative *z*-direction. Comparing the two cases, one can see that in the All Philic case the liquid slug travels a greater distance from 4,010 to 4,210 ps and has a much smaller and less sharp density peak. This occurs due to improved heat transfer, which produces a higher-pressure vapor layer and acts to dissipate the liquid slug more quickly. In both cases the density peak decreases with increasing time, though this effect is much more pronounced in the All Philic case.

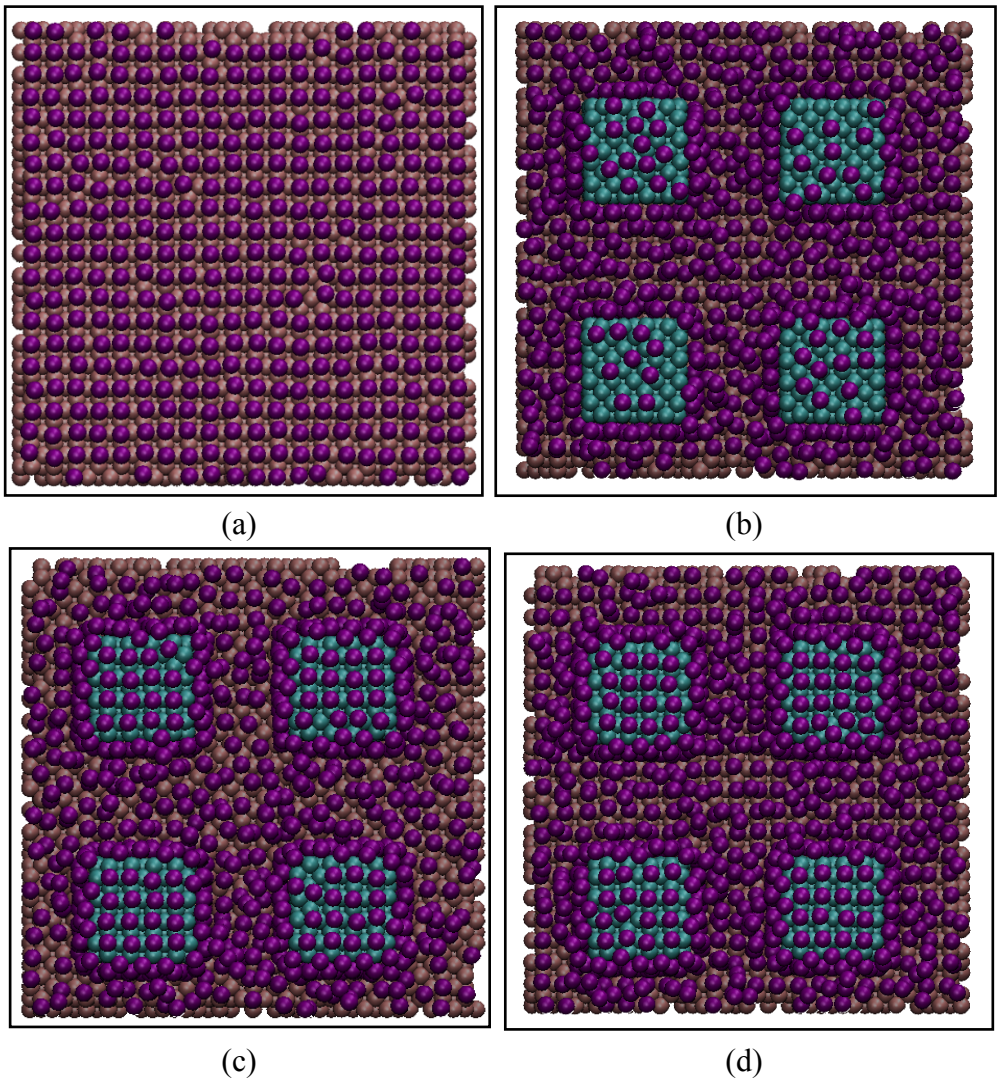

Figure 3.11: Nano-structure coverage: (a) Flat Philic; (b) Philic Wall/Phobic Post; (c) Phobic Wall/Philic Post; and (d) All Philic (high temperature cases).

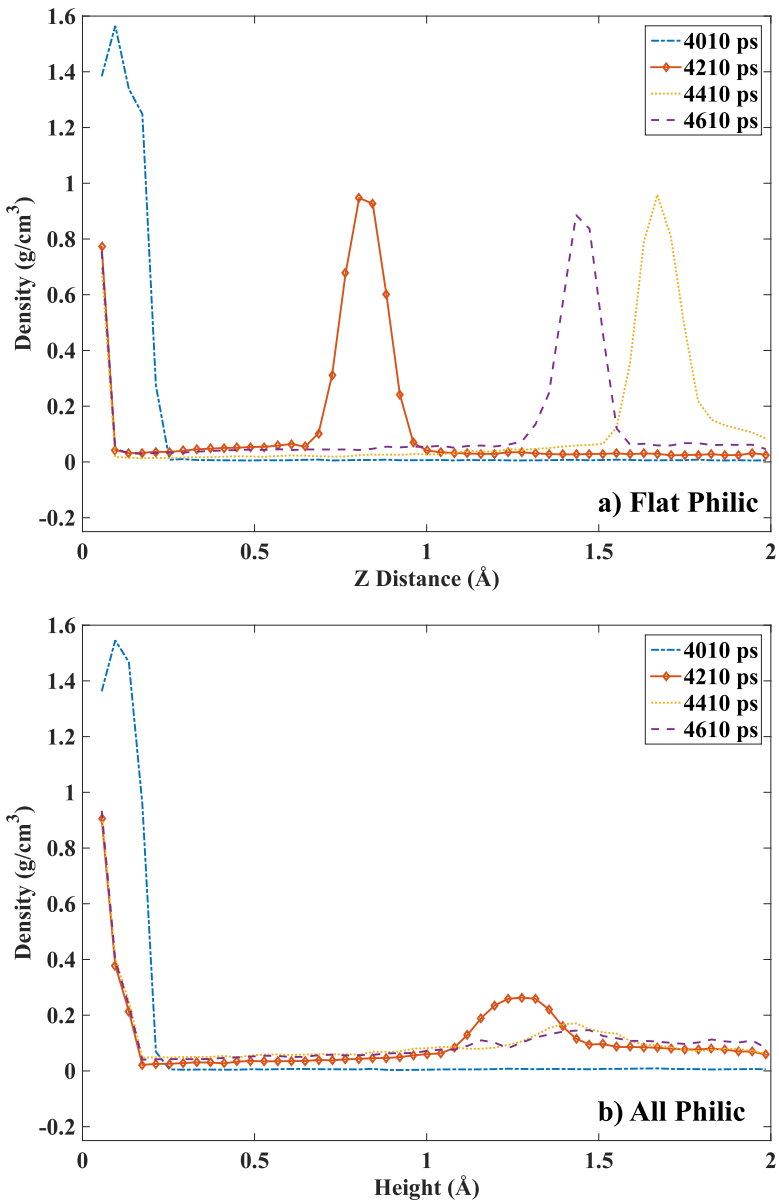

Figure 3.12: Ar density profiles at different times (high temperature cases).

Figures 3.13 and 3.14 show the evaporation ratio and average overall heat flux versus time, respectively. For the evaporation ratio data shown in Figure 3.13 the vapor atoms were tracked in the upper region of the simulation in order to remove the influence of the adsorbed atoms and extra surface area of the nano-pillars. As in the low temperature cases, the All Philic case shows the best evaporation results. Within roughly

500 ps of the start of Phase II the All Philic evaporation ratio reaches a steady state value, due to quick vaporization of the liquid film. Compare this to the Flat Philic case, which has a lower evaporation ratio and requires more time (~2500 ps) to reach a steady state. From these results as well as the density data it is clear that as compared to the nano-structured surfaces, the liquid slug in the Flat Philic case takes much longer to fully dissipate due to inhibited heat transfer. In Figure 3.14 we see a local maximum (and minimum) in the first 10 to 40 ps in which the All Philic case shows slightly higher heat flux, shortly after which the maximum heat flux is reached after ~200 ps. Here once again the All Philic case exhibits the highest heat flux, which it maintains for the entire simulation. At the end of the simulation the average heat flux for the All Philic case was ~1.5×10^8 W/m^2, with the next highest heat flux of ~1.3×10^8 W/m^2 coming from the Phobic Wall/Philic Post case. Again, this could be due to the enlarged surface area of the philic nanoposts as compared to the base wall. The peak instantaneous heat flux attained in these scenarios, which ranged from ~$6\text{-}10 \times 10^8$ W/m^2, was again of the same order as those attained in previous simulations[64,69] and one order of magnitude less than other reports[59,68] which both used argon as the heat transfer fluid (although in Hens et al.[68] a thicker Pt substrate and smaller number of argon atoms were used).

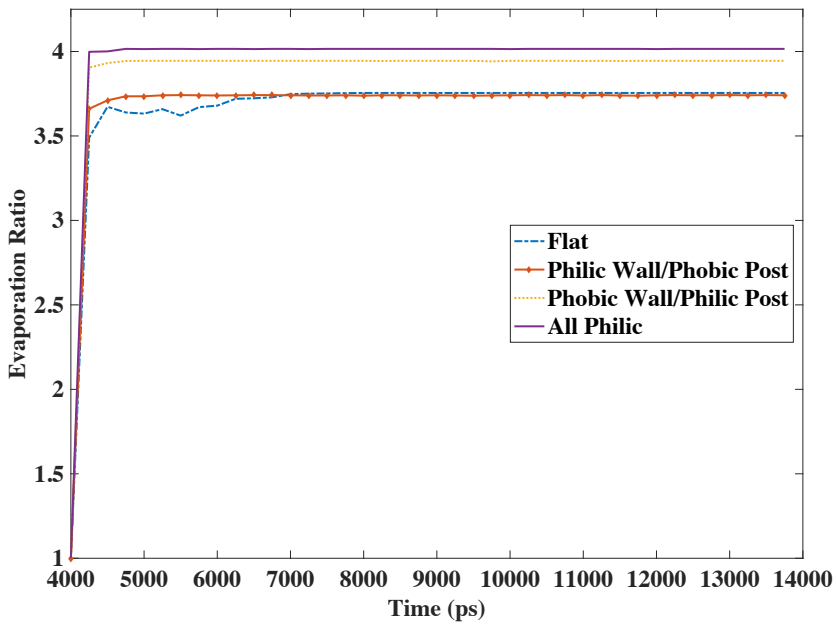

Figure 3.13: Evaporation ratio (high temperature cases).

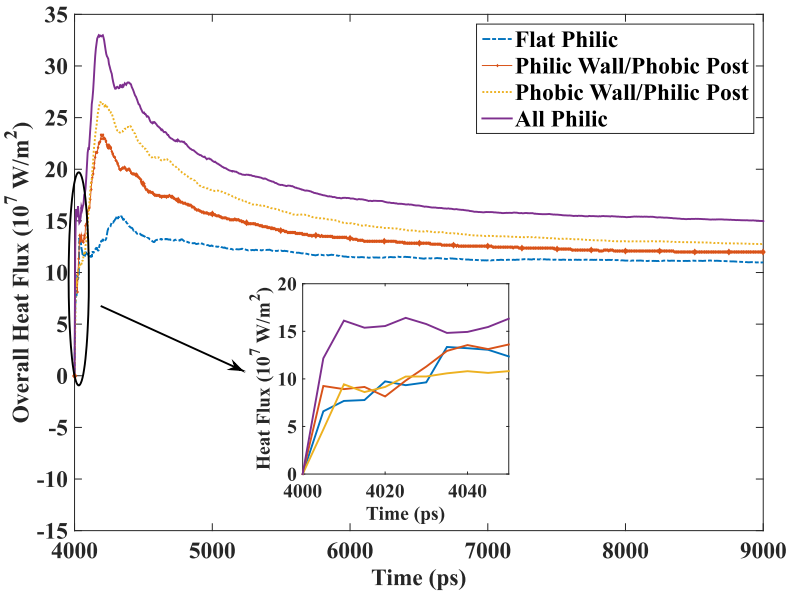

Figure 3.14: Average heat flux (high temperature cases).

3.5 Conclusions

Nucleate and explosive pool boiling heat transfer of a liquid Ar thin film on Cu wall with different nano-patterns and surface conditions has been investigated via MD simulation. After monitoring the temperature, density, evaporation, and energy histories for each case the following observations have been made:

- In the nucleate boiling regime, heat flux and evaporation are most improved with the use of both a philic base wall and philic pillars (i.e. the All Philic case), with a steady heat flux of ~8.9×10^7 W/m^2 (and a maximum instantaneous flux of ~5.1×10^8 W/m^2). Also, in the Philic Wall/Phobic Post and Phobic Wall/Philic Post cases, for a given film thickness the use of phobic substrate seems to decrease some of the heat flux increase due to surface area increase (as compared to the Flat Philic case). However it must be noted that heat flux in the Flat Philic case benefits from having a greater number of argon atoms in this study.
- During explosive boiling, once again the All Philic case showed better performance than all other cases in terms of evaporation number and heat flux, with maximum instantaneous fluxes nearing 1×10^9 W/m^2.
- In all explosive boiling cases a non-evaporating layer is present, with a thickness dependent on the philic/phobic nature of the substrate.
- A new, accurate coordination number was established in this study to differentiate between Ar liquid and vapor atoms. This criterion can be used in future studies to monitor evaporation, as well as aid in the determination of early, nanoscale bubble nucleation.

- A typical 2.5σ cutoff in MD simulations could under-predict steady heat flux by about 8.7% in comparison with 8σ cutoff. A 4σ cutoff improves the steady heat flux prediction to within 4.9% with a CPU time increase of roughly 2.5x. A 6σ cutoff could improve the heat flux prediction to within 2.4%, but increases the CPU time by ~6.6x.

Chapter 4

Wettability and Pitch Effects on Evaporation and Pool Boiling Heat Transfer

4.1 Introduction

With advances in micro- and nanoscale manufacturing methods, the substrate topologies available for use in pool boiling applications are increasing. As this control on the nanoscale increases it is vital to characterize the effect that these altered substrates have on the phase change process. This knowledge will facilitate the manufacture of better designed substrates and will allow more rapid removal of heat flux from ever more powerful devices.[115-118] While investigations have been carried out to detail certain pitch effects on pool boiling heat transfer,[49-50] these studies were experimental in nature and necessarily focused on macroscale boiling. Thus there is a dearth of information regarding these effects in nanoscale boiling heat transfer.

The effect of liquid contact angle is another important consideration, as it is intertwined with pitch, surface roughness, and other factors and affects the overall wettability of a liquid/substrate combination. Contact angle and its effect on evaporation and CHF have previously been investigated in simulations[119] and experiments,[29,48] and others[30,120] proposed correlations for pool boiling CHF that incorporated contact angle, amongst other variables. In general these studies showed that CHF is adversely affected by large contact angles (hydrophobicity), while smaller (hydrophilic) contact angles increase the heat transfer coefficient and improve CHF. It is difficult, however, to

perform these types of experiments on the nanoscale while controlling for a number of different variables. On such a small scale larger bubble sizes (radii >= 1 micrometer) are not allowed to form, and the dynamics and heat transfer mechanisms can be very different.

Thus, Molecular Dynamics (MD) simulations have been utilized to investigate the effect of equilibrium contact angle on maximum heat flux during nanoscale evaporation and pool boiling. In the context of this work maximum heat flux refers to the highest heat flux (to the liquid film) achieved before the onset of explosive boiling/dry out. In this study, the substrate topology (roughness), temperature, and pressure were all controlled in order to more clearly view the effect of contact angle on the maximum heat flux. To date many MD studies have been conducted on both homogeneous and heterogeneous systems in order to investigate heat transfer, phase change, flow properties, etc. Several studies[68,105,106] have used flat substrates to investigate evaporation, effect of wettability, etc. and there have more recently been some studies focused on boiling/evaporation on nano-structured substrates using differently shaped nano-structures and nano-structures with different wettability.[66,67,107] Nevertheless, to date no known MD study has been conducted looking at maximum heat flux as a function of contact angle and pitch variations.

In this study, a nanostructured copper substrate is used to heat a liquid argon film. Several different scenarios were investigated, including eight different contact angles, ranging from hydrophilic to hydrophobic, and six different pitches. Simulation of these arrangements has allowed us to compare the boiling and evaporation characteristics of

each to determine heat transfer trends, and investigate mechanisms by which the heat transfer enhancements take place.

4.2 Simulation Method

The system used in the main simulations was comprised of a horizontal solid copper wall with vertically oriented nano-pillars, a layer of liquid argon, and argon vapor molecules in a simulation box with varying dimensions based on pitch, which are detailed in Table 4.1. Figures 4.1(a), (b) and (c) detail the overall configuration of a typical simulation and the enlarged views of the copper wall and nano-pillars, respectively. The wall at the bottom of the simulation box consisted of a base of five monolayers of solid copper. As in previous works, this was deemed enough to accurately act as a conduction layer for liquid heating.[69,108,121] The nano-pillars were arranged on the base wall in a symmetrical fashion. The nano-pillars were fifteen monolayers high and each measured 25.3 x 25.3 x 25.3 Å. The base wall and nano-pillars were arranged in an FCC lattice structure corresponding to the (100) plane. For these copper atoms a lattice constant of 3.615 Å was used, corresponding to a density of 8.9 g/cm^3. Fifteen monolayers of argon molecules were placed just above the copper base wall, covering both the wall and pillars. For the argon liquid atoms a lattice constant of 5.256 Å was used, corresponding to an initial density of 1.4 g/cm^3. Finally, argon vapor atoms (corresponding to a density of 5.77x10^{-3} g/cm^3) were placed above the liquid, filling the rest of the simulation box.

Table 4.1: Simulation domain parameters based on pitch (¼ model)

Pitch	Dimensions	# Cu Atoms	# Ar Atoms
21.7Å	47.0 x 47.0 x 440Å	3,160	2,135
27.1Å	52.4 x 52.4 x 440Å	3,790	2,588
45.2Å	70.5 x 70.5 x 440Å	5,273	5,442
65.1Å	90.4 x 90.4 x 440Å	7,720	9,424
85.0Å	110.3 x 110.3 x 440Å	10,990	13,757
106.6Å	131.9 x 131.9 x 440Å	15.010	20,777

Interactions between all atoms were modeled with the standard 12-6 Lennard-Jones potential of Equation 2.7. To reduce the computational cost an r_c equal to $4\sigma_{Ar\text{-}Ar}$ was employed.

Before the main simulation runs, separate simulations were first carried out using altered interaction potential parameters in order to establish the different contact angles. The $\varepsilon_{Cu\text{-}Ar}$ interaction value for the 106° contact angle (i.e. $\varepsilon_{Cu\text{-}Ar}$ = 0.0653 eV) was calculated via the normal Lorentz-Berthelot mixing rules of Equation 2.8, however for most cases the Cu-Ar potential well depth was altered in order to change the interaction strength, and consequently the contact angle. The altered potential well depth is calculated as follows:

$$\varepsilon_{Cu-Ar} = c \cdot \sqrt{\varepsilon_{Cu}\varepsilon_{Ar}} \tag{4.1}$$

where *c* is a user-chosen numerical constant. Each case is meant to simulate a copper substrate with altered wetting characteristics (via surface modification, coatings, etc.).

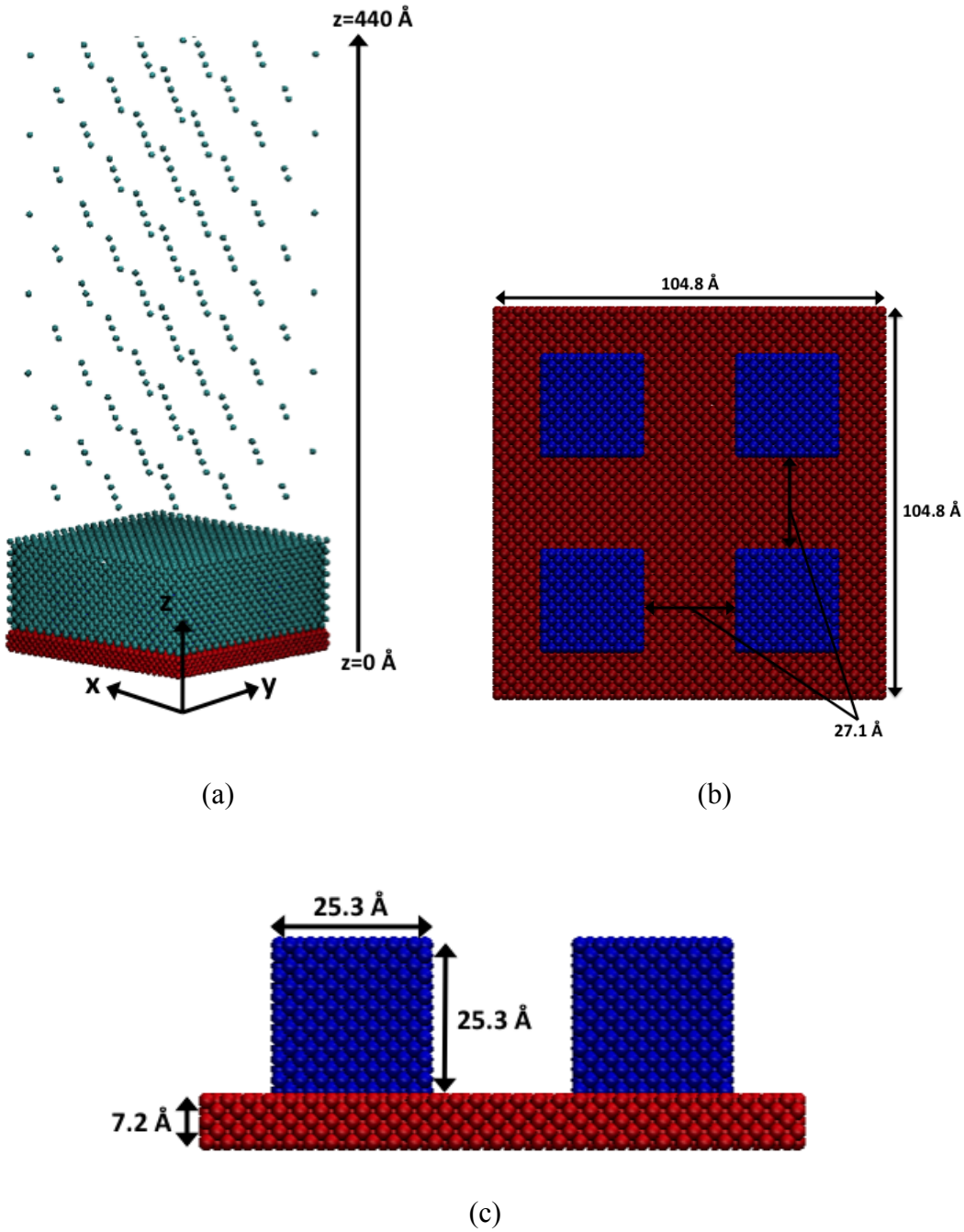

Figure 4.1: Sketch of the 27.1Å pitch simulation model: (a) overall simulation configuration (1/4 was considered in computation due to symmetry), (b) and (c) enlarged views of the copper substrate and nano-pillars (Units: Å).

Table 4.2 details the potential parameters and the resulting contact angles of 0°, 57°, 76°, 92°, 103°, 116°, 121°, and 127°. A smaller ε value indicates a weaker, or more hydrophobic, interaction (i.e. a larger contact angle). For clarity, each case will be referred to with a CA followed by its contact angle value, i.e. CA-0, CA-57, etc.

Table 4.2: Potential well depth parameters and resultant contact angles

Case	*c*	$\varepsilon_{Cu\text{-}Ar}$ (eV)	Contact Angle (deg)
CA-0	0.09	0.0059	0
CA-57	0.08	0.0052	57
CA-76	0.07	0.0046	76
CA-92	0.06	0.0039	92
CA-103	0.05	0.0033	103
CA-116	0.04	0.0026	116
CA-121	0.03	0.0020	121
CA-127	0.02	0.0013	127

The separate contact angle simulations were performed on a flat copper substrate with roughly the same dimensions as the 85.0 Å pitch substrate used in the main heating simulations. A block of liquid argon particles was initially placed just above the substrate while argon vapor atoms filled the rest of the simulation box. The liquid block runs the entire length (in the *y* direction) of the simulation box, resulting in a cylindrical 'infinite length' droplet. From previous work[122] this is shown to better approximate the macro contact angle in nanoscale studies. The simulation was run for 3.5 ns with a 5 fs time step while a Langevin thermostat was applied in order to keep all atoms at 90K. In order to simulate the resulting contact angle, the simulation domain was first divided into

a grid of boxes ~2 Å per side, and the average density was monitored in each and written to a file every 250 ps. The last four data points were then averaged to determine the final density profile, an example of which is shown in Figure 4.2. As in Isaiev et al.[122] a small portion of the liquid region near the wall was excluded to remove any influence of the copper wall on the contact angle calculation. Once the profile was calculated, an algebraic circle fit was used to estimate the droplet boundary as well as its intersection with the horizontal substrate. With the circle and intersection point defined, a contact angle could be calculated.

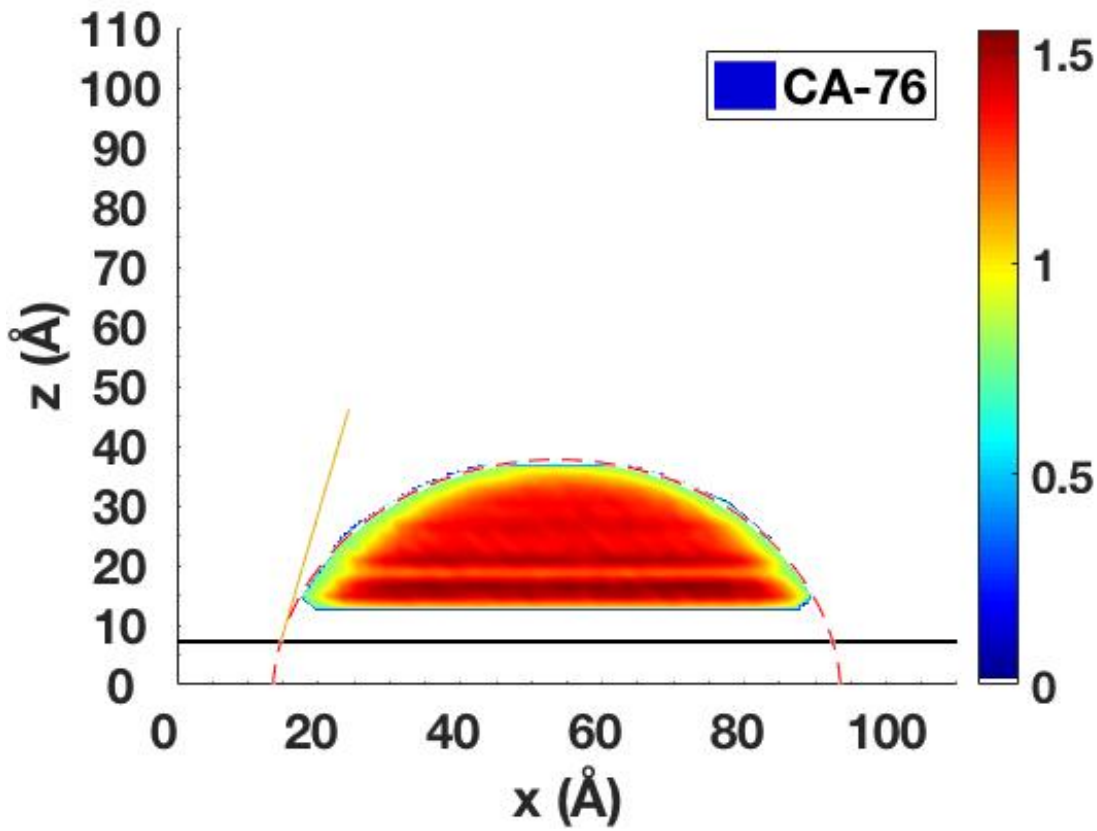

Figure 4.2: Density map of the CA-76 simulation.

After the contact angles were established, the evaporation/boiling simulations were carried out in two phases. Phase I consisted of initialization and equilibration, and was itself broken down into three sub-phases. First an energy minimization was carried out to determine the minimum energy state of the initial configuration. Once completed, a Langevin thermostat was imposed on all atoms to establish an equilibration temperature of 90K. After 3 ns the thermostat was removed, and the system was allowed to evolve under the microcanonical ensemble (NVE) for an additional 1 ns. Once the system temperature and energy are stable Phase II commences and the temperature of the system is steadily increased from 90K to 300K over the course of 7.5 ns (not including the previous 4 ns of Phase I), in order to move fully through the explosive boiling regime and show the full nanoscale boiling curve. In this phase the Langevin thermostat was applied to only the second monolayer of the copper base wall, while the first (bottom) layer was kept immobile to prevent atoms from moving through the bottom of the simulation domain. The upper three levels of the copper atoms were maintained in the NVE ensemble and allowed to interact as they normally would via the Lennard-Jones potential. Both phases used a velocity Verlet integration algorithm with a 5 fs time step.

The simulation domain is periodic in the four sidewalls of both the x and y directions, which helps to prevent finite size effects of the small simulation domain. To reduce the computational time required, 1/4 of the arrangement shown in Figure 4.1 (i.e. only one nano-pillar) was used for the simulations. The results from the smaller domain were compared to the four nano-pillar domain and showed no significant differences in pressure, temperature, density, or heat flux. The CPU time required was reduced by

42%, with the larger domain requiring 32.1 hours and the smaller domain only requiring 13.6 hours. The top of the simulation domain is a fixed, adiabatic boundary, which means that any atom that moves outside the boundary by a certain distance is placed back inside the boundary by that same distance, while having the sign of its z velocity reversed. All simulations were run using LAMMPS software (version 16 Feb 2016), a classical molecular dynamics code based on Plimpton's work,[111] while system visualization was performed with VMD v1.9.1.[112] All simulations were performed on a workstation cluster of 75 2.6 GHz Intel Sandy Bridge 2670 CPUs, with typical runs requiring 6.7 to 21.8 hours of run time (depending on pitch) and 4-9 MB of memory per processor.

4.3 Results and Discussion

During Phase I equilibration the average pressure in the *z* direction was monitored in order to determine system stability. Pressure was calculated via the following formula:

$$P = \frac{Nk_B T}{V} + \frac{\sum_i^N r_i \cdot f_i}{d_n V} \tag{4.2}$$

where d_n is the system dimensionality (in this case 3). The equilibration is meant to take place at atmospheric pressure conditions, while during Phase II the pressure is allowed to evolve as it normally would in a closed system. Figure 4.3 shows the *z* component of the pressure in the vapor region (i.e. $z > 75$Å) for both Phase I and II of the 27.1Å pitch case. As can be seen, most cases maintain a vapor pressure of about 1 bar during the 4 ns of Phase I before showing a relatively steady pressure increase during Phase II. The vapor

pressures recorded are in line with those seen in previous experimental works.[113] CA-0 through CA-116 are grouped together until roughly 6 ns, when separation starts to occur. In general the more hydrophilic (lower contact angle) cases exhibit higher vapor pressures as the temperature rises, which suggests increased evaporation. This holds true for all pitches considered in this study.

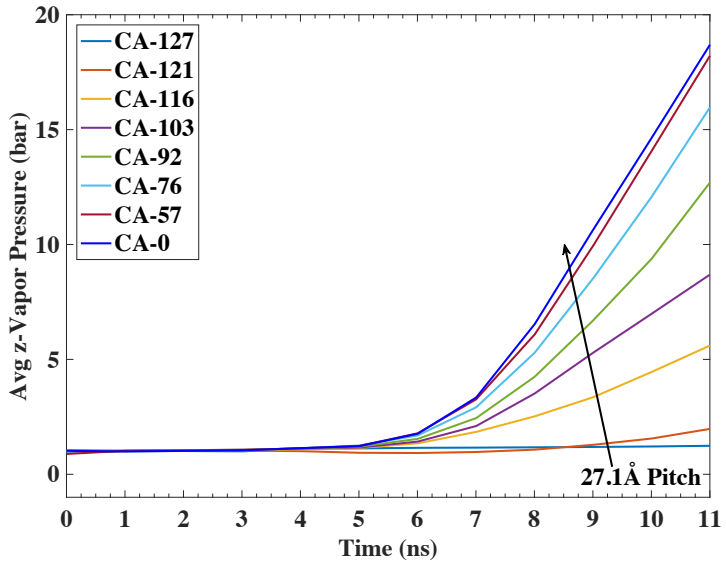

Figure 4.**3:** Ar *z*-vapor pressure evolution.

Figures 4.4(a) and (b) show the temperature history for copper and argon respectively. As expected, the copper temperature is virtually the same for all cases, and after the equilibration at 90 K it rises linearly to 300 K over the duration of the simulation. The argon temperature initially follows a similar path due to the slow nature of the temperature increase, however soon after Phase II begins all cases tend to follow the copper temperature less closely (there is a 10-60 K lag between the copper and argon temperatures). Again, some separation between the different cases emerges, with the

more hydrophilic cases showing a higher temperature. Between 7 and 8 ns the rate of temperature increase for most cases then begins to slow down. This occurs just after the maximum heat flux is reached, and is due to the onset of the film boiling condition and accompanying vapor layer formation for the various cases, as will be seen in later figures. After this point in certain cases there is a temperature rate increase that corresponds to the full vaporization of the liquid slug, which is ejected from the substrate during the onset of explosive boiling. These general trends hold true for larger pitches as well, though the onset of film boiling tends to occur at higher temperatures. At the 27.1Å pitch shown in the figure the CA-121 and CA-127 cases are once again anomalous, and there is no clear region where the rates of temperature increase change. This is due to the film boiling condition not being reached for these cases, though for larger pitches this is not always the case.

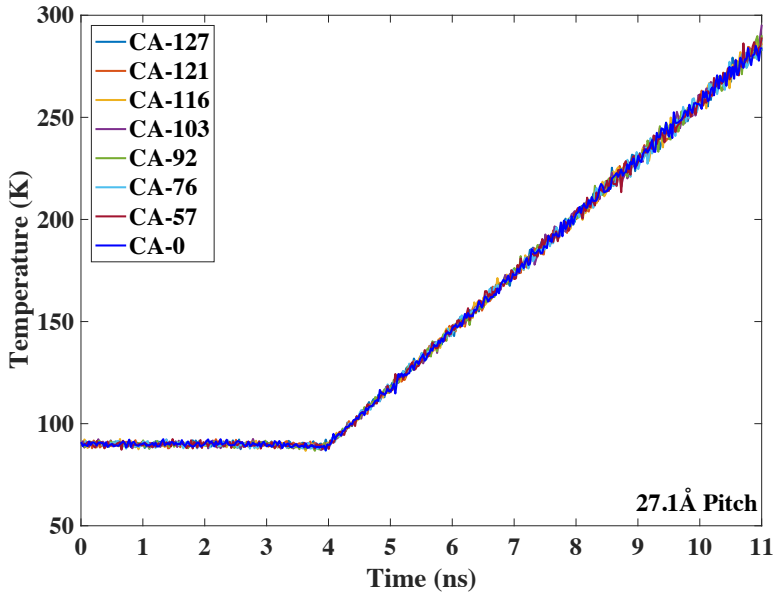

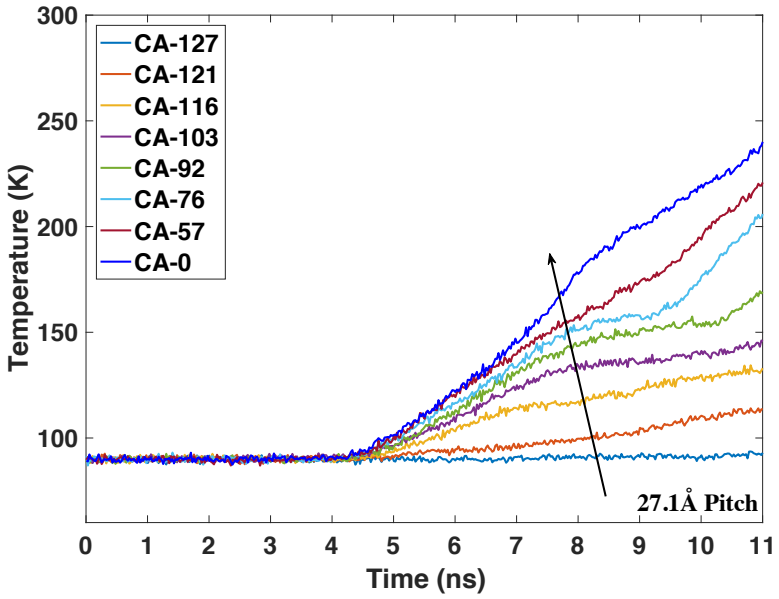

Figure 4.4: Temperature history for a) Cu and b) Ar.

Figures 4.5 and 4.6 show the density during Phase II and the evaporation ratio for both phases, respectively. To calculate the density, the simulation domain was divided into boxes encompassing the entire x and y directions and 7.9 Å in the z-direction, and the average density in each box was recorded every 10 ps. The density measurements for all cases were restricted to the liquid region (i.e. less than or equal to 50 Å). The density values at the end of Phase I/beginning of Phase II (~1-1.2 g/cm^3) show good agreement with the thermodynamic properties of argon liquid for the given pressure and temperature. From the very beginning of Phase II separation is apparent, with stronger interaction potentials (i.e. lower contact angles) predictably resulting in higher densities. The separation decreases as each case nears its point of maximum heat flux (marked by a sharp drop in density), with all but the three most hydrophobic cases in the 21.7Å pitch scenario (Figure 4.5(a)) having a density near 0.7 g/cm^3 at 7 ns. CA-116 shows an earlier

density drop due to the brief onset of a Cassie-Baxter condition, while the CA-121 and CA-127 cases begin Phase II already in the Cassie-Baxter state due to having weaker potential interactions. For comparison, Figures 4.5(b)-(d) show the 45.2Å , 65.1Å , and 106.6Å pitch scenarios respectively. In general as the pitch increases the temperature at which maximum heat flux occurs also increases, as does the density difference between contact angles. The CA-121 and/or the CA-127 cases remain anomalous until the 106.6Å pitch case, where there is a clear trend in the onset of film boiling, which increases in time as hydrophobicity increases. In the absence of nanoscale cavities/roughness this makes sense, as better heat transfer (and thus greater vapor formation) is expected from the more hydrophilic cases. The density curves begin as slowly decreasing, and then move to a region of faster exponential decrease as the maximum heat flux is approached before transitioning to a nearly constant density after the film boiling occurs. In a macro sense this exponential density decrease is due to the sharp increase in nucleation rate that accompanies the maximum heat flux condition.[123]

While the small-scale nature of these simulations makes it difficult to directly observe bubble nucleation, the rate of phase change from liquid to vapor can be viewed via the evaporation ratio, in Figure 4.6. This shows the ratio of the evaporation number at a certain time to the initial number of vapor atoms within the liquid region. To distinguish between liquid and vapor atoms the criteria based on coordination number developed in Chapter 3 was used, where any argon atom surrounded by less than 12 other atoms (within a radius of 5.3 Å) is considered a vapor atom. In this way the number of liquid and vapor atoms can be tracked and compared between cases.

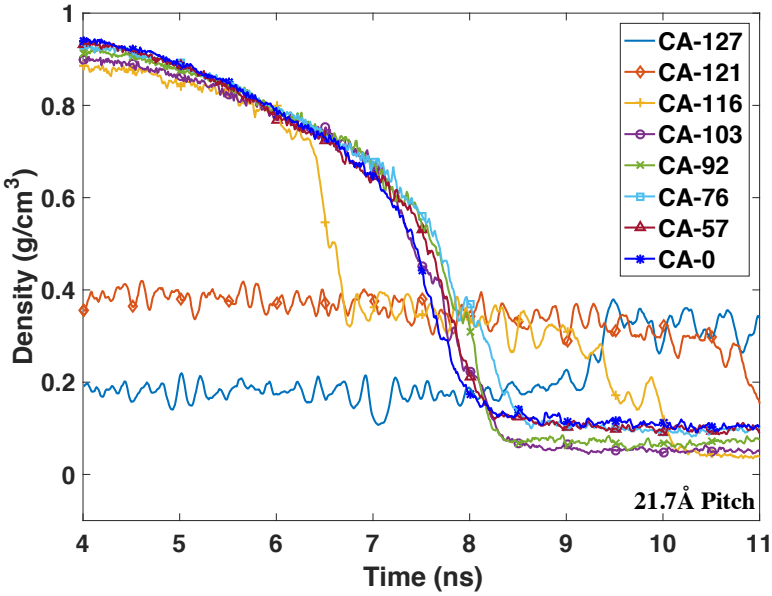
CA-127
CA-121
CA-116
CA-103
CA-92
CA-76
CA-57
CA-0
21.7Å Pitch
Density (g/cm3)
Time (ns)
1
0.8
0.6
0.4
0.2
0
4
5
6
7
8
9
10
11

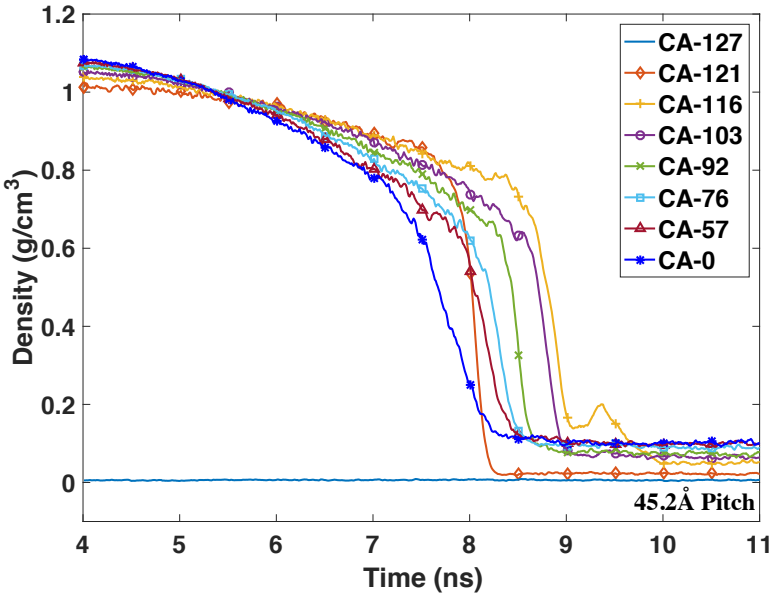
CA-127
CA-121
CA-116
CA-103
CA-92
CA-76
CA-57
CA-0
45.2Å Pitch
Density (g/cm3)
Time (ns)
1.2
1
0.8
0.6
0.4
0.2
0
4
5
6
7
8
9
10
11

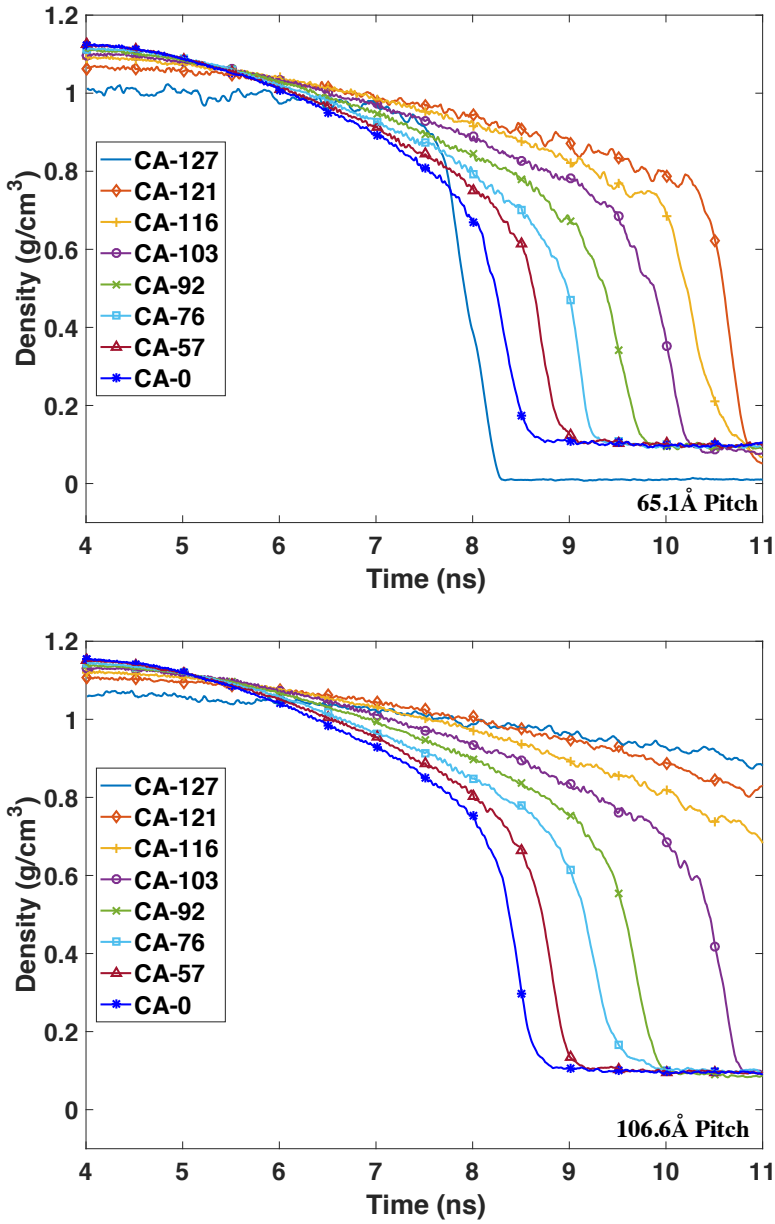

Figure 4.5: Phase II density profiles for a) 21.7Å pitch, b) 45.2Å pitch, c) 65.1Å pitch and d) 106.6Å pitch.

For the 21.7Å pitch case shown in Figure 4.6(a), within the liquid there is indeed a spike in the number of evaporated argon atoms coinciding with the maximum heat flux near 7 ns. The CA-0 case has the largest ratio, which suggests better heat transfer, however it

should be noted that there is not a direct (one-to-one) correlation between evaporation and maximum flux, and it will later be seen that the evaporation ratio peaks are more closely spaced than the heat flux peaks. In the 65.1Å pitch case of Figure 4.6(b) the peaks occur later in the simulation, and the evaporation ratio is increasing with decreasing contact angle. This trend continues in Figure 4.6(c) (106.6Å pitch case), and due to a lack of any anomalous Cassie-Baxter states each peak occurs at increasing times (and superheats) as the contact angle is increased. Of the contact angles and pitches considered, the 106.6Å pitch is the only case that exhibits no Cassie-Baxter transition.

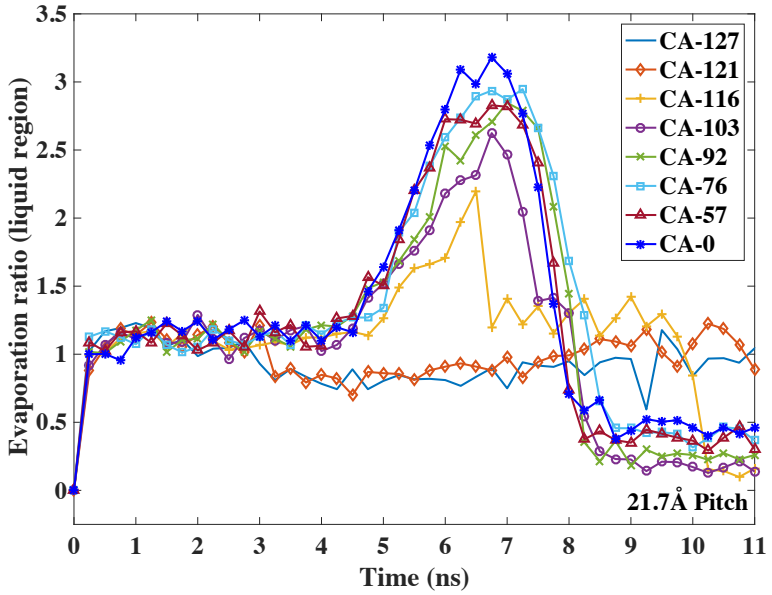

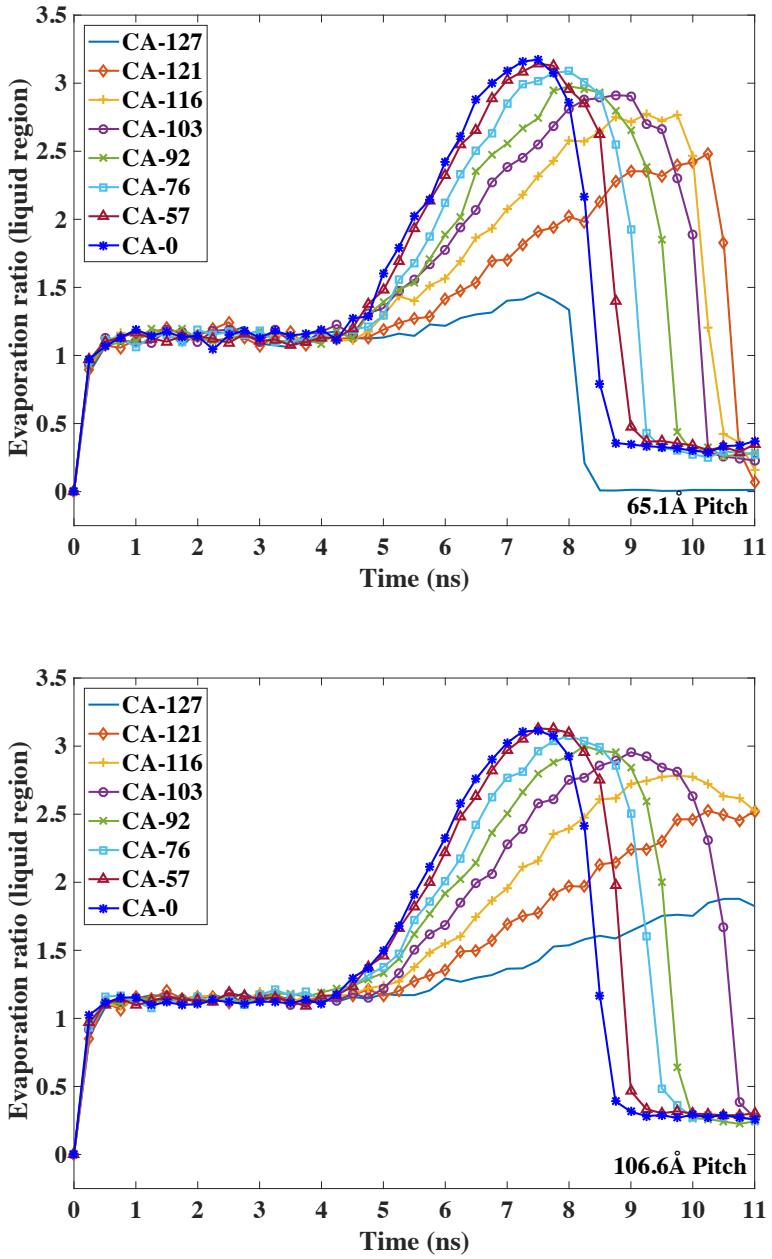

Figure 4.6: Evaporation ratio (in the liquid region, z<50 Å) a) 21.7Å pitch, b) 65.1Å pitch, and c) 106.6Å pitch.

The boiling curves for the 21.7Å, 65.1Å, and 106.6Å pitches are shown in Figures 4.7(a)-(c). To calculate heat flux the total energy (kinetic and potential) of the argon atoms was tracked each time step, then divided by the time step size and surface area of

the substrate to calculate the heat flux. The fluxes for all the present cases are in line with previous simulations,[64] as well as the heat flux limit predicted by the evaporative kinetic theory.[114] Interestingly, at smaller pitches the excess temperature at which the peak flux occurs tends to increase with decreasing contact angle, except for the two highest and two lowest contact angles. For the 21.7Å pitch scenario (Figure 4.7(a)) CA-0 shows the maximum heat flux (~1.02×10^8 W/m^2), which is a 91% increase over the minimum case of CA-127 (~0.09×10^8 W/m^2) and a 5.9% increase over CA-57 (~0.96×10^8 W/m^2). For most cases the temperature required to reach the maximum flux condition are grouped relatively closely near an excess temeperature of 113 K, though the CA-116, CA-121, and CA-127 cases are not due to the Cassie-Baxter transition. Indeed, here it is confirmed that CA-121 and CA-127 do not reach a heat flux maximum at all, as their fluxes are seen to slowly increase through the entirety of the simulation time.

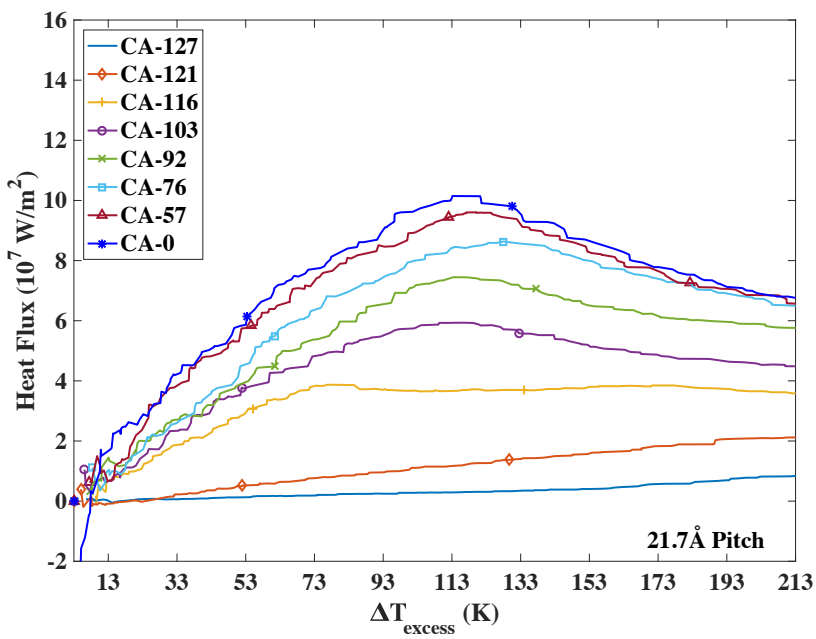

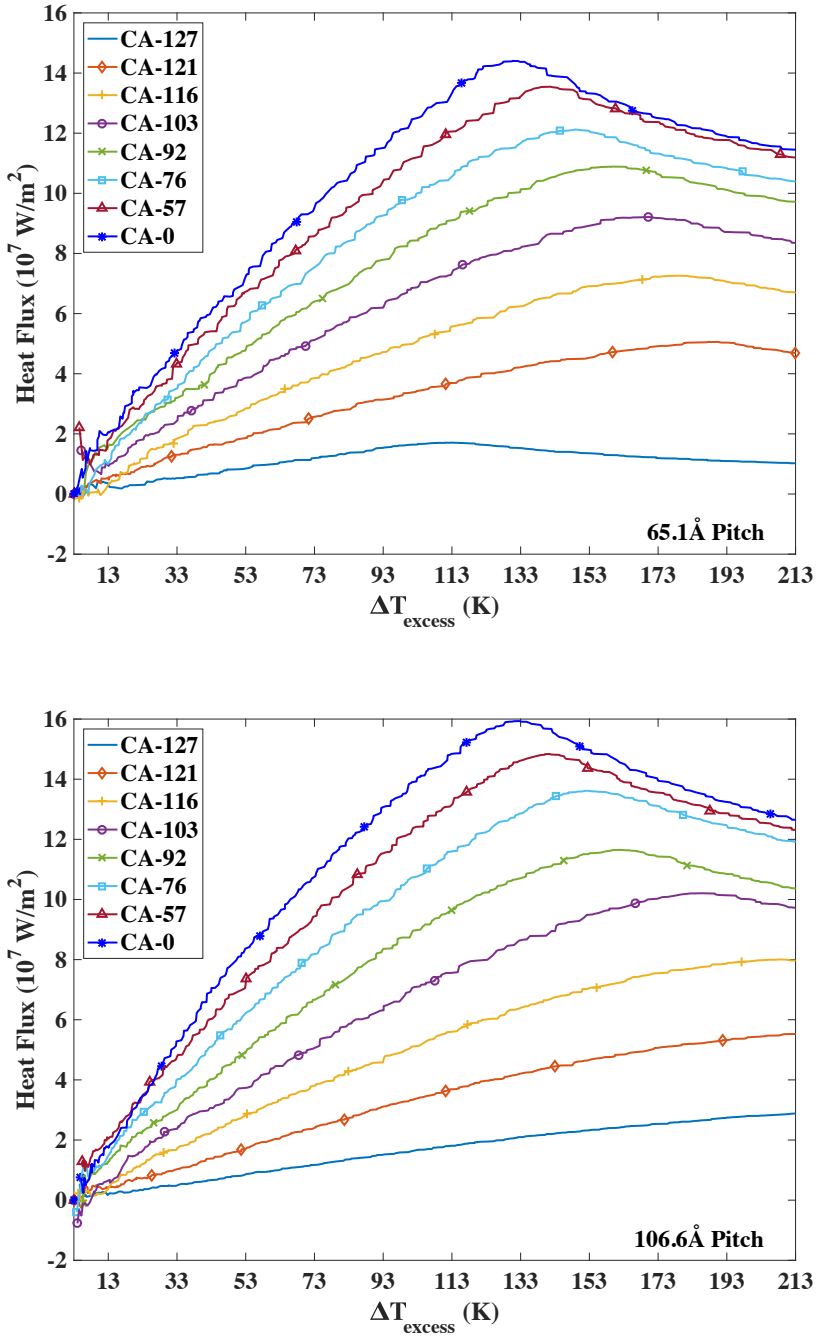

Figure 4.7: Boiling curves (argon heat flux vs. excess temperature) for a) 21.7Å pitch, b) 65.1Åpitch, and c) 106.6Å pitch.

In the 65.1Å pitch scenario (Figure 4.7(b)) CA-0 case shows a higher overall maximum flux (~1.44×10^8 W/m^2) than the lower pitch cases, and is an 88% increase over CA-127 (~0.17×10^8 W/m^2) and a 6% over CA-57 (~1.35×10^8 W/m^2). At this pitch the peaks are less concentrated, with CA-0's peak (at ΔT_{excess}= 133 K) ~9K lower than CA-57, and ~55 K lower than CA-121. Here all cases reach a maximum flux point, though CA-127 remains anomalous with a peak at ΔT_{excess}= 113 K, which is much earlier than the other cases.

The overall trend shows that as the pitch is increased the more hydrophilic cases tend to improve peak flux performance as compared to the more hydrophobic cases, and the maximum flux shifts toward greater superheats. This trend continues for the 106.6Å pitch case (Figure 4.7(c)), where CA-0 shows the highest flux (~1.59×10^8 W/m^2, at ΔT_{excess}= 132 K). This is ~82% higher than CA-127 (~0.29×10^8 W/m^2), and ~7 higher than CA-57 (~1.48×10^8 W/m^2). CA-127 once again does not reach a heat flux maximum, however in this case it is due to the superheat required exceeding 213 K rather than effects of Cassie-Baxter state. Overall, in terms of heat flux the larger pitch scenarios looks most like what would be expected from a macro-scale study, where increasing hydrophilicity corresponds to greater heat flux. The excess temperature at the onset of film boiling, however, is inversely related to hydrophilicity.

Figure 4.8(a) shows a plot of the peak flux as a function of contact angle. As can be seen, the most hydrophilic case shows the highest peak flux at all pitches, and there is a non-linear decrease in flux with increasing contact angle. This decrease is due to the weakening interaction between liquid and substrate, no longer allowing efficient kinetic

energy exchange. This trend is in line with previous experimental and theoretical studies[30,119,124] in which more hydrophilic substrates produced higher flux values. Also, the 85.0Å and 106.6Å pitches have extremely close flux profiles, thus it would be reasonable to assume that increasing the pitch further would do very little to increase the maximum heat flux.

Figure 4.8(b) shows the increase of peak heat flux with increasing pitch. Once again it can be seen that the peak flux increases with increasing pitch, non-linearly. The 106.6Å pitch case has a ~36% increase in peak flux over the 21.7Å case, a ~10% increase over the 65.1Å case, and only a ~1% increase over the 85.0Å case. This suggests that the peak flux eventually reaches a peak value somewhere slightly above a 106.6Å pitch. In previous larger-scale studies[50] smaller pitches corresponded with higher heat flux, which suggests that after the peak the flux values will start to decrease rather than plateau, however more simulations are needed to confirm this.

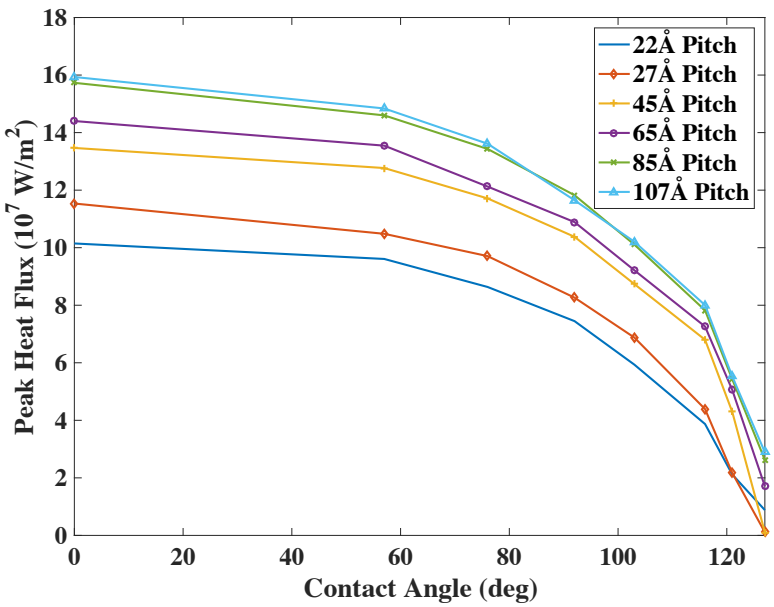

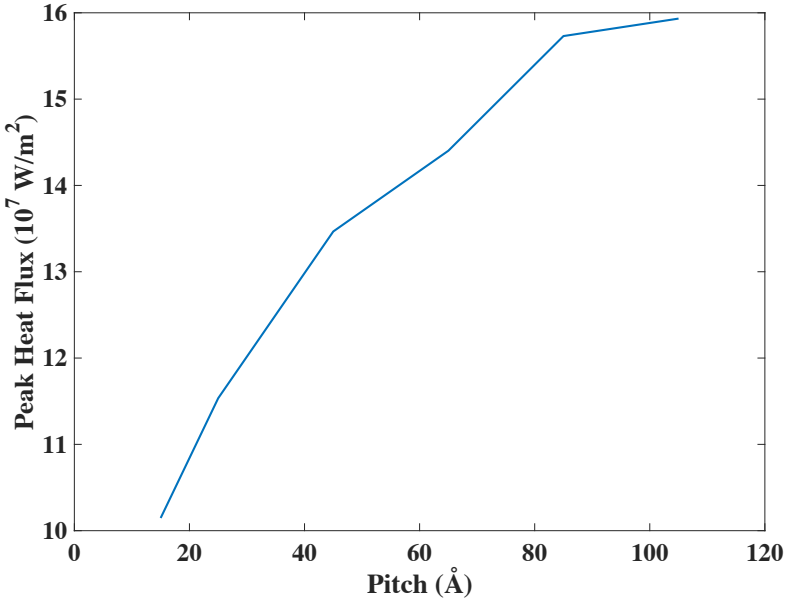

Figure 4.8: Peak heat flux curves: a) peak flux vs. contact angle and b) peak flux vs. pitch

Figure 4.9 shows the wall superheat at the peak flux condition vs. contact angle for each pitch scenario. Two distinct groups can be seen in this plot, with the three smallest pitches in one group and the three largest in the other. For the three largest pitches the superheat required to attain the peak flux increases with both increasing contact angle and pitch, which is expected. Increased wettability at low contact angles aids in kinetic energy transfer, leading to faster onset of the film boiling condition. At higher contact angles heating of the liquid occurs more slowly (per Figure 4.4) due to reduced liquid-solid particle interaction, leading to additional superheating before the film boiling condition is met. The lowest three pitches begin similarly to the previous group, with an increase (albeit slight) in superheat with increasing contact angle. This initial rise, however, is followed by an eventual drop in required superheat. The

combination of low pitch and hydrophobic interaction results in the Cassie-Baxter transition, which alters the dynamics of the system. These low superheats could be due to the pitch being of similar length to the critical bubble radius (in this case ~20Å). Instead of a bubble nucleating, growing, and then finally separating from the substrate (as in a high pitch case), a growth-hindered bubble would be less likely to separate, eventually coalescing with nearby bubbles to form a vapor layer near the substrate and leading to the film boiling condition. Regarding pitch, although the lower pitch scenarios (namely the 21.7Å and 27.1Å cases) have lower overall heat fluxes, they also reach peak heat flux at much lower wall superheats, which could be desirable in applications that need to remain at lower temperatures for mechanical or efficiency reasons.

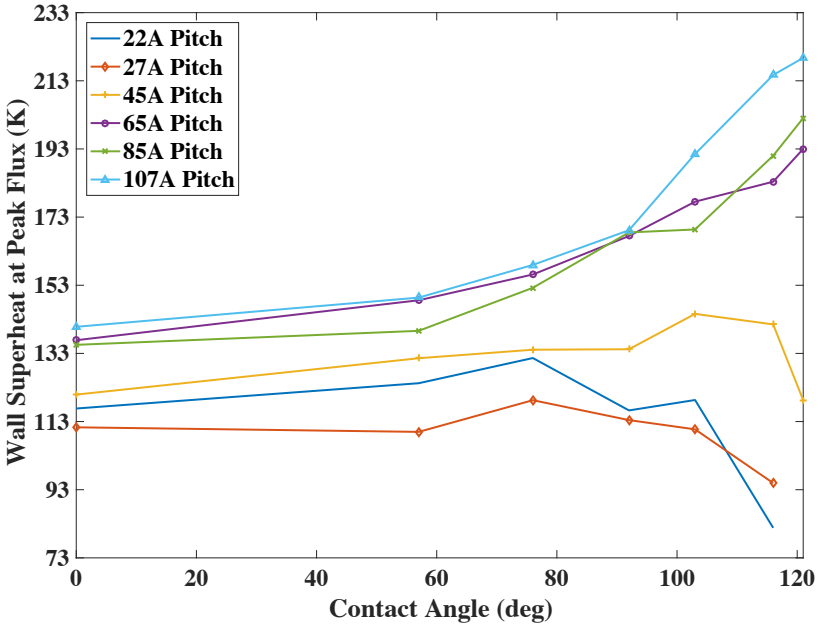

Figure 4.9: Wall superheat at peak flux vs. contact angle

4.4 Conclusions

Evaporation and film boiling of a thin liquid argon film on a nano-structured copper substrate was investigated via MD simulation. After obtaining boiling curves based on varying contact angles and pitches, and monitoring temperature, density, pressure, and evaporation the following observations were made:

- In line with previous studies, it was found that for a given pitch, there is an inverse relationship between contact angle and heat flux. As the pitch is increased the heat flux also increases.
- For the lowest pitch (21.7Å) the peak heat flux was ~1.01×10^8 W/m^2. The largest overall flux occurred at the 106.6Å pitch, with a maximum of 1.59×10^8 W/m^2. The heat flux increase of the maximum over the minimum case for a given pitch ranged from ~80-90%, while the 106.6Å pitch case showed a 1-36% increase in peak flux over the lower pitch cases.
- For pitches 65.1Å and above, the temperature at which peak heat flux occurs (and thus the degree of superheat) increases with increasing contact angle, and was also found to increase with pitch. Lower than 65.1Å the combination of large contact angles and small pitches results in the liquid film eventually transitioning to a Cassie-Baxter state, which reduces overall heat transfer.
- This density and evaporation number data corroborates these findings, showing peaks that correspond to the onset of the film boiling condition for each case.

Chapter 5

Pool Boiling Heat Transfer on Single-Layer Graphene Coated Substrates

5.1 Introduction

Pool boiling specifically is attractive due to its passive nature, resulting in reduced system complexity and ease of implementation. Another method of improving heat transfer that has garnered much attention in the recent past is the use of graphene. Graphene has a host of favorable properties,[125] including very high thermal conductance[126,127] as well as effective thermal rectification.[128] The effect of geometry and temperature of metal-graphene composites has been investigated via MD simulation,[129] showing that interface conductance tends to decrease as the number of graphene layers is increased. The thermal resistance at a water-graphene interface was also simulated,[130] showing that the Kapitza resistance decreased with increasing number of graphene layers, and was also dependent on the density stratification of the adjacent water block.

Trying to take advantage of graphene's properties for pool boiling purposes is a natural next step. Recently, some macroscale pool boiling experiments have shown an increase in heat transfer when using graphene-coated substrates. Seo et al.[131] showed a 9% increase in critical heat flux (CHF) for a nonporous graphene-coated ITO (indium tin oxide) surface over bare ITO, while porous graphene-coated ITO increased CHF by 90%. Similarly, Jaikumar et al.[132] showed that both CHF and heat transfer coefficient of over 40% when comparing water boiling on a copper versus graphene and graphene oxide coated copper. While these pool boiling experiments involving graphene-coated substrates have been carried out, very few, if any, experiments or simulations have

explored this scenario on the nanoscale. In this study, metallic substrates like copper, nickel, and platinum, and semiconductor silicon are topped with single-layer graphene (SLG), and system temperatures are raised to induce nucleate boiling of water. Such substrates have favorable thermal properties and have been used to grow graphene in the past.[129,133] These materials are often used in electronic chips and other high power devices due to their thermal properties (among others), and enhancing these properties is often a method used to improve system performance. For the metal substrates there is also the possibility of growing large area graphene films via chemical vapor deposition (CVD).[134] Simulation of these different scenarios allows for comparison of many system attributes, including liquid density, heat flux, substrate thermal conductivity, and vibrational density of states (VDOS), to gain insight into the heat transfer mechanisms of these small-scale systems.

5.2 Simulation Method

The simulation domain shown in Figure 5.1 consists of a metal substrate topped with a single layer of graphene, over which the liquid water rests. Water vapor fills the rest of the simulation domain. The domain is roughly 49 x 46 x 210 $Å^3$, although slight changes to each dimension were made in certain cases to accommodate the varying substrate lattice parameters. To prevent finite size effects the domain is periodic in both the positive and negative *x* and *y* directions, while the upper *z* boundary is a fixed, reflective, adiabatic boundary. Each substrate consisted of five monolayers, where the bottom monolayer was held immobile to act as a lower *z* direction boundary, and the second layer was used for thermostatting purposes. Based on previous works,[66,121] the upper

three layers were deemed to be enough for use as conduction layers to heat the water above. The Cu, Ni, and Pt were arranged in an FCC lattice structure, with densities of 8.96 g/cm^3, 8.91 g/cm^3, and 21.46 g/cm^3, respectively. The Si substrate was arranged in a diamond cubic structure with a density of 2.33 g/cm^3.

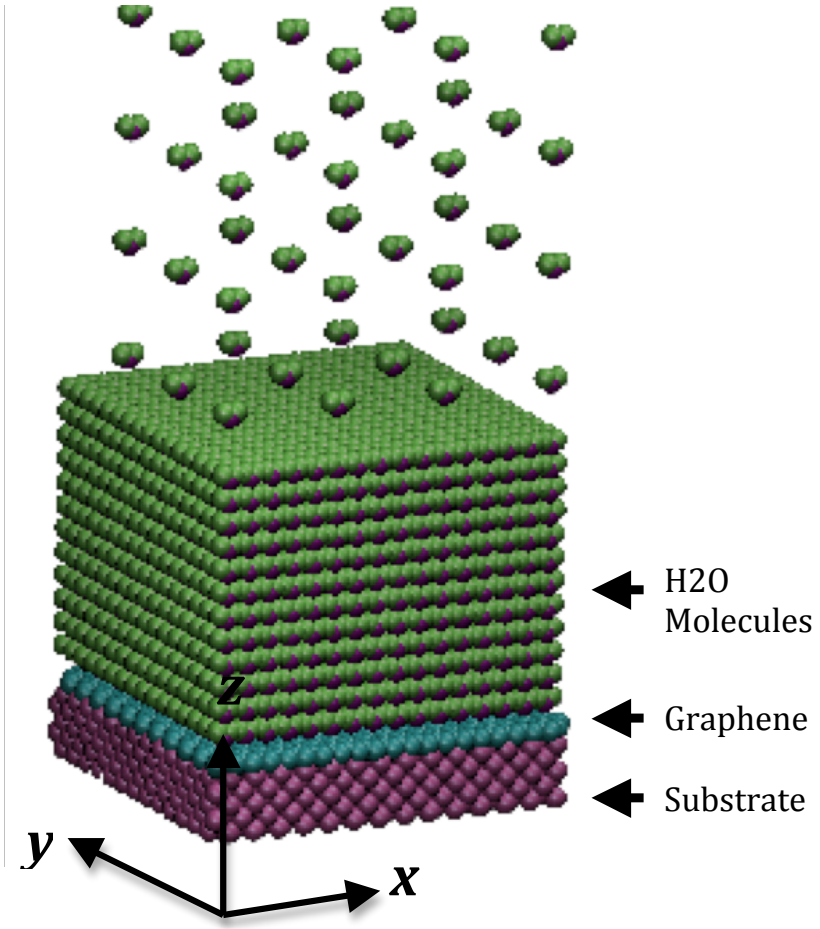

Figure 5.1: Setup of simulation domain.

For each substrate, boiling simulations were run using the 100, 110, and 111 planes in order to test conductivity and compatibility with the graphene layer. Each plane has a different lattice mismatch with graphene as well as a slightly different substrate-graphene separation distance, which could affect overall heat transfer. The number of

substrate atoms ranged from 720 to 2185 atoms. Table 5.1 shows the simulation domain dimensions and number of substrate atoms for each case. In this study cases are referred to by the substrate material, lattice plane, and graphene layer (e.g. CuG100); in the cases without graphene used for comparison purpose, only substrate and plane are marked (i.e. Cu100). 880 graphene atoms were arranged above the main substrate with the standard hexagonal (honeycomb) lattice, with a 2.46 Å lattice constant.

Table 5.1: System dimensions and substrate configurations.

Case	**Dimensions (Å)**	**# Substrate Atoms**
CuG100	50.6 x 47.0 x 211.0	1820
CuG110	51.3 x 46.8 x 208.2	1359
CuG111	50.6 x 46.8 x 210.5	2128
NiG100	49.3 x 46.8 x 210.5	1890
NiG110	49.3 x 47.4 x 207.9	1330
NiG111	49.6 x 46.8 x 211.9	2185
PtG100	50.0 x 47.1 x 211.5	1560
PtG110	51.0 x 46.8 x 208.6	1105
PtG111	49.2 x 48.6 x 213.3	1854
SiG100	49.2 x 46.8 x 208.2	720
SiG110	49.2 x 46.8 x 211.3	1080
SiG111	49.2 x 46.8 x 209.5	1040

Twelve monolayers of liquid water (forming a 36 Å thick film) were initially placed above the graphene layer with water vapor molecules filling the rest of the domain, totaling 3,192 molecules. The extended simple point charge (SPC/E) water model[135] was employed, which uses a 1 Å bond length, 109.47^{o} HOH bond angle, -0.8476*e* oxygen charge and 0.4238*e* hydrogen charge. The SHAKE algorithm[90] was used to maintain the molecule geometry, while a PPPM solver[136] with 10^{-4} accuracy was used to compute long-range Coulombic interactions.

The interactions between graphene and hydrogen molecules were modeled using the AIREBO potential[77] with a 10.2 Å cutoff. Interactions between Si atoms were

modeled using the three-body Stillinger-Weber potential[76] with a cutoff of 3.8 Å, which works well for atoms arranged in the diamond cubic lattice structure (Si, Ge, etc.). The remaining interactions were modeled using the standard 12-6 Lennard-Jones (LJ) potential with an additional term to take Coulombic interactions into account (Equation 2.9). All LJ potential parameters are shown in Table 5.2.[137-142] It should be noted that for use with the PPPM solver the Coulomb term includes a damping factor, which goes to zero at r_C, and takes an *erfc* form.[143] It should also be noted that different cutoff radii (r_C) are used for the LJ and Coulombic terms. The LJ term cutoff is 11.66, while the Coulombic term cutoff is 12.66 ($4\sigma_{oxy}$). For atoms of different LJ molecules the common Lorentz-Berthelot mixing rules (Equation 2.8) were applied. In keeping with the SPC/E model, the hydrogen molecules do not have any LJ interactions.

Table 5.2: Lennard Jones potential parameters.

LJ Interaction	**σ (Å)**	**ε (eV)**	**r_C (Å)**
Cu-Cu	2.3300[a]	0.40960[a]	12.664
Cu-C	3.0825[b]	0.02578[b]	12.664
Cu-O	2.7480[c]	0.05254[c]	12.664
Cu-H	0.0000	0.0000	0.0000
Ni-Ni	2.2800[d]	0.51970[d]	12.664
Ni-C	2.8400[e]	0.60000[e]	12.664
Ni-O	2.7230[c]	0.05918[c]	12.664
Ni-H	0.0000	0.0000	0.0000
Pt-Pt	2.4750[f]	0.52115[f]	12.664
Pt-C	2.9500[g]	0.02206[g]	12.664
Pt-O	2.8205[c]	0.05927[c]	12.664
Pt-H	0.0000	0.00000	0.0000
O-O	3.1660[h]	0.00674[h]	12.664
O-C	3.1900[i]	0.00455[i]	12.664
O-H	0.0000	0.0000	0.0000

a. Reference 125
b. Reference 138
c. Equation 2.8
d. Reference 139
e. Reference 140
f. Reference 126
f. Reference 126
g. Reference 141
h. Reference 137
i. Reference 138

From the initial setup, the simulations were carried out in two phases. Initialization and equilibration took place during Phase I, where an energy minimization was implemented on the initial atom arrangement, after which a 400 ps equilibration occurred. The equilibration occurred in the canonical ensemble (NVT) with a Nosé-Hoover thermostat at 300K on all atoms. The temperature, vapor pressure, and energy were monitored to ensure equilibrium prior to the beginning of Phase II.

At the start of Phase II, the thermostat is removed from all atoms except those in the 2nd monolayer of the substrate. The temperature of these atoms was increased (instantaneously) to 400K to induce nucleate boiling, while all other atoms were held in the microcanonical (NVE) ensemble. Over the course of 3000 ps the high temperature thermostat atoms were allowed to interact with the upper layers of the substrate, graphene, and water, thereby increasing the overall temperature of the system. Both phases used a velocity-Verlet integration scheme with a 1 fs timestep.

Thermal conductivity was calculated using the Green-Kubo method. First, the heat flux was calculated using Equation 3.1. The thermal conductivity *k* can then be determined via the ensemble-average of the autocorrelation of the heat flux:

$$k = \frac{V}{3k_B T^2} \int_0^\infty \left\langle q''(0) \bullet q''(t) \right\rangle dt \tag{5.1}$$

As these simulations utilize classical MD, it should be noted that all conductivities only include the portion due to phonon transport.

In order to gain further insight into the relationship between the substrate, graphene sheet, and liquid water, we calculated the vibrational density of states (VDOS) for these system components. The VDOS is proportional to the Fourier transform of the

normalized velocity autocorrelation function (VACF) and can thus be calculated using the following relation:

$$D = \int_{-\infty}^{\infty} \frac{\sum_{i=1}^{N} \left\langle v_i(t) \cdot v_i(0) \right\rangle}{\sum_{i=1}^{N} \left\langle v_i(0) \cdot v_i(0) \right\rangle} \tag{5.2}$$

where $\langle \mathbf{v}_i(t) \bullet \mathbf{v}_i(0) \rangle / \langle \mathbf{v}_i(0) \bullet \mathbf{v}_i(0) \rangle$ is the normalized VACF.

In order to better compare the VDOS data we calculated a quantity S, the overlap of the vibration spectra:[144]

$$S = \frac{\int_0^{\infty} D_1(f) D_2(f) df}{\int_0^{\infty} D_1(f) df \int_0^{\infty} D_2(f) df} \tag{5.3}$$

where D_1 and D_2 are two different VDOS profiles. Two overlaps were calculated for each case, between the substrate and water (S_{SW}), and graphene and water (S_{GW}).

All simulations were conducted using LAMMPS software (version 31 Mar 2017), an open-source classical MD code based on Plimpton's work,[111] while visualization was performed with VMD v1.9.1.[112] The simulations were performed on a cluster of 2.6 GHz Intel Sandy Bridge 2670 CPUs, typically using ~22 MB of memory per processor.

5.3 Results and Discussion

In general, the metal-graphene substrates all increase in temperature very quickly after the onset of Phase II, reaching the target temperature within 30 ps. The SiG substrate requires a bit more time, taking more than 650 ps to reach 400 K. There is very little separation between the water temperatures of different plane cases for all but the SiG

substrate, in which the 111-plane reaches the target temperature within 600 ps of heating, while the other planes require 1,100 ps. It should be noted that the temperature overshoot in the SiG cases was ~7-12%, compared to only ~5% for the metal-graphene cases.

Figure 5.2 shows the through-plane thermal conductivity for each substrate as heat is provided in the *z*-direction, along with reference values for validation purposes. The bottom bar graph shows the conductivity for different planes of the each pure substrate, while the top shows the overall SLG-coated substrate conductivity for the 100-plane as well as typical graphene-only conductivities. Starting at the bottom of the figure, Cu has shown 2-10% phonon contribution to the total thermal conductivity (400 W/mK) in previous works,[145,146] which aligns well with the present results shown (~2.5-9.5% phonon contribution). Momenzadeh et. al.[145] calculated Cu conductivity via MD/Green-Kubo method at zero pressure (and using an EAM potential), while Yao et. al.[146] experimentally determined low temperature (<60 K) phonon conductivity in single crystal Cu by suppressing electronic thermal conduction via magnetic field. Ni (bulk k~90 W/mK) shows 8-30% phonon contribution, which is somewhat higher than previous work by Ou et al.,[147] which found ~3% phonon contribution at 300K by using Ni nanowire and estimating phonon conductivity from resistivity measurements and the Wiedemann-Franz law. However, boundary scattering effects in the nanowire could explain their lower conductivity values. There is a good agreement however with Heino et. al.,[148] who used MD to apply a constant heat flux (in the 100 direction), measuring the temperature gradient, then directly calculating the conductivity. Pt (bulk k~71 W/mK) shows 3-28% phonon contribution, which is also in good agreement with Heino et. al.[148] (~15% phonon contribution). Si (bulk k~145 W/mK), which has a very large phonon

contribution, has a thermal conductivity ranging from ~6-11 W/mK, lower than that found by Esfarjani et al.,[149] which used the MD/Green-Kubo method at 600 K and resulted in conductivities of 27-47 W/mK.

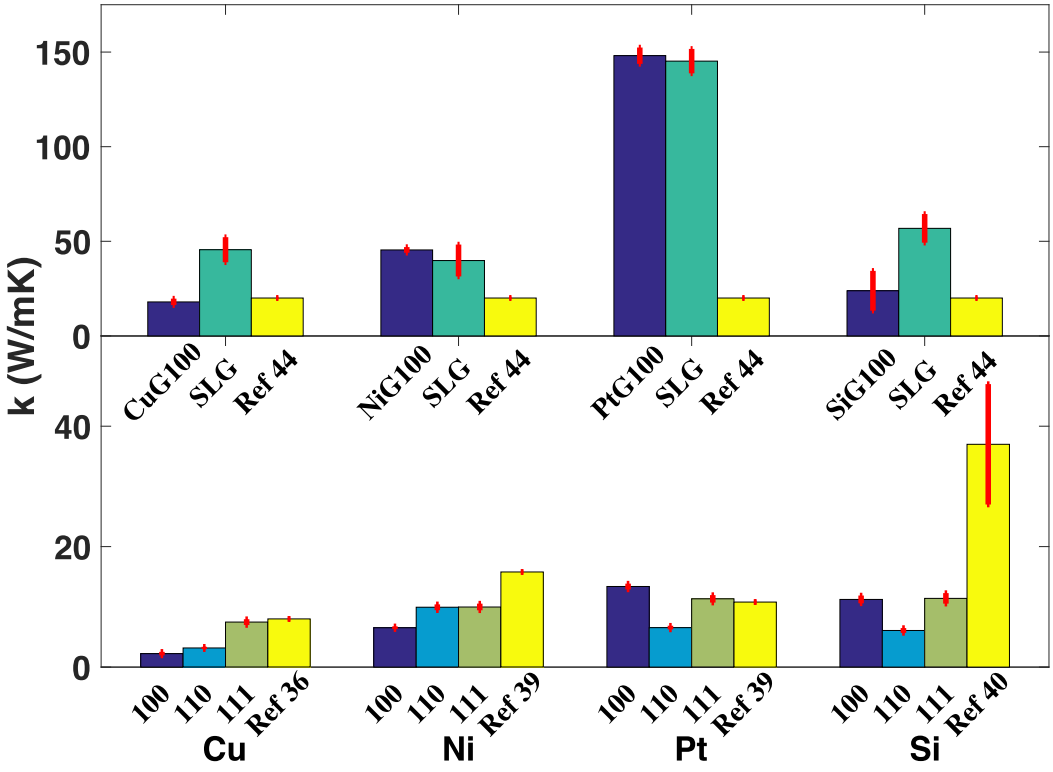

Figure 5.2: Thermal conductivity values for the different substrate planes (bottom) as well as graphene only and SLG-coated substrates (top), with error bars shown in red.

The single-layer graphene sheet, as expected, has a through-plane thermal conductivity greater (by 1-2 orders of magnitude) than that of the metallic and semiconductor substrates studied. Typical values of the 100-plane (labeled "SLG") are shown in the top of Figure 5.2. The graphene-only *k* values ranged from 13-200 W/mK, which is much lower than found in previous studies,[126,150] though these measured the in-plane conductivity of free (suspended) SLG. Also, supported

graphene has lower thermal conductivity in part due to damping of out-of-plane phonon modes.[151,152] The *k* values presented here represent the through-plane conductivity, and as graphene is an anisotropic 2D material this tends to be much lower than its in-plane conductivity.[126,152] Indeed, in our study the in-plane conductivity (not shown) was found to be anywhere from 1-3 orders of magnitude greater than the through-plane conductivity. For comparison results from Alofi and Srivastava[153] (of through-plane graphite conductivity) are presented with our data. We expect this to be of the same order of magnitude as graphene through-plane conductivity. The SLG-substrate conductivity for the 100-planes is shown in dark blue. In all cases they are higher than that of the bare substrate, and in the 100- and 110-plane cases they are either within the margin of error or below the values of the SLG conductivity. Curiously, the conductivity values for the 111-plane SLG-substrates (not shown) are all greater than the SLG only values. Further exploration is required to determine the exact cause, however it is possible that the combination of Si's diamond lattice and 111-plane results in better coupling between materials, resulting in a reduction of cross-plane phonon scattering. There was no obvious trend regarding specific lattice planes (100, 110, etc.) having higher or lower conductivities, but it is clear that the addition of graphene greatly improves overall *k* values. The PtG100 case showed the largest overall combined conductivity, averaging just above 148 W/mK. Figure 5.3 shows some typical thermal conductivity profiles for SLG-coated substrates during Phase II. Generally there is a brief period (0.5-1.5 ns) of transience after the temperature is increased at the beginning of the phase, after which conductivity values become relatively stable.

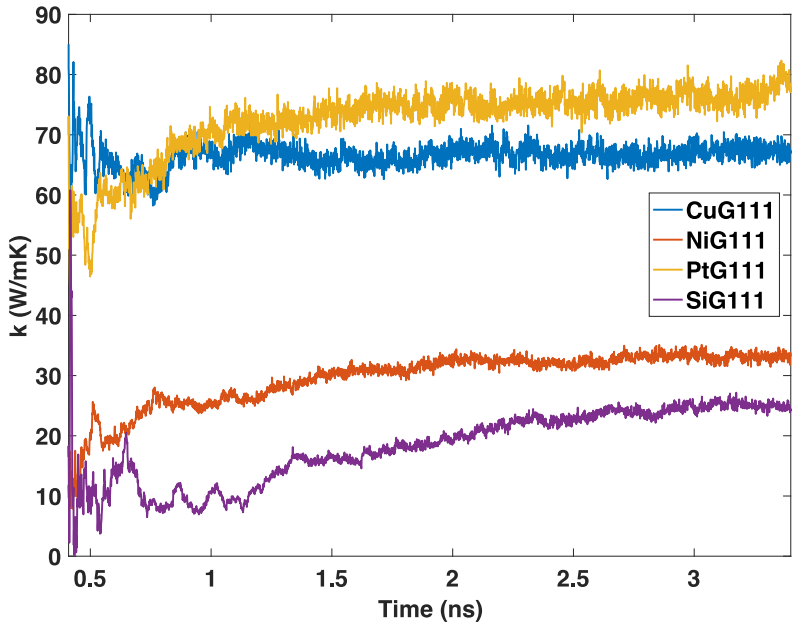

Figure 5.3: Phase II thermal conductivity profile for select SLG-coated substrates.

Figure 5.4 shows Phase II heat flux profiles for the SLG substrates (110 plane) in order to highlight the overall trends. As mentioned, there is a heat flux peak reached very soon (within 0.2 ns) after the onset of Phase II, followed by an exponential decay as the temperature equalizes. At around 3 ns the flux values tend to reach stable levels with respect to time, as well as in relation to one another. Figure 5.5 details the heat flux profiles for each case. Results from additional graphene-less simulations (water was heated directly on the 100 plane of the metal and Si substrates) were also included for comparison. For the SLG-coated substrates the initial profile had distinct maxima in the first 50-200 ps, with ~1-2 GW/m^2 difference between peaks (shown in the bottom of the figure). The 110, 110, 111, and 111 planes resulted in the highest peaks, respectively. Of the graphene-containing cases, CuG110 resulted in a maximum overall peak of 4.50 GW/m^2, while SiG110 had the lowest peak of 1.58 GW/m^2. However perhaps the most surprising the result is that for all materials the graphene-less substrates had much higher

initial peaks than the others, ranging from ~4-14 GW/m^2. The interfacial thermal (Kapitza) resistance between the graphene and substrate layers could play a role in this effect, reducing heat transfer between solid layers as well as graphene-water layers.[130] The single-layer nature of the graphene would also play a role, as the thermal conductance of graphene tends to increase with the number of layers.[129] This overall trend goes against previous experimental works,[131,132] which showed an increase in heat flux with the addition of a graphene coating. However, it should be noted that in those experiments, the resulting graphene surfaces have increased surface roughness compared with the plain substrates, as well as multiple graphene layers, both of which could act to increase heat flux over the bare substrate cases. These millimeter-scale experiments showed overall heat fluxes on the order of 1 MW/m^2, 3-4 orders of magnitude lower than found in our nanoscale simulations.

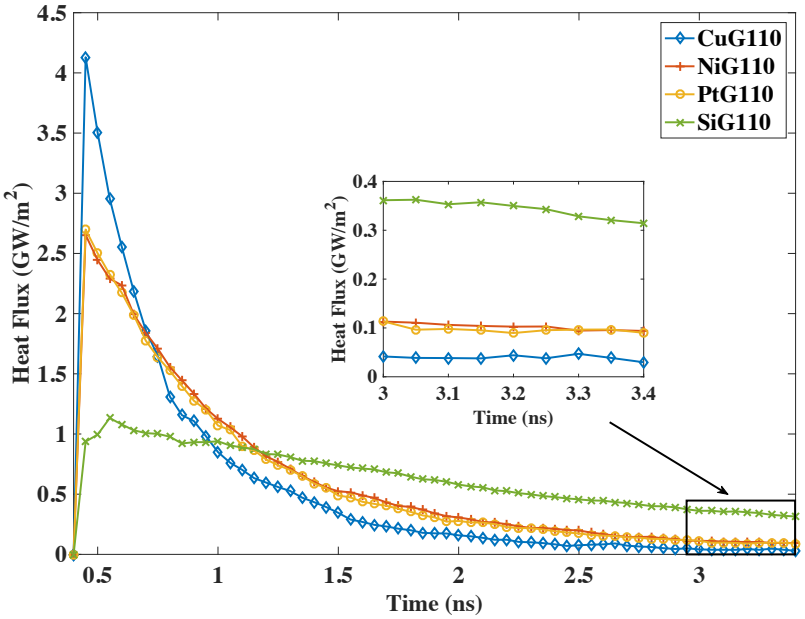

Figure 5.4: Heat flux profile for SLG-coated substrates. Inset shows values at the end of the simulation.

In general however, the initial peak would only be of interest in applications with extremely short durations, as the peak effects subside within 1.5-2.5 ns of the temperature increase. After this point the heat fluxes reach relative levels that remain the same for the remainder of the simulation. For example, for the PtG substrate, after ~2.5 ns the 100 plane exhibits the highest flux, followed by the 110 and 111 planes, and this remains the case until the end of the simulation. Thus for longer heat transfer processes the stable flux values (top of figure) would be of greater interest. In all cases, after the initial peak the heat flux decreased exponentially toward a steady state value with less separation between cases. By the end of Phase II separation between maximum and minimum cases typically ranged between ~0.02-0.20 GW/m^2. It should be noted that among graphene-containing cases the maximum initial peak did not predict the maximum average values at the end of the simulation, in fact the opposite appears to be true. The cases exhibiting the highest initial peaks tended to have the lowest average heat flux values. Also, the (graphene-less) Cu, Ni, Pt, and Si100 cases moved from having the highest initial peaks to either the lowest or next-to-lowest fluxes averaged over the entirety of Phase II. The CuG100 and CuG111 stable fluxes were 1.7x greater than that of Cu100, while NiG111 was 9.6x greater than Ni100. PtG100 shows a 4.7x increase over Pt100, while SiG110 is 2.3x greater than Si100. Of the SLG-substrate cases, SiG110 resulted in the highest average heat flux value (~0.31 GW/m^2), while CuG110 had the lowest (~0.03 GW/m^2). This general trend does follow the experimental data. Due to graphene's superior conductivity the initial Kapitza resistance is overcome and allows SLG-coated substrates to have better heat flux performance than graphene-less substrates once a steady heat flux is achieved.

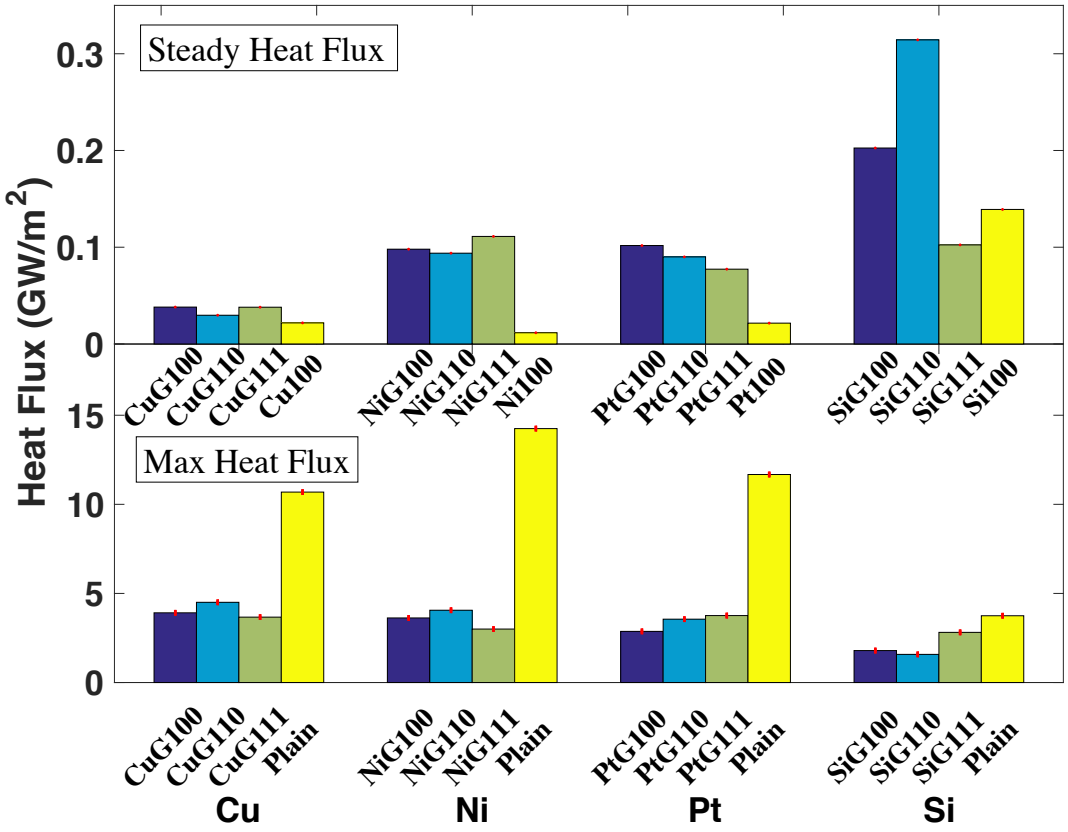

Figure 5.5: Heat flux values for different substrate cases, with error bars shown in red.

Based on Fourier's Law of heat conduction, Figure 5.6 details the time-averaged temperature gradient *dT/dz* for two SLG-substrate cases (CuG100 and PtG100) and the corresponding graphene-less cases (Cu100 and Pt100) from the known conductivity and heat flux profiles. As can be seen, the *dT/dz* values for the SLG-substrates are lower than that of the graphene-less case, especially in the first half of Phase II. Although it's through-plane conductivity is poor, graphene's high in-plane thermal conductivity allows for more uniform heating. In practical terms, this much less steep temperature gradient results in a reduction of hotspots, thereby preventing overheating of the substrate. Later in the simulation, once the water temperature has had a chance to increase via

conduction, the gradient of the graphene-less case is much closer to that of the SLG-substrate, though still larger in the case of Pt. Although not shown, the *dT/dx* and *dT/dy* gradients show the same trend, but with even larger differences in the first half of the simulation due to graphene's larger in-plane conductivity.

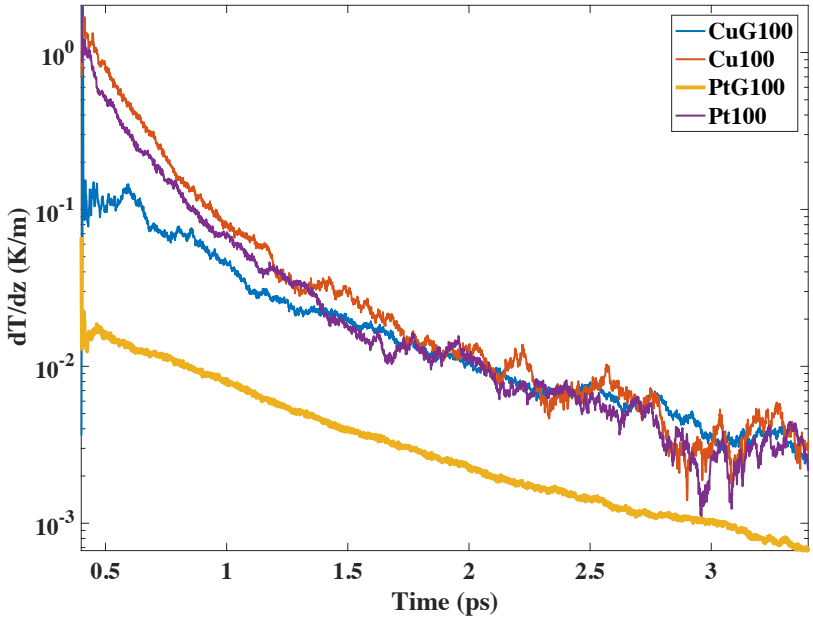

Figure 5.6: Time-averaged Phase II temperature gradient (*dT/dz*) data for select cases (log-scale).

The nanoscale boiling curves for select substrates were also determined, and plotted in Figures 5.7(a) and (b) to give a sense of the boiling process and CHF trends. To obtain the curves separate simulations were run, where after the Phase I equilibration process the temperature was incrementally raised from 373 K to 473 K over 3.5 ns. The temperature of the substrate was raised to various temperatures between 373 and 433 K and kept steady at each for 500 ps before moving to the next temperature. An interpolated curve was included for each data set to guide the eye. As could be predicted from the steady heat flux values of Figure 5.5, the SLG cases generally show higher heat fluxes

than the graphene-less cases. The CHF for the Cu100 is ~0.31 GW/m^2, while the CuG100 CHF is ~0.36 GW/m^2, an increase of ~14%. Also, the CHF is seen to occur earlier in the SLG case, at 20 K superheat compared to the 25 K superheat required for the graphene-less case. The PtG100 case (~0.48 GW/m^2) shows a ~9% increase in CHF over that of Pt100 (~0.43 GW/m^2). In this case, where both substrates have similar CHF values, the same superheat is required. Taking both the Cu and Pt cases together and because the heating surface is almost perfectly flat (so nanoscale roughness does not come into play), this suggests that larger CHF values will occur at lower superheat due to better heat transfer, which can vaporize the liquid and bring about film boiling more quickly. In general, the conductivity enhancement due to the SLG coating allows better overall heat transfer, which follows the trends in Figure 5.5 and previous experiments.[131,132] After CHF is reached, the flux drops briefly before continuing to rise again during film boiling.

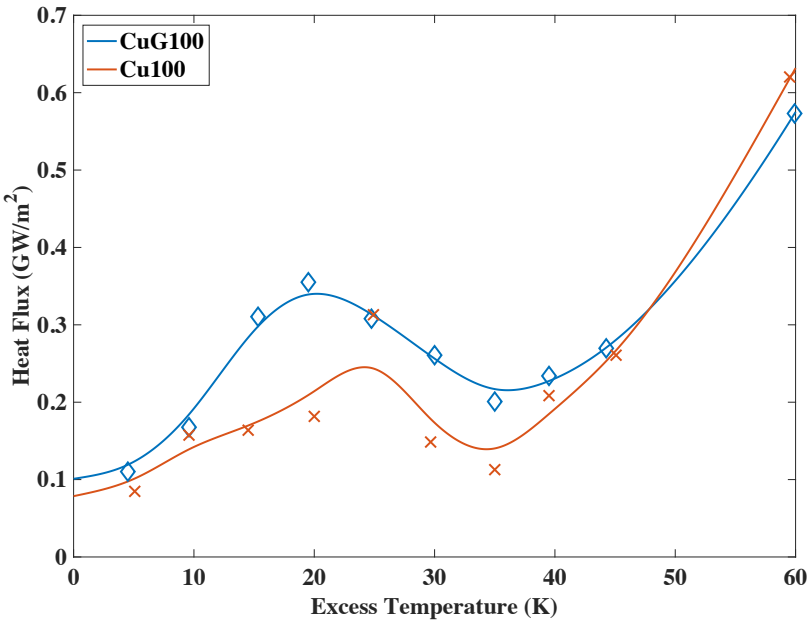

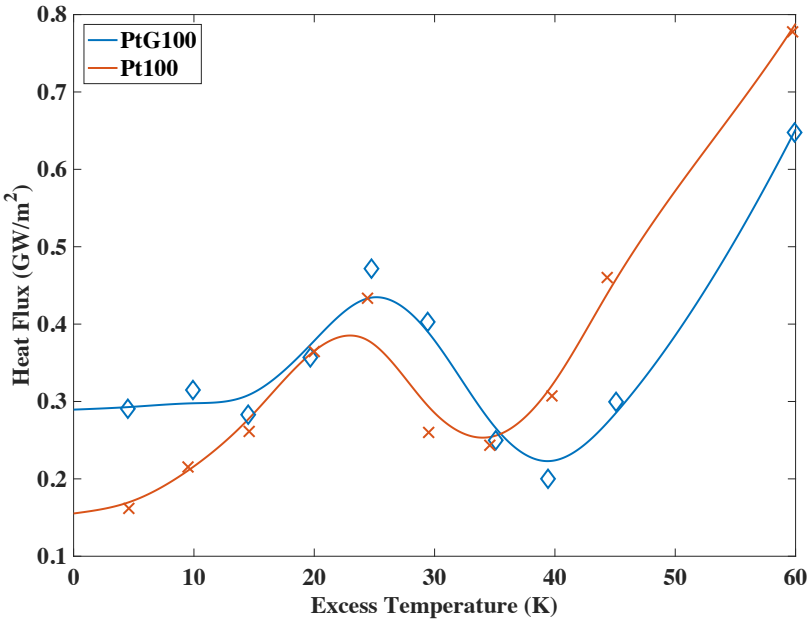

Figure 5.7: Boiling curves comparing a) CuG100 and Cu100 and b) PtG100 and Pt100.

All S values, which measure the degree of VDOS overlap, are detailed in Table 5.3. Perhaps unsurprisingly, in all cases S_{SW} had the highest overlap value. Again, due to the hydrophobicity of graphene the metal/silicon substrates tend to interact more strongly with the liquid, which improves vibration spectra overlap. Although graphene can improve conductivity, it still has a weak correlation with water, which may hinder overall heat transfer somewhat.

Table 5.3: VDOS overlap and overlap ratio values.

Case	S_{SW}	S_{GW}	S_{GW}/S_{SW}
CuG100	0.5015	0.1559	0.3109
CuG110	0.5808	0.2058	0.3544
CuG111	0.6486	0.2089	0.3221
NiG100	0.6224	0.2206	0.3545
NiG110	0.5441	0.2273	0.4178
NiG111	0.6202	0.2379	0.3837
PtG100	0.6082	0.2063	0.3392
PtG110	0.5675	0.2070	0.3648
PtG111	0.6302	0.2144	0.3401
SiG100	0.4467	0.2183	0.4887
SiG110	0.5265	0.2184	0.4149
SiG111	0.5415	0.1850	0.3417

In order to determine whether the VDOS overlap correlated with better heat transfer, the heat flux values were plotted against the ratios of the overlap values, shown in Figure 5.8. In particular the ratio S_{GW}/S_{SW} were chosen (the raw S values were also plotted against the heat flux, but no significant correlation was found), as these ratios can perhaps give a good view of the mismatch between substrates. The ratios for all cases range between ~0.3-0.5, suggesting a certain amount of mismatch, and thus Kapitza resistance, is always present. The only type of adsorption present in the simulations is physisorption, it is assumed that the stronger and more stable chemisorption bonding would result in smaller Kapitza resistance,[153] higher overlap ratios, and higher heat flux. The figure shows the steady flux values at the end of our simulation (with a trendline to guide the eye) and shows a positive correlation. This positive correlation makes intuitive sense, since an increase in the overlap ratio (while <1) implies less thermal resistance (between graphene and water) and more efficient heat transfer. At higher liquid temperatures, higher frequency graphene modes (which also have a somewhat higher

VDOS) are better coupled to the water and play a larger role in heat transfer, as opposed to the lower frequency modes which dominate when its spectral temperature is closer to that of the adjacent liquid or solid.[154,155]

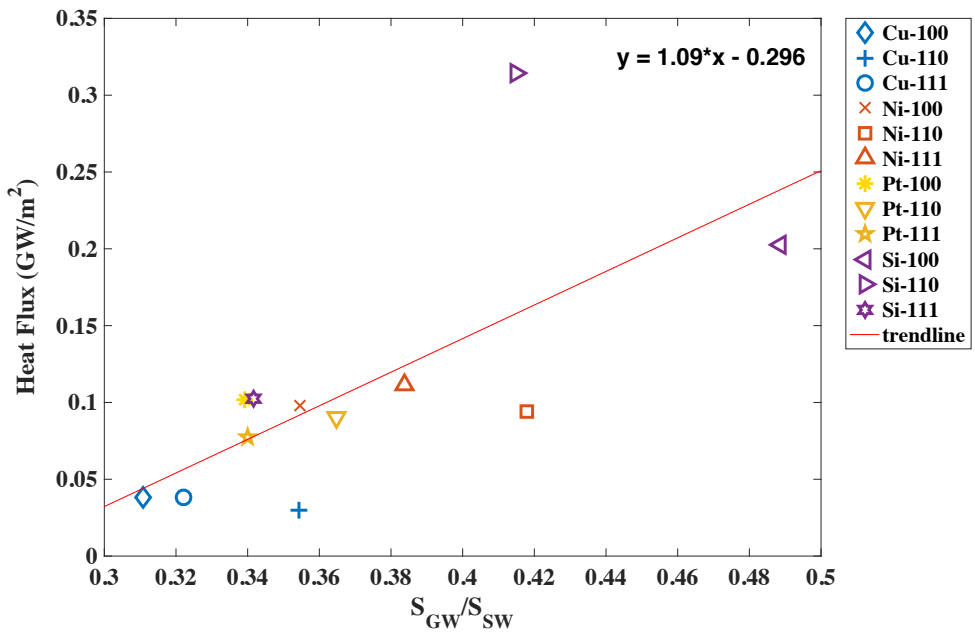

Figure 5.8: Steady heat flux vs overlap ratio S_{GW}/S_{SW}.

Figure 5.9 details the liquid water density profile of each case during Phase II. In order to calculate the density, the simulation domain was sliced into 1 Å high slabs, running the entire *x* and *y* directions. The density of each slab was then averaged every 5000 time steps for the duration of the simulation. The density values presented were averaged over the entire duration of the phase. Only the first 20 Å are shown in order to better view the density stratification near the solid wall. It should be noted that the oscillatory behavior of the density near the graphene sheet is due to the expected stratification due to wall interaction,[130] and can be attributed to the orientation of the water molecules closest to the graphene wall, which is determined by the water dipole.[156-

[158] Figures 5.9(a) and (b) show the results for Cu and Ni, and Pt and Si substrates respectively. The differences in near-graphene liquid density between the cases can be attributed to the substrate/graphene interaction potentials, substrate lattice constants and planar densities. In the case of Cu, the CuG111 shows the highest density peak, while NiG110, PtG110, and SiG111 show the highest density peaks for their respective substrates, though the Si peaks are closely clustered. The highest overall peak belongs to the NiG110 case, with a value of ~2.18 g/cm^3. The second peaks are also closely clustered and do not appear to show significant differentiation, but rather signify the intermediate density region before the bulk density is reached, which in all cases occurs at roughly 10 Å, with a density between 0.90 and 0.91 g/cm^3. For all substrates the density values drop to nearly zero after the liquid/vapor interface, at a height of 40 Å (not shown). The small circles in each figure mark the local maxima and minima in the density values, which were recorded and later compared to heat flux, thermal conductivity, and vibrational density of states (VDOS) data to look for underlying trends, though no strong correlations were found.

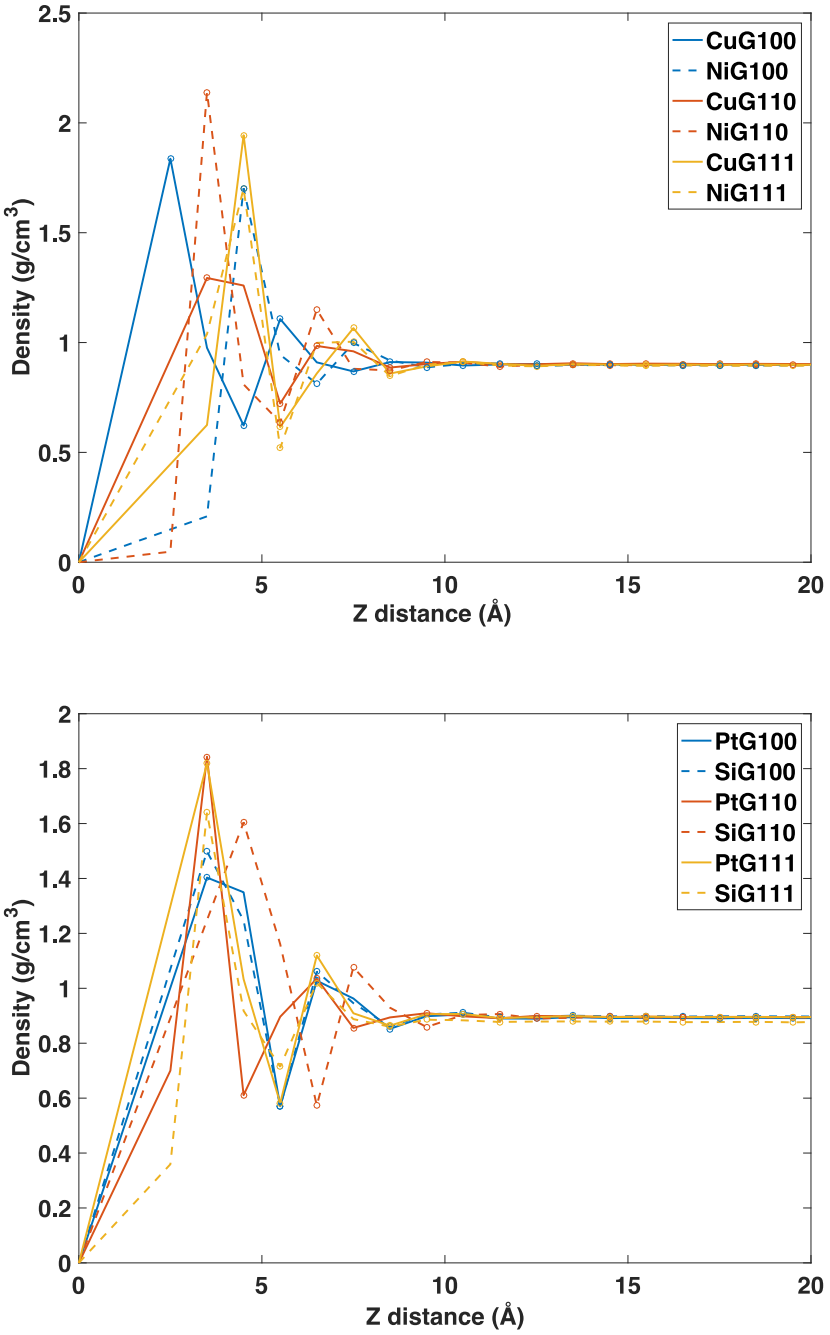

Figure 5.9: Phase II density profile for liquid water over (a) CuG and NiG, and (b) PtG and SiG substrates.

5.4 Conclusions

In this study molecular dynamics was used to simulate water boiling over a heated solid, which consisted of a substrate topped with a single graphene sheet, in order to enhance boiling heat transfer.

- The addition of a single layer graphene greatly improves the through-plane thermal conductivity of Cu, Ni, Pt, and Si substrates during boiling, with increases in conductivity 1-2 orders of magnitude greater than that of the substrate alone. The PtG100 case showed the best conductivity, just slightly below 148 W/mK.
- Density stratification of water was confirmed, with a region of alternating density maxima and minima near the graphene sheet before the bulk density was achieved after ~10Å.
- For cases involving coated graphene, the highest maximum flux value occurred in the CuG110 (~4.50 GW/m^2). However, bare substrates (w/o graphene) were also simulated and found to have higher initial peaks, most likely due to reduced Kapitza resistance.
- Stable heat flux values achieved by the end of the simulation time, however, tended to be higher for the graphene-containing cases, with ~2-10x increases over the plain substrate cases.
- The temperature gradients for SLG-coated substrates were found to be much lower than graphene-less substrates, especially shortly after the initial temperature rise. This is due to graphene's high thermal conductivity, which allows for more uniform heating.

- Nanoscale boiling curves were produced, comparing select SLG-coated and graphene-less cases. The CuG100 case showed a 14% increase in CHF (~0.36 GW/m^2) over the Cu100 case, and had higher fluxes in all stages of boiling. PtG100 showed a 9% increase in CHF (~0.48 GW/m^2) over the Pt100 case. The SLG-coated cases also required less superheat to achieve the CHF condition.
- Using VDOS data, an overlap ratio S_{GW}/S_{SW} was calculated and used to view heat flux trends. The stable heat flux correlated positively with the overlap ratio, suggesting that heat transfer improves with better substrate/graphene matching due to a reduction in thermal resistance.
- For all graphene sheet and substrate combinations in this study, no overlap ratio exceeded 0.5.

Chapter 6

Conclusions

Over the course of this work, MD investigations were carried out in order to improve upon the current knowledge of heat transfer mechanisms involved in nanoscale pool boiling.

The first investigation simulated the boiling of a thin liquid argon film on nano-pillared copper surfaces. While it is known that adding structures to a surface will enhance its heat transfer capabilities (due to an increase in heating surface area), the use of both hetero- and homogeneous wettability substrates had rarely been examined on the nanoscale. Two heating temperatures were considered: 105 K to view evaporative/nucleate boiling, and 300 K to induce explosive boiling. In order to track the number of vapor atoms throughout the simulation a criterion based on coordination number was used. Based on separate simulations carried out at saturation temperature and pressure, it was determined that any argon atom with less than 12 neighbors in a 5.3 Å radius was considered a vapor atom. This criterion can be used in future studies to aid in the viewing of nanoscale bubble incipience/growth.

For both normal and explosive boiling it was found that using a hydrophilic material for both the substrate base and nano-pillars resulted in the largest heat flux enhancement over the flat substrate case. During normal boiling the hydrophilic substrate topped with hydrophobic pillars showed no improvement over the flat case, while the hydrophobic substrate with hydrophilic pillars actually had decreased performance. In both cases it seems the reduced density due to the hydrophobic portions of the substrate cancelled out any heat transfer gain due to surface area. Steady heat

fluxes at the end of the simulation were between 70-90 MW/m^2. During explosive boiling all nanostructured surface showed improvement over the flat surface. The presence of pillars makes formation of the vapor layer more difficult, allowing for more heat transfer before the liquid film is ejected from the substrate. Steady heat fluxes were slightly increased from the low temperature case, to 100-150 GW/m^2.

In the next investigation, evaporation and film boiling of a thin liquid argon film on a nanostructured substrate were again simulated, with an emphasis on obtaining the transient boiling curve and determining the effect of wettability (via contact angle) and nanostructure pitch length. For constant pitch it was found that heat flux increased with decreases in contact angle, which follows most previous experimental works. Heat flux was also found to increase with increasing pitch. For pitches 65.1 Å and above, the degree of superheat required to reach film boiling increased with both increasing contact angle and pitch. The improved heat transfer brought about by wettability and pitch considerations delayed the onset of the film boiling condition and allowed higher peak flux values to be reached. The highest pitch (106.6 Å) and smallest contact angle (0°) case had a maximum heat flux of 159 MW/m^2. For smaller pitch cases the effect of small pitch and large contact angles results in the liquid's transition to a Cassie-Baxter state, further inhibiting heat transfer via a drastic reduction of solid-liquid contact area. Overall, increasing the pitch from 21.7 Å to 106.6 Å increased peak heat flux up to 36%, while going from a contact angle of 127° to 0° increased peak flux by as much as 90%. Many future avenues can yet be explored regarding heat flux based on contact angle and pitch. Further simulations should be performed exploring more super hydrophilic and

hydrophobic interaction potentials to further illuminate the relationship between peak flux and contact angle. The pitch of the nanostructures should also further be increased in order to determine its effect on peak flux, as well as the temperature at which the maximum flux occurs, though computational cost increases with pitch.

A final set of simulations investigated the heat transfer characteristics of single-layer graphene-topped substrates (Cu, Ni, Pt, and Si) during pool boiling of water. As expected, the addition of graphene improved the through-plane thermal conductivity of all substrates, with 1-2 orders of magnitude increases seen over plain substrates. This thermal conductivity also aided in reducing the temperature gradient when compared to graphene-less substrates, especially in the first half of the simulations.

While heating to 400 K, the heat flux profile for each substrate quickly reached a distinct maxima before dropping off exponentially and reaching a steady heat flux state. For SLG substrates the largest maximum flux value occurred on the 110-plane SLG-coated copper, and reached 4.5 GW/m^2. The plain substrates showed much higher initial maximums (as high as 15 GW/m^2) due to reduced interfacial thermal resistance. These maximum values, however, correlated inversely with the eventual steady flux values achieved, which were on the order of 10 MW/m^2. Steady fluxes for the SLG substrates were ~2-10x larger than those of the plain substrates. Nanoscale boiling curves for select cases were also determined, and it was found that the addition of SLG generally enhanced heat flux, and specifically increased CHF by as much as 14%. The SLG cases were also able to achieve the CHF condition at lower superheats than the non-graphene cases. A criterion was also developed to determine the degree of vibrational mismatch between substrates and graphene. The ratio of the overlap of VDOS spectra (S_{GW}/S_{SW})

can be used to predict heat flux trends. Future graphene-related work should aim to further characterize the CHF and VDOS characteristics of the substrate/graphene sheet combinations, including investigation of the Kapitza resistance/conductance and its relation to the overlap ratio, spectral temperature, heat flux, etc. Imperfect and/or multiple graphene sheets should also be considered.

References

1. Cahill, D.G., Goodson, K. and Majumdar, A., 2002. Thermometry and thermal transport in micro/nanoscale solid-state devices and structures. *Journal of Heat Transfer*, *124*(2), pp.223-241.
2. Chen, G., 2005. *Nanoscale energy transport and conversion: a parallel treatment of electrons, molecules, phonons, and photons*. Oxford University Press.
3. Wu, Z. and Sundén, B., 2014. On further enhancement of single-phase and flow boiling heat transfer in micro/minichannels. *Renewable and Sustainable Energy Reviews*, *40*, pp.11-27.
4. Amon, C.H., Yao, S.C., Wu, C.F. and Hsieh, C.C., 2005. Microelectromechanical system-based evaporative thermal management of high heat flux electronics. *Journal of Heat Transfer*, *127*(1), pp.66-75.
5. Mudawar, I., 2001. Assessment of high-heat-flux thermal management schemes. *IEEE Transactions on Components and Packaging Technologies*, *24*(2), pp.122-141.
6. Kandlikar, S.G., 2013. Controlling bubble motion over heated surface through evaporation momentum force to enhance pool boiling heat transfer. *Applied Physics Letters*, *102*(5), p.051611.
7. Kandlikar, S.G., 2010. Similarities and differences between flow boiling in microchannels and pool boiling. *Heat Transfer Engineering*, *31*(3), pp.159-167.
8. Lienhard, J.H. and Witte, L.C., 1985. An historical review of the hydrodynamic theory of boiling. *Reviews in Chemical Engineering*, *3*(3-4), pp.187-280.
9. Nukiyama, S., 1934. Maximum and minimum values of heat q transmitted from metal to water under atmospheric pressure. *Society of Mechanical Engineers of Japan. l934 (37)*, *354*(367), p.2.
10. Farber, E.A. and Scorah, R.L., 1948. Heat transfer to water boiling under pressure. *Transactions of the American Society of Mechanical Engineers*, *70*, pp.369-384.
11. Johnson, R.W. ed., 2016. *Handbook of fluid dynamics*. Crc Press.
12. Rohsenow, W.M., 1951. A method of correlating heat transfer data for surface boiling of liquids. *Cambridge, Mass.: MIT Division of Industrial Cooperation*.
13. Fritz, W., 1935, Maximum Volume of Vapor Bubbles, *Physik Zeitschr.,* 36, pp. 379-384.
14. Plesset, M.S. and Zwick, S.A., 1954. The growth of vapor bubbles in superheated liquids. *Journal of Applied Physics*, *25*(4), pp.493-500.
15. Mikic, B.B., Rohsenow, W.M. and Griffith, P., 1970. On bubble growth rates. *International Journal of Heat and Mass Transfer*, *13*(4), pp.657-666.

16. Lienhard, J.H. and Dhir, V.K., 1973. Extended hydrodynamic theory of the peak and minimum pool boiling heat fluxes. *NASA CR-2270*

17. Kutateladze, S.S., 1948. On the transition to film boiling under natural convection. *Kotloturbostroenie*, *3*, pp.10-12.

18. Zuber, N., 1958. On the stability of boiling heat transfer. *Transactions of the American Society Mechanical Engineers.*, *80*., p.711-720

19. Tien, C.L., 1962. A hydrodynamic model for nucleate pool boiling. *International Journal of Heat and Mass Transfer*, *5*(6), pp.533-540.

20. Hsu, Y.Y. and Graham, R.W., 1961, Analytical and Experimental Study of Thermal Boundary Layer and Ebullition Cycle in Nucleate Boiling, *National Aeronautics and Space Administration–Technical Notes*, TN-D-594, p. 43.

21. Hsu, Y.Y., 1962. On the size range of active nucleation cavities on a heating surface. *Journal of Heat Transfer*, *84*(3), pp.207-213.

22. Cooper, M.G. and Lloyd, A.J.P., 1969. The microlayer in nucleate pool boiling. *International Journal of Heat and Mass Transfer*, *12*(8), pp.895-913.

23. Chatterjee, A., Plawsky, J.L. and Wayner Jr, P.C., 2011. Disjoining pressure and capillarity in the constrained vapor bubble heat transfer system. *Advances in Colloid and Interface Science*, *168*(1-2), pp.40-49.

24. Siedel, S., Cioulachtjian, S. and Bonjour, J., 2008. Experimental analysis of bubble growth, departure and interactions during pool boiling on artificial nucleation sites. *Experimental Thermal and Fluid Science*, *32*(8), pp.1504-1511.

25. Demiray, F. and Kim, J., 2004. Microscale heat transfer measurements during pool boiling of FC-72: effect of subcooling. *International Journal of Heat and Mass Transfer*, *47*(14-16), pp.3257-3268.

26. Myers, J.G., Yerramilli, V.K., Hussey, S.W., Yee, G.F. and Kim, J., 2005. Time and space resolved wall temperature and heat flux measurements during nucleate boiling with constant heat flux boundary conditions. *International Journal of Heat and Mass Transfer*, *48*(12), pp.2429-2442.

27. Kim, J., Do Oh, B. and Kim, M.H., 2006. Experimental study of pool temperature effects on nucleate pool boiling. *International Journal of Multiphase Flow*, *32*(2), pp.208-231.

28. Costello, C.P. and Frea, W.J., 1963. A salient nonhydrodynamic effect on pool boiling burnout of small semicylindrical heaters. In *AIChE Chemical Engineering Progress Symposium Series*, *61*(57), pp. 258-268.

29. Gaertner, R.F., 1963. Effect of Heater Surface Chemistry on the Level of Burnout Heat Flux in Pool Boiling, *Technical Information Series*, No. 63-RL- 3449C, General Electric Research Laboratory, Schenectady, New York.

30. Kandlikar, S.G., 2001. A theoretical model to predict pool boiling CHF incorporating effects of contact angle and orientation. *Journal of Heat Transfer*, *123*(6), pp.1071-1079.

31. Lee, C.Y., Bhuiya, M.M.H. and Kim, K.J., 2010. Pool boiling heat transfer with nano-porous surface. *International Journal of Heat and Mass Transfer*, *53*(19-20), pp.4274-4279.

32. Kim, H., Kim, J. and Kim, M.H., 2006. Effect of nanoparticles on CHF enhancement in pool boiling of nano-fluids. *International Journal of Heat and Mass Transfer*, *49*(25-26), pp.5070-5074.

33. Kim, S.J., Bang, I.C., Buongiorno, J. and Hu, L.W., 2006. Effects of nanoparticle deposition on surface wettability influencing boiling heat transfer in nanofluids. *Applied Physics Letters*, *89*(15), p.153107.

34. Mitrovic, J.,and Hartmann, F., 2004. A New Microstructure for Pool Boiling. Superlattices and Microstructures, *35*(3–6), pp. 617–628.

35. Wei, J.J. and Honda, H., 2003. Effects of fin geometry on boiling heat transfer from silicon chips with micro-pin-fins immersed in FC-72. *International Journal of Heat and Mass Transfer*, *46*(21), pp.4059-4070.

36. Cooke, D. and Kandlikar, S.G., 2011. Pool boiling heat transfer and bubble dynamics over plain and enhanced microchannels. *Journal of Heat Transfer*, *133*(5), p.052902.

37. Ahn, H.S., Sathyamurthi, V. and Banerjee, D., 2009. Pool boiling experiments on a nano-structured surface. *IEEE Transactions on Components and PackagingTtechnologies*, *32*(1), pp.156-165.

38. Hendricks, T.J., Krishnan, S., Choi, C., Chang, C.H. and Paul, B., 2010. Enhancement of pool-boiling heat transfer using nanostructured surfaces on aluminum and copper. *International Journal of Heat and Mass Transfer*, *53*(15-16), pp.3357-3365.

39. Li, C., Wang, Z., Wang, P.I., Peles, Y., Koratkar, N. and Peterson, G.P., 2008. Nanostructured copper interfaces for enhanced boiling. *Small*, *4*(8), pp.1084-1088.

40. Theofanous, T.G., Tu, J.P., Dinh, A.T. and Dinh, T.N., 2002. The boiling crisis phenomenon: Part I: nucleation and nucleate boiling heat transfer. *Experimental thermal and fluid science*, *26*(6-7), pp.775-792.

41. Cavicchi, R.E. and Avedisian, C.T., 2007. Bubble nucleation and growth anomaly for a hydrophilic microheater attributed to metastable nanobubbles. *Physical review letters*, *98*(12), p.124501.

42. Dong, L., Quan, X. and Cheng, P., 2014. An experimental investigation of enhanced pool boiling heat transfer from surfaces with micro/nano-structures. *International Journal of Heat and Mass Transfer*, *71*, pp.189-196.

43. Weibel, J.A., Garimella, S.V. and North, M.T., 2010. Characterization of evaporation and boiling from sintered powder wicks fed by capillary action. *International Journal of Heat and Mass Transfer*, *53*(19-20), pp.4204-4215.

44. Chowdhury, S.R. and Winterton, R.H.S., 1985. Surface effects in pool boiling. *International Journal of Heat and Mass Transfer*, *28*(10), pp.1881-1889.

45. Maracy, M. and Winterton, R.H.S., 1988. Hysteresis and contact angle effects in transition pool boiling of water. *International Journal of Heat and Mass Transfer*, *31*(7), pp.1443-1449.

46. Wang, C.H. and Dhir, V.K., 1993. Effect of surface wettability on active nucleation site density during pool boiling of water on a vertical surface. *Journal of Heat Transfer*, *115*(3), pp.659-669.

47. Grigoriev, V.A., Pavlov, Y.M. and Ametistov, E.V., 1973. About correlation of experimental data for heat transfer under boiling of some cryogenic fluids in a large volume. *Thermal Engineering*, *9*, pp.57-63.

48. Ahn, H.S., Jo, H.J., Kang, S.H. and Kim, M.H., 2011. Effect of liquid spreading due to nano/microstructures on the critical heat flux during pool boiling. *Applied Physics Letters*, *98*(7), p.071908.

49. Betz, A.R., Xu, J., Qiu, H. and Attinger, D., 2010. Do surfaces with mixed hydrophilic and hydrophobic areas enhance pool boiling?. *Applied Physics Letters*, *97*(14), p.141909.

50. Jo, H., Ahn, H.S., Kang, S. and Kim, M.H., 2011. A study of nucleate boiling heat transfer on hydrophilic, hydrophobic and heterogeneous wetting surfaces. *International Journal of Heat and Mass Transfer*, *54*(25-26), pp.5643-5652.

51. Maruyama, S., Shoji, M. and Shimizu, S., 1992. A numerical simulation of transition boiling heat transfer, *Proceedings of the Second JSME–KSME Thermal Engineering Conference*, pp. 3-345-3-348.

52. Maruyama, S., Tatsuto, K. and Yamaguchi, Y., 1997. A molecular dynamics simulation of a bubble nucleation on solid surface. *National Heat Transfer Symposium of Japan, 34*, pp. 675-676.

53. Son, G., Dhir, V.K. and Ramanujapu, N., 1999. Dynamics and heat transfer associated with a single bubble during nucleate boiling on a horizontal surface. *Journal of Heat Transfer*, *121*(3), pp.623-631.

54. Son, G., Ramanujapu, N. and Dhir, V.K., 2002. Numerical simulation of bubble merger process on a single nucleation site during pool nucleate boiling. *Journal of Heat Transfer*, *124*(1), pp.51-62.

55. Mukherjee, A. and Dhir, V.K., 2004. Study of lateral merger of vapor bubbles during nucleate pool boiling. *Journal of Heat Transfer*, *126*(6), pp.1023-1039.

56. Matsumoto, S., Maruyama, S. and Saruwatari, H., 1997. Molecular Dynamics Simulation of a Liquid Droplet on a Solid Surface. *Japanese Journal of Tribology*, *42*, pp.143-152.

57. Sarkar, S. and Selvam, R.P., 2007. Molecular dynamics simulation of effective thermal conductivity and study of enhanced thermal transport mechanism in nanofluids. *Journal of applied physics*, *102*(7), p.074302.

58. Li, L., Zhang, Y., Ma, H. and Yang, M., 2010. Molecular dynamics simulation of effect of liquid layering around the nanoparticle on the enhanced thermal conductivity of nanofluids. *Journal of Nanoparticle Research*, *12*(3), pp.811-821.

59. Merabia, S., Keblinski, P., Joly, L., Lewis, L.J. and Barrat, J.L., 2009. Critical heat flux around strongly heated nanoparticles. *Physical Review E*, *79*(2), p.021404.

60. Yasuoka, K. and Matsumoto, M., 1998. Molecular dynamics of homogeneous nucleation in the vapor phase. II. Water. *The Journal of Chemical Physics*, *109*(19), pp.8463-8470.

61. Yi, P., Poulikakos, D., Walther, J. and Yadigaroglu, G., 2002. Molecular dynamics simulation of vaporization of an ultra-thin liquid argon layer on a surface. *International Journal of Heat and Mass Transfer*, *45*(10), pp.2087-2100.

62. Nagayama, G. and Tsuruta, T., 2003. A general expression for the condensation coefficient based on transition state theory and molecular dynamics simulation. *The Journal of Chemical Physics*, *118*(3), pp.1392-1399.

63. Yang, T.H. and Pan, C., 2005. Molecular dynamics simulation of a thin water layer evaporation and evaporation coefficient. *International Journal of Heat and Mass Transfer*, *48*(17), pp.3516-3526.

64. Maroo, S.C. and Chung, J.N., 2008. Molecular dynamic simulation of platinum heater and associated nano-scale liquid argon film evaporation and colloidal adsorption characteristics. *Journal of Colloid and Interface Science*, *328*(1), pp.134-146.

65. Zou, Y., Huai, X. and Lin, L., 2010. Molecular dynamics simulation for homogeneous nucleation of water and liquid nitrogen in explosive boiling. *Applied Thermal Engineering*, *30*(8-9), pp.859-863.

66. Morshed, A.K.M.M., Paul, T.C. and Khan, J.A., 2011. Effect of nanostructures on evaporation and explosive boiling of thin liquid films: a molecular dynamics study. *Applied Physics A*, *105*(2), pp.445-451.

67. Seyf, H.R. and Zhang, Y., 2013. Molecular dynamics simulation of normal and explosive boiling on nanostructured surface. *Journal of Heat Transfer*, *135*(12), p.121503.

68. Hens, A., Agarwal, R. and Biswas, G., 2014. Nanoscale study of boiling and evaporation in a liquid Ar film on a Pt heater using molecular dynamics simulation. *International Journal of Heat and Mass Transfer*, *71*, pp.303-312.

69. Wang, W., Huang, S. and Luo, X., 2016. MD simulation on nano-scale heat transfer mechanism of sub-cooled boiling on nano-structured surface. *International Journal of Heat and Mass Transfer*, *100*, pp.276-286.

70. Allen, M.P. and Tildesley, D.J., 2017. *Computer simulation of liquids*. Oxford University Press.

71. Buckingham, R.A., 1938. The Classical Equation of State of Gaseous Helium, Neon and Argon. *Proceedings of the Royal Society A: Mathematical and Physical Sciences*, *168*(933), pp.264–283.

72. Stockmayer, W.H., 1941. Second virial coefficients of polar gases. *Journal of Chemical Physics, 9*, pp.398-402.

73. Morse, P. M., 1929. Diatomic molecules according to the wave mechanics. II. Vibrational levels. *Physical Rev*iew *34*. pp.57–64.

74. Daw, M.S. and Baskes, M.I., 1984. Embedded-atom method: Derivation and application to impurities, surfaces, and other defects in metals. *Physical Review B*, *29*(12), p.6443.

75. Tersoff, J., 1986. New empirical model for the structural properties of silicon. *Physical Review Letters*, *56*(6), p.632.

76. Stillinger, F.H. and Weber, T.A., 1985. Computer simulation of local order in condensed phases of silicon. *Physical Review B*, *31*(8), p.5262.

77. Stuart, S.J., Tutein, A.B. and Harrison, J.A., 2000. A reactive potential for hydrocarbons with intermolecular interactions. *The Journal of chemical physics*, *112*(14), pp.6472-6486.

78. Brenner, D.W., Sinnott, S.B. and Harrison, J.A., 1990. Reactive empirical bond order (REBO) potential energy expression for hydrocarbons. *Physical Review B*, *42*, pp.9458-9470.

79. Trokhymchuk, A. and Alejandre, J., 1999. Computer simulations of liquid/vapor interface in Lennard-Jones fluids: Some questions and answers. *The Journal of Chemical Physics*, *111*(18), pp.8510-8523.

80. Stoddard, S.D. and Ford, J., 1973. Numerical experiments on the stochastic behavior of a Lennard-Jones gas system. *Physical Review A*, *8*(3), p.1504.

81. Guo, M. and Lu, B.C.Y., 1997. Long range corrections to thermodynamic properties of inhomogeneous systems with planar interfaces. *The Journal of Chemical Physics*, *106*(9), pp.3688-3695.

82. Kovács, I. and Nemes, L., 1969. *Rotational structure in the spectra of diatomic molecules* (pp. 272-274). London: Hilger.

83. Rector, D.R., Van Swol, F. and Henderson, J.R., 1994. Simulation of surfactant solutions: I. Micelle formation in the bulk phase. *Molecular Physics*, *82*(5), pp.1009-1031.

84. Kremer, K. and Grest, G.S., 1990. Dynamics of entangled linear polymer melts: A molecular‐dynamics simulation. *The Journal of Chemical Physics*, *92*(8), pp.5057-5086.

85. Lifson, S. and Warshel, A., 1968. Consistent force field for calculations of conformations, vibrational spectra, and enthalpies of cycloalkane and n‐alkane molecules. *The Journal of Chemical Physics*, *49*(11), pp.5116-5129.

86. Gear, C.W., 1971. Numerical Initial Value Problems in Ordinary Differential Equations. Prentice Hall.

87. Verlet, L., 1967. Computer" experiments" on classical fluids. I. Thermodynamical properties of Lennard-Jones molecules. *Physical review*, *159*(1), p.98.

88. Swope, W.C., Andersen, H.C., Berens, P.H. and Wilson, K.R., 1982. A computer simulation method for the calculation of equilibrium constants for the formation of physical clusters of molecules: Application to small water clusters. *The Journal of Chemical Physics*, *76*(1), pp.637-649.

89. Tuckerman, M.B.B.J.M., Berne, B.J. and Martyna, G.J., 1992. Reversible multiple time scale molecular dynamics. *The Journal of Chemical Physics*, *97*(3), pp.1990-2001.

90. Ryckaert, J.P., Ciccotti, G. and Berendsen, H.J.C., 1977. Numerical Integration of the Cartesian Equations of Motion of a System with Constraints: Molecular Dynamics of *n*-Alkanes. *Journal of Computational Physics*. *23*(3): 327–341.

91. Andersen, H.C., 1983. Rattle: A “velocity” version of the shake algorithm for molecular dynamics calculations. *Journal of Computational Physics*, *52*(1), pp.24-34.

92. Hess, B., Bekker, H., Berendsen, H.J.C. and Fraaije, J.G.E.M., 1997. LINCS: A Linear Constraint Solver for Molecular Simulations. *Journal of Computational Chemistry*, *18*(12), pp.1463–1472.

93. Berendsen, H.J., Postma, J.V., van Gunsteren, W.F., DiNola, A.R.H.J. and Haak, J.R., 1984. Molecular dynamics with coupling to an external bath. *The Journal of Chemical Physics*, *81*(8), pp.3684-3690.

94. Schneider, T. and Stoll, E., 1978. Molecular-dynamics study of a three-dimensional one-component model for distortive phase transitions. *Physical Review B*, *17*(3), p.1302.

95. Griebel, M., Knapek, S. and Zumbusch, G., 2007. Numerical Simulation in Molecular Dynamics. Numerics, Algorithms, Parallelization, Applications, Volume 5 of Texts in Computational Science and Engineering. Springer.

96. Wei, J., Zhao, J., Yuan, M. and Xue, Y., 2009. Boiling heat transfer enhancement by using micro-pin-finned surface for electronics cooling. *Microgravity Science and Technology*, *21*(1), pp.159-173.

97. Wen, D., Lin, G., Vafaei, S. and Zhang, K., 2009. Review of nanofluids for heat transfer applications. *Particuology*, *7*(2), pp.141-150.

98. Madhour, Y., Olivier, J., Costa-Patry, E., Paredes, S., Michel, B. and Thome, J.R., 2011. Flow boiling of R134a in a multi-microchannel heat sink with hotspot heaters for energy-efficient microelectronic CPU cooling applications. *IEEE Transactions on Components, Packaging and Manufacturing Technology*, *1*(6), pp.873-883.

99. Herrault, F., Hidalgo, P.A., Ji, C.H., Glezer, A. and Allen, M.G., 2012, January. Cooling performance of micromachined self-oscillating reed actuators in heat transfer channels with integrated diagnostics. In *Micro Electro Mechanical Systems (MEMS), 2012 IEEE 25th International Conference,* pp. 1217-1220.

100. Cosley, M.R., Fischer, R.L., Thiesen, J.H. and Willen, G.S., Marconi Communications Inc, 2004. *Small scale chip cooler assembly*. U.S. Patent 6,679,315.

101. Zou, Y., Cai, J., Huai, X., Xin, F. and Guo, Z., 2014. Molecular dynamics simulation of heat conduction in Si nano-films induced by ultrafast laser heating. *Thin Solid Films*, *558*, pp.455-461.

102. Semironi, D.T. and Azimian, A.R., 2010. Molecular dynamics simulation of liquid–vapor phase equilibrium by using the modified Lennard-Jones potential function. *Heat and mass transfer*, *46*(3), pp.287-294.

103. Xu, J.L. and Zhou, Z.Q., 2004. Molecular dynamics simulation of liquid argon flow at platinum surfaces. *Heat and Mass Transfer*, *40*(11), pp.859-869.

104. Noorian, H., Toghraie, D. and Azimian, A.R., 2014. The effects of surface roughness geometry of flow undergoing Poiseuille flow by molecular dynamics simulation. *Heat and Mass Transfer*, *50*(1), pp.95-104.

105. Ji, C.Y. and Yan, Y.Y., 2008. A molecular dynamics simulation of liquid–vapour–solid system near triple-phase contact line of flow boiling in a microchannel. *Applied thermal engineering*, *28*(2-3), pp.195-202.

106. Shi, B. and Dhir, V.K., 2009. Molecular dynamics simulation of the contact angle of liquids on solid surfaces. *The Journal of chemical physics*, *130*(3), p.034705.

107. Fu, T., Mao, Y., Tang, Y., Zhang, Y. and Yuan, W., 2016. Effect of nanostructure on rapid boiling of water on a hot copper plate: a molecular dynamics study. *Heat and Mass Transfer*, *52*(8), pp.1469-1478.

108. Mao, Y. and Zhang, Y., 2014. Molecular dynamics simulation on rapid boiling of water on a hot copper plate. *Applied Thermal Engineering*, *62*(2), pp.607-612.

109. Schneider, T. and Stoll, E., 1978. Molecular-dynamics study of a three-dimensional one-component model for distortive phase transitions. *Physical Review B*, *17*(3), p.1302.

110. Dünweg, B. and Paul, W., 1991. Brownian dynamics simulations without Gaussian random numbers. *International Journal of Modern Physics C*, *2*(03), pp.817-827.

111. Plimpton, S., 1995. Fast parallel algorithms for short-range molecular dynamics. *Journal of computational physics*, *117*(1), pp.1-19. http://lammps.sandia.gov - Sandia National Laboratories, USA.

112. Humphrey, W., Dalke, A. and Schulten, K., 1996. VMD: visual molecular dynamics. *Journal of molecular graphics*, *14*(1), pp.33-38.

113. Gilgen, R., Kleinrahm, R. and Wagner, W., 1994. Measurement and correlation of the (pressure, density, temperature) relation of argon II. Saturated-liquid and saturated-vapour densities and vapour pressures along the entire coexistence curve. *The Journal of Chemical Thermodynamics*, *26*(4), pp.399-413.

114. Gambill, W.R. and Lienhard, J.H., 1989. An upper bound for the critical boiling heat flux. *ASME J. Heat Transfer*, *111*(3), pp.815-818.

115. Wang, H.C., Jewell-Larsen, N.E. and Mamishev, A.V., 2013. Thermal management of microelectronics with electrostatic fluid accelerators. *Applied Thermal Engineering*, *51*(1-2), pp.190-211.

116. Hamann, H.F., Weger, A., Lacey, J.A., Hu, Z., Bose, P., Cohen, E. and Wakil, J., 2007. Hotspot-limited microprocessors: Direct temperature and power distribution measurements. *IEEE Journal of Solid-State Circuits*, *42*(1), pp.56-65.

117. Narayanan, S., Fedorov, A.G. and Joshi, Y.K., 2009. Gas-assisted thin-film evaporation from confined spaces for dissipation of high heat fluxes. *Nanoscale and Microscale Thermophysical Engineering*, *13*(1), pp.30-53.

118. Narayanan, S., Fedorov, A.G. and Joshi, Y.K., 2010. On-chip thermal management of hotspots using a perspiration nanopatch. *Journal of micromechanics and microengineering*, *20*(7), p.075010.

119. Ahn, H. and Son, G., 2015. Numerical simulation of liquid film evaporation in circular and square microcavities. *Numerical Heat Transfer, Part A: Applications*, *67*(9), pp.934-951.

120. Chu, K.H., Enright, R. and Wang, E.N., 2012. Structured surfaces for enhanced pool boiling heat transfer. *Applied Physics Letters*, *100*(24), p.241603.

121. Maruyama, S. and Kimura, T., 1999. A study on thermal resistance over a solid-liquid interface by the molecular dynamics method. *Thermal Sciences and Engineering*, *7*(1), pp.63-68.

122. Isaiev, M., Burian, S., Bulavin, L., Gradeck, M., Lemoine, F. and Termentzidis, K., 2016. Efficient tuning of potential parameters for liquid–solid interactions. *Molecular Simulation*, *42*(11), pp.910-915.

123. Srivastava, M., 2015. Image Processing and Analysis of Vapor Bubbles Nucleated in Thin Liquid Film Boiling, Masters thesis, North Carolina State University, Raleigh, NC.

124. Hsu, C.C. and Chen, P.H., 2012. Surface wettability effects on critical heat flux of boiling heat transfer using nanoparticle coatings. *International Journal of Heat and Mass Transfer*, *55*(13-14), pp.3713-3719.

125. Balandin, A.A., 2011. Thermal properties of graphene and nanostructured carbon materials. *Nature materials*, *10*(8), p.569.

126. Nika, D.L., Pokatilov, E.P., Askerov, A.S. and Balandin, A.A., 2009. Phonon thermal conduction in graphene: Role of Umklapp and edge roughness scattering. *Physical Review B*, *79*(15), p.155413.

127. Zhong, W.R., Zhang, M.P., Ai, B.Q. and Zheng, D.Q., 2011. Chirality and thickness-dependent thermal conductivity of few-layer graphene: A molecular dynamics study. *Applied Physics Letters*, *98*(11), p.113107.

128. Ouyang, T., Chen, Y., Xie, Y., Wei, X.L., Yang, K., Yang, P. and Zhong, J., 2010. Ballistic thermal rectification in asymmetric three-terminal graphene nanojunctions. *Physical Review B*, *82*(24), p.245403.

129. Chang, S.W., Nair, A.K. and Buehler, M.J., 2012. Geometry and temperature effects of the interfacial thermal conductance in copper–and nickel–graphene nanocomposites. *Journal of Physics: Condensed Matter*, *24*(24), p.245301.

130. Alexeev, D., Chen, J., Walther, J.H., Giapis, K.P., Angelikopoulos, P. and Koumoutsakos, P., 2015. Kapitza resistance between few-layer graphene and water: Liquid layering effects. *Nano letters*, *15*(9), pp.5744-5749.

131. Seo, H., Chu, J.H., Kwon, S.Y. and Bang, I.C., 2015. Pool boiling CHF of reduced graphene oxide, graphene, and SiC-coated surfaces under highly wettable FC-72. *International Journal of Heat and Mass Transfer*, *82*, pp.490-502.

132. Jaikumar, A., Kandlikar, S.G. and Gupta, A., 2017. Pool boiling enhancement through graphene and graphene oxide coatings. *Heat Transfer Engineering*, *38*(14-15), pp.1274-1284.

133. Choi, W., Lahiri, I., Seelaboyina, R. and Kang, Y.S., 2010. Synthesis of graphene and its applications: a review. *Critical Reviews in Solid State and Materials Sciences*, *35*(1), pp.52-71.

134. Dahal, A. and Batzill, M., 2014. Graphene–nickel interfaces: a review. *Nanoscale*, *6*(5), pp.2548-2562.

135. Berendsen, H.J.C., Grigera, J.R. and Straatsma, T.P., 1987. The missing term in effective pair potentials. *Journal of Physical Chemistry*, *91*(24), pp.6269-6271.

136. Hockney, R.W. and Eastwood, J.W., 1981. *Computer simulation using particles*. McGraw-Hill.

137. Guo, Y. and Guo, W., 2006. Structural transformation of partially confined copper nanowires inside defected carbon nanotubes. *Nanotechnology*, *17*(18), p.4726.

138. Zhu, S.B. and Philpott, M.R., 1994. Interaction of water with metal surfaces. *The Journal of chemical physics*, *100*(9), pp.6961-6968.

139. Schebarchov, D. and Hendy, S.C., 2011. Effects of epitaxial strain on the melting of supported nickel nanoparticles. *Physical Review B*, *84*(8), p.085407.

140. Morrow, B.H. and Striolo, A., 2008. Platinum nanoparticles on carbonaceous materials: the effect of support geometry on nanoparticle mobility, morphology, and melting. *Nanotechnology*, *19*(19), p.195711.

141. Svishchev, I.M. and Kusalik, P.G., 1993. Structure in liquid water: A study of spatial distribution functions. *The Journal of chemical physics*, *99*(4), pp.3049-3058.

142. Li, X., Li, L., Wang, Y., Li, H. and Bian, X., 2013. Wetting and interfacial properties of water on the defective graphene. *The Journal of Physical Chemistry C*, *117*(27), pp.14106-14112.

143. Shi, B., Sinha, S. and Dhir, V.K., 2006. Molecular dynamics simulation of the density and surface tension of water by particle-particle particle-mesh method. *The Journal of chemical physics*, *124*(20), p.204715.

144. Lan, J. and Li, B., 2006. Thermal rectifying effect in two-dimensional anharmonic lattices. *Physical Review B*, *74*(21), p.214305.

145. Momenzadeh, L., Evteev, A.V., Levchenko, E.V., Belova, I.V., Murch, G.E. and Sohn, Y.H., 2013. Phonon Thermal Conductivity of fcc Cu by Molecular Dynamics Simulation. *Defect and Diffusion Forum*, *336*, pp.169-184.

146. Yao, M., Zebarjadi, M. and Opeil, C.P., 2017. Experimental determination of phonon thermal conductivity and Lorenz ratio of single crystal metals: Al, Cu, and Zn. *Journal of Applied Physics*, *122*(13), p.135111.

147. Ou, M.N., Yang, T.J., Harutyunyan, S.R., Chen, Y.Y., Chen, C.D. and Lai, S.J., 2008. Electrical and thermal transport in single nickel nanowire. *Applied Physics Letters*, *92*(6), p.063101.

148. Heino, P. and Ristolainen, E., 2003. Thermal conduction at the nanoscale in some metals by MD. *Microelectronics journal*, *34*(9), pp.773-777.

149. Esfarjani, K., Chen, G. and Stokes, H.T., 2011. Heat transport in silicon from first-principles calculations. *Physical Review B*, *84*(8), p.085204.

150. Evans, W.J., Hu, L. and Keblinski, P., 2010. Thermal conductivity of graphene ribbons from equilibrium molecular dynamics: Effect of ribbon width, edge roughness, and hydrogen termination. *Applied Physics Letters*, *96*(20), p.203112.

151. Seol, J.H., Jo, I., Moore, A.L., Lindsay, L., Aitken, Z.H., Pettes, M.T., Li, X., Yao, Z., Huang, R., Broido, D. and Mingo, N., 2010. Two-dimensional phonon transport in supported graphene. *Science*, *328*(5975), pp.213-216.

152. Ong, Z.Y. and Pop, E., 2011. Effect of substrate modes on thermal transport in supported graphene. *Physical Review B*, *84*(7), p.075471.

153. Alofi, A. and Srivastava, G.P., 2013. Thermal conductivity of graphene and graphite. *Physical Review B*, *87*(11), p.115421.

154. Mao, R., Kong, B.D., Gong, C., Xu, S., Jayasekera, T., Cho, K. and Kim, K.W., 2013. First-principles calculation of thermal transport in metal/graphene systems. *Physical Review B*, *87*(16), p.165410.

155. Hu, L., Desai, T. and Keblinski, P., 2011. Determination of interfacial thermal resistance at the nanoscale. *Physical Review B*, *83*(19), p.195423.

156. Shen, M., Schelling, P.K. and Keblinski, P., 2013. Heat transfer mechanism across few-layer graphene by molecular dynamics. *Physical Review B*, *88*(4), p.045444.

157. Walther, J.H., Jaffe, R., Halicioglu, T. and Koumoutsakos, P., 2001. Carbon nanotubes in water: structural characteristics and energetics. *The Journal of Physical Chemistry B*, *105*(41), pp.9980-9987.

158. Gordillo, M.C. and Marti, J., 2010. Water on graphene surfaces. *Journal of Physics: Condensed Matter*, *22*(28), p.284111.

Appendix A
Additional Figures for Chapter 3

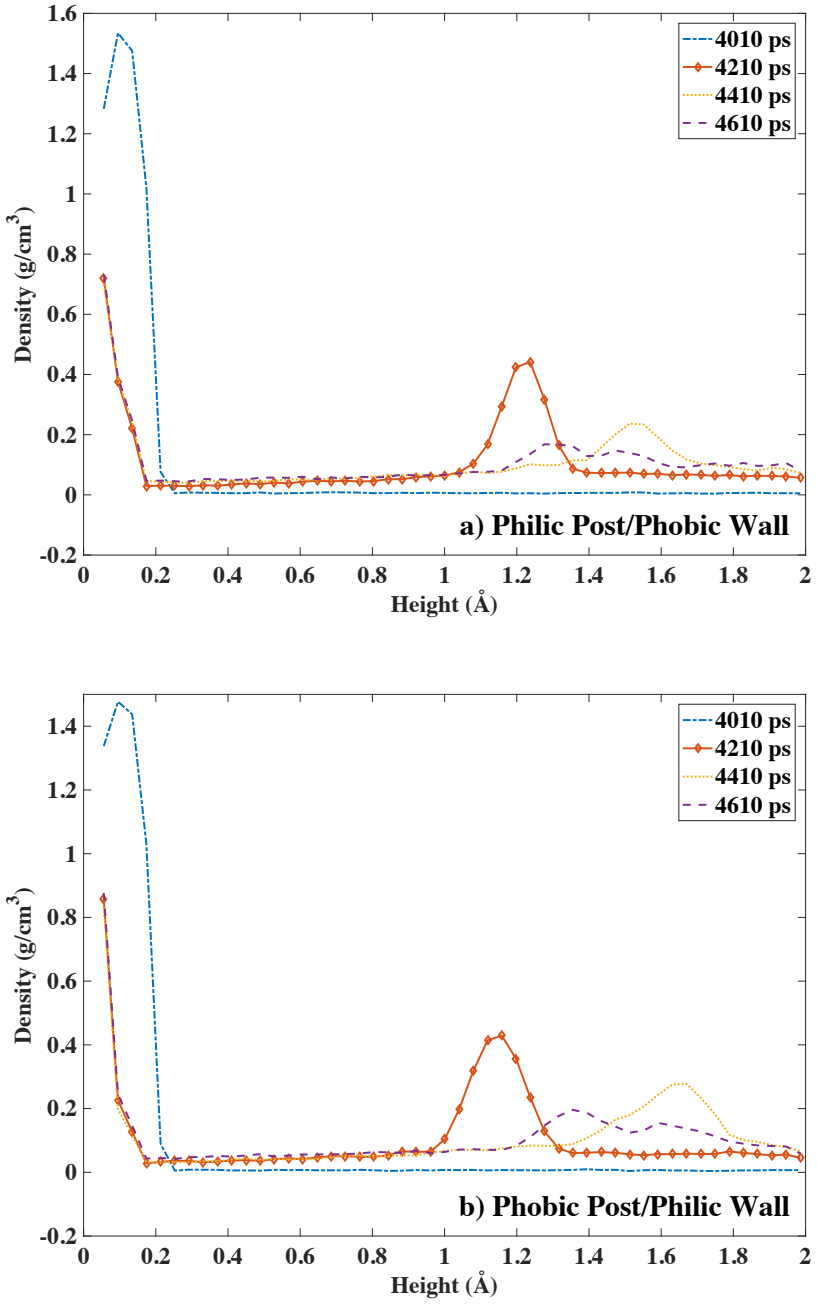

Figure A.1: Ar density profiles at different times for a) Philic Post/Phobic Wall and b) Phobic Post/Philic Wall (high temperature cases).

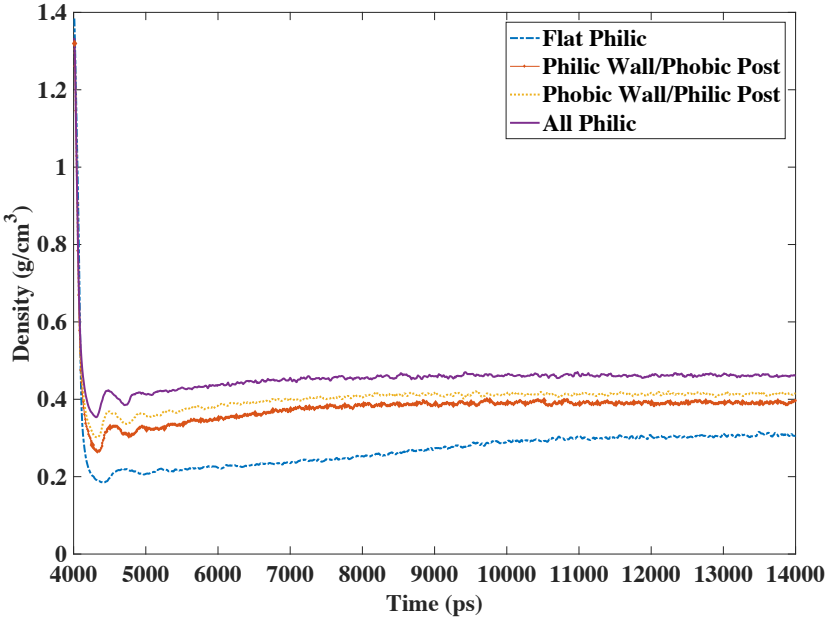

Figure A.2: Ar density evolution (high temperature cases).

Appendix B

Additional Figures for Chapter 4

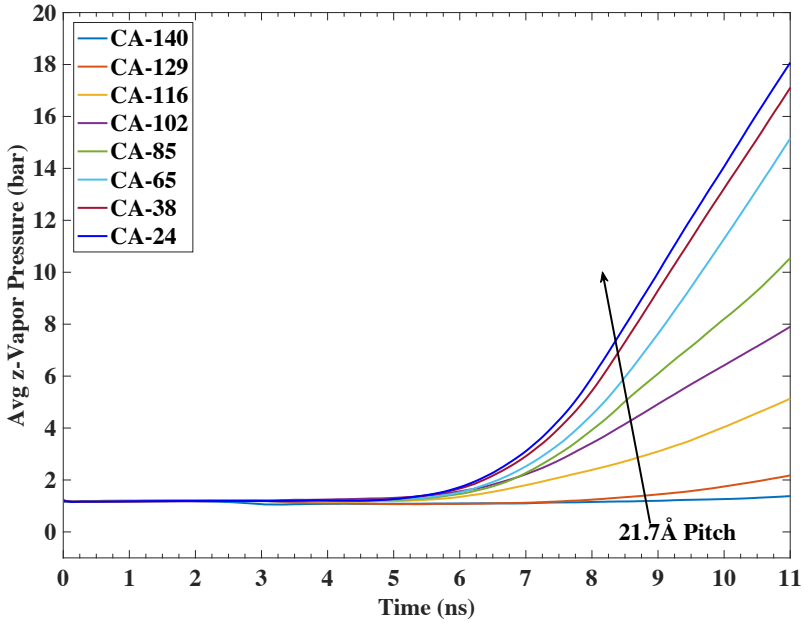

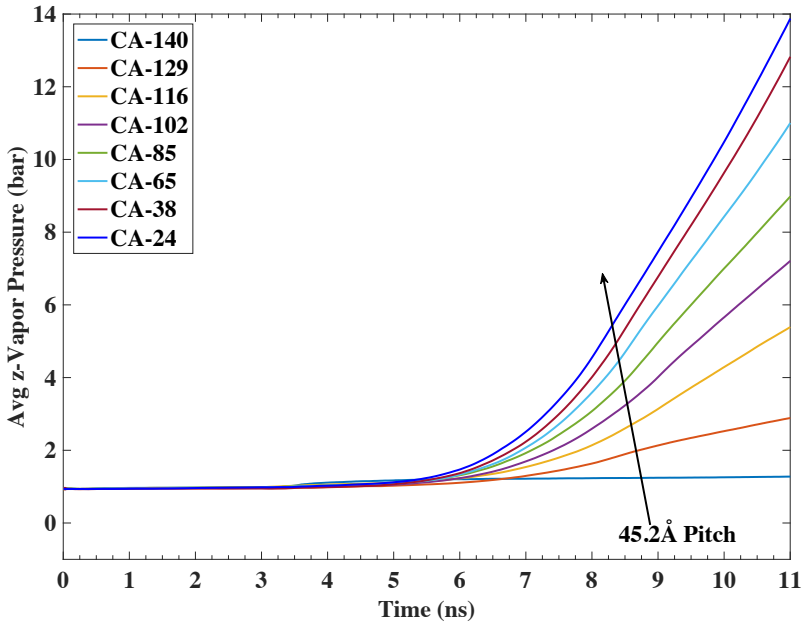

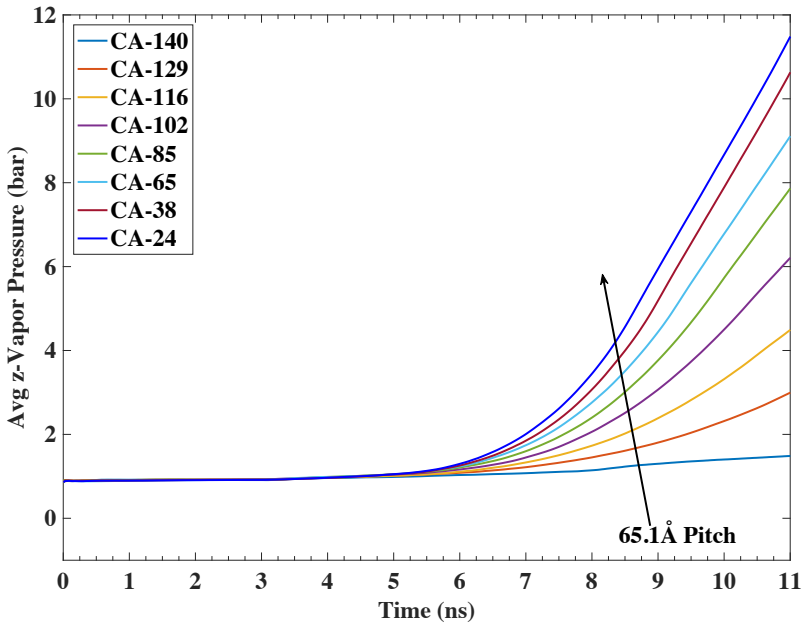
CA-140
CA-129
CA-116
CA-102
CA-85
CA-65
CA-38
CA-24
65.1Å Pitch
Avg z-Vapor Pressure (bar)
Time (ns)
0
2
4
6
8
10
12
0
1
2
3
4
5
6
7
8
9
10
11

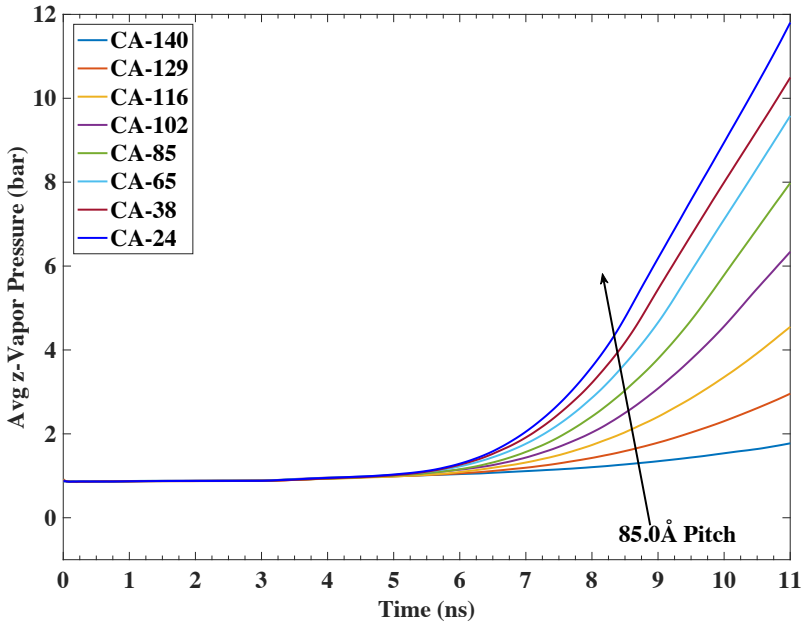
CA-140
CA-129
CA-116
CA-102
CA-85
CA-65
CA-38
CA-24
85.0Å Pitch
Avg z-Vapor Pressure (bar)
Time (ns)
0
2
4
6
8
10
12
0
1
2
3
4
5
6
7
8
9
10
11

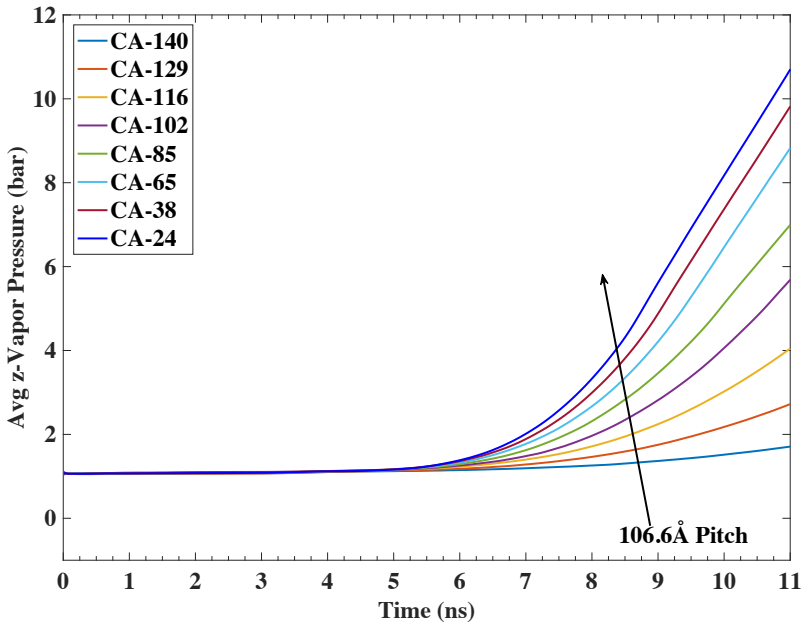

Figure B.1: Ar *z*-vapor pressure evolution.

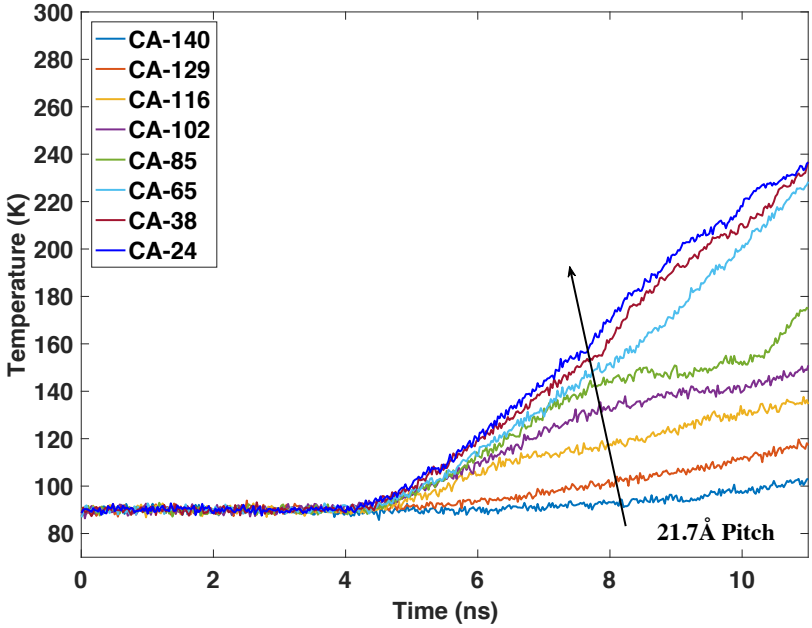
CA-140
CA-129
CA-116
CA-102
CA-85
CA-65
CA-38
CA-24
Temperature (K)
Time (ns)
21.7Å Pitch

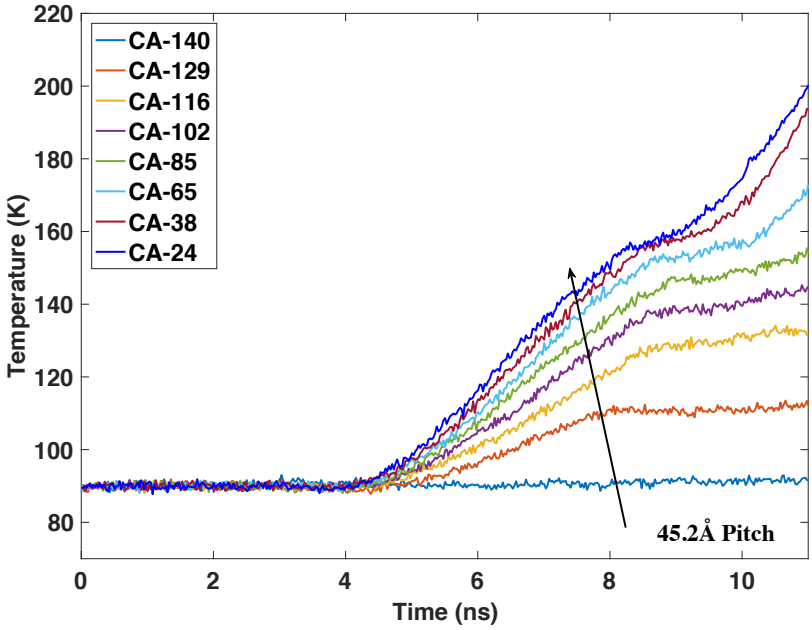
CA-140
CA-129
CA-116
CA-102
CA-85
CA-65
CA-38
CA-24
Temperature (K)
Time (ns)
45.2Å Pitch

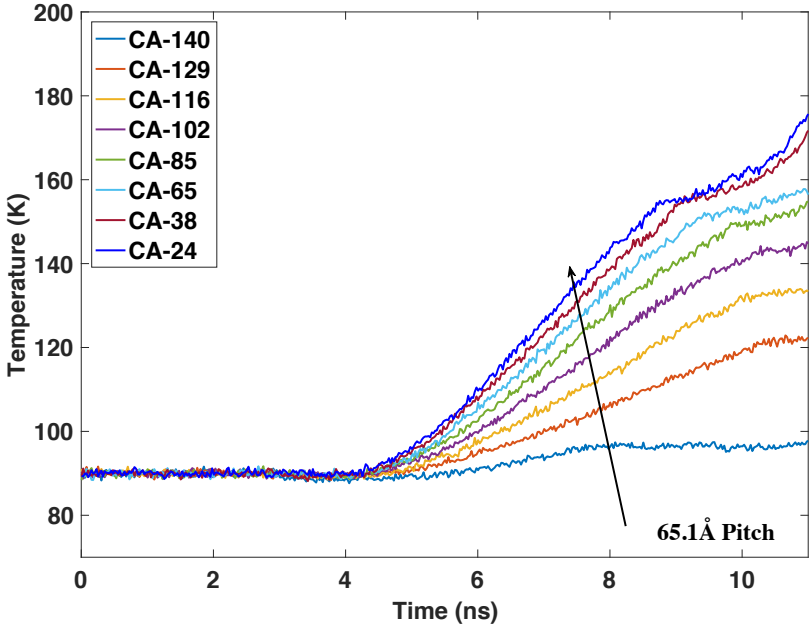
CA-140
CA-129
CA-116
CA-102
CA-85
CA-65
CA-38
CA-24
Temperature (K)
Time (ns)
65.1Å Pitch

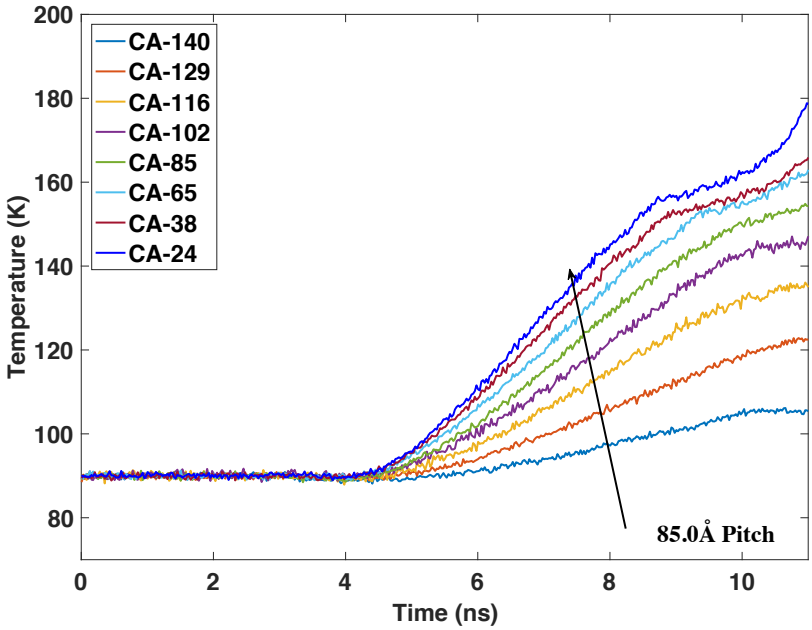
CA-140
CA-129
CA-116
CA-102
CA-85
CA-65
CA-38
CA-24
Temperature (K)
Time (ns)
85.0Å Pitch

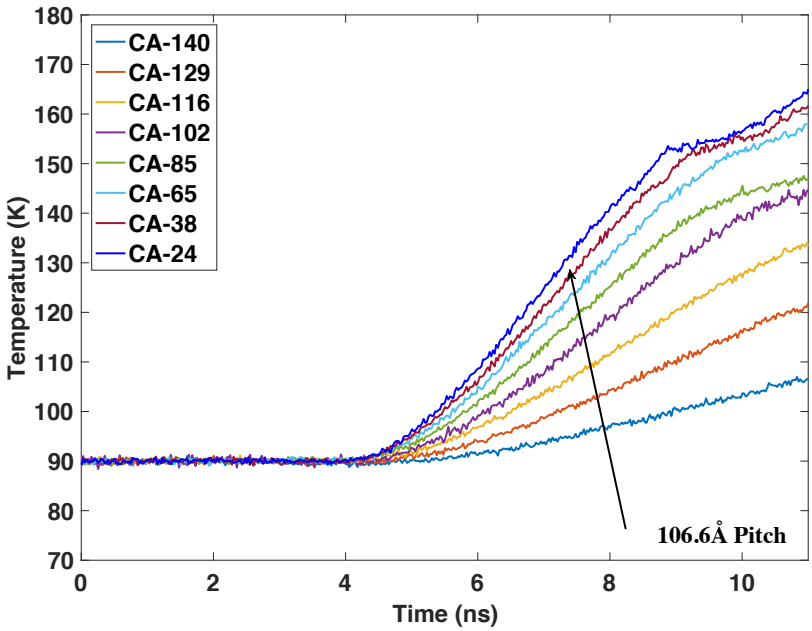

Figure B.2: Ar temperature history.

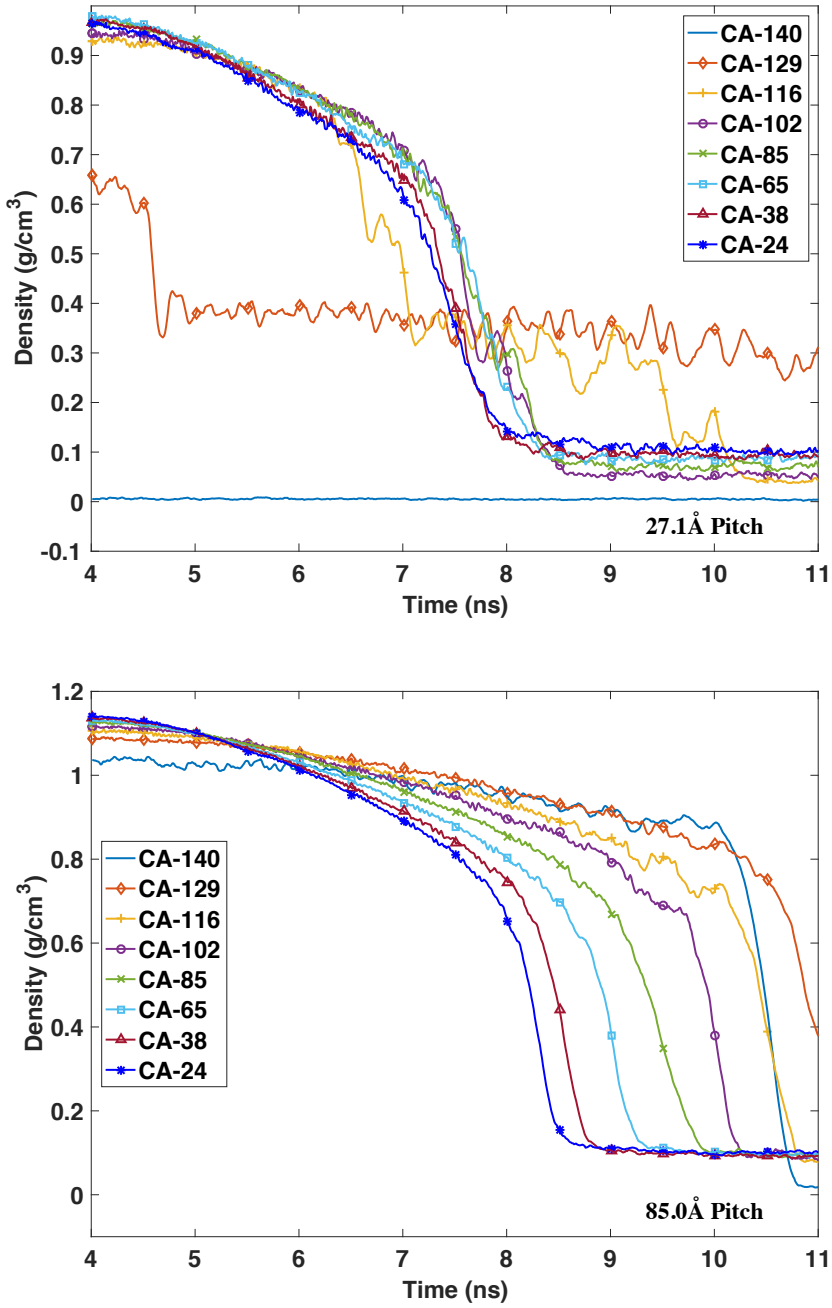

Figure B.3: Phase II density profiles.

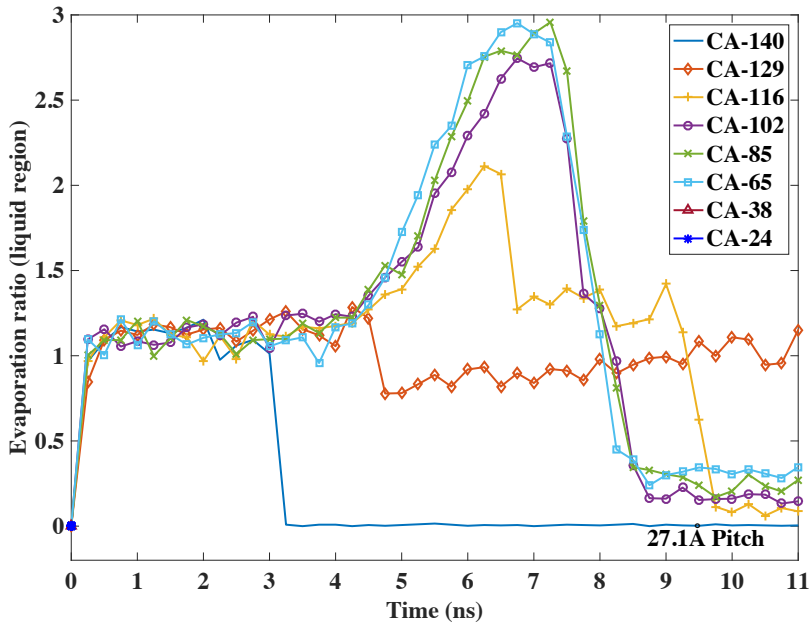
CA-140
CA-129
CA-116
CA-102
CA-85
CA-65
CA-38
CA-24
27.1Å Pitch
Evaporation ratio (liquid region)
Time (ns)

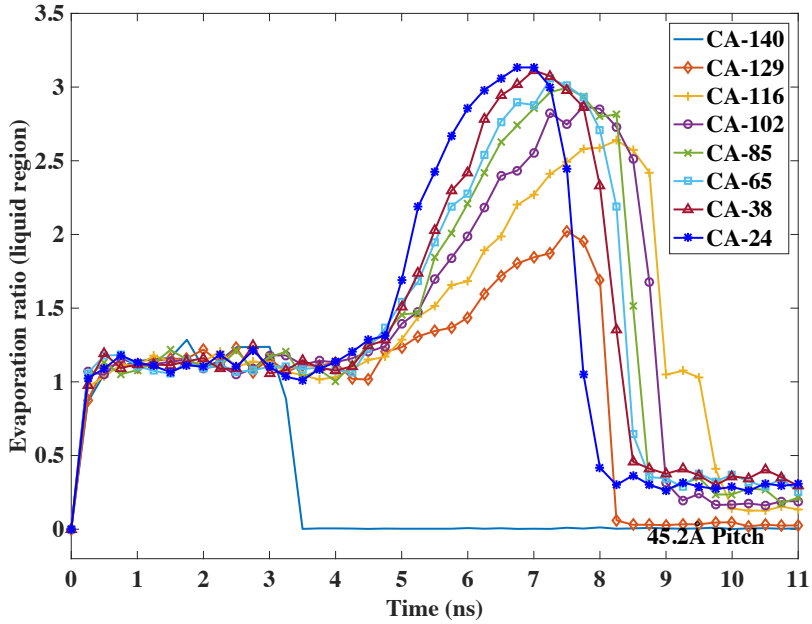
CA-140
CA-129
CA-116
CA-102
CA-85
CA-65
CA-38
CA-24
45.2Å Pitch
Evaporation ratio (liquid region)
Time (ns)

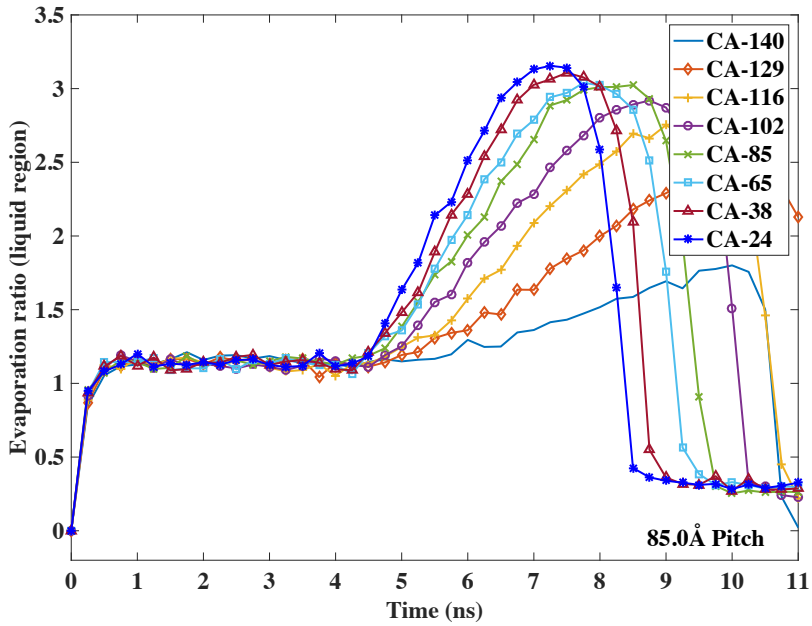

Figure B.4: Evaporation ratio in the liquid region (z<50Å).

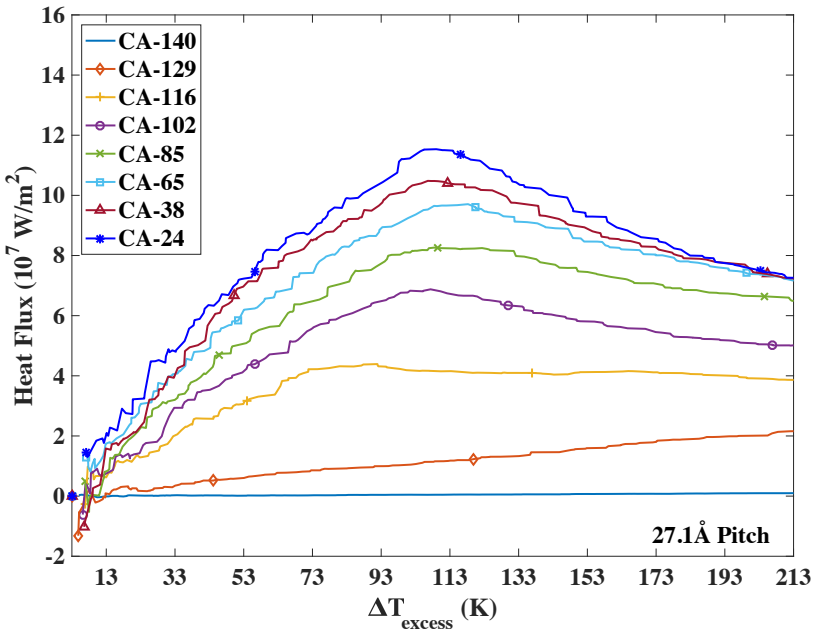
CA-140
CA-129
CA-116
CA-102
CA-85
CA-65
CA-38
CA-24
27.1Å Pitch
Heat Flux (10^7 W/m^2)
ΔT_{excess} (K)
16
14
12
10
8
6
4
2
0
-2
13
33
53
73
93
113
133
153
173
193
213

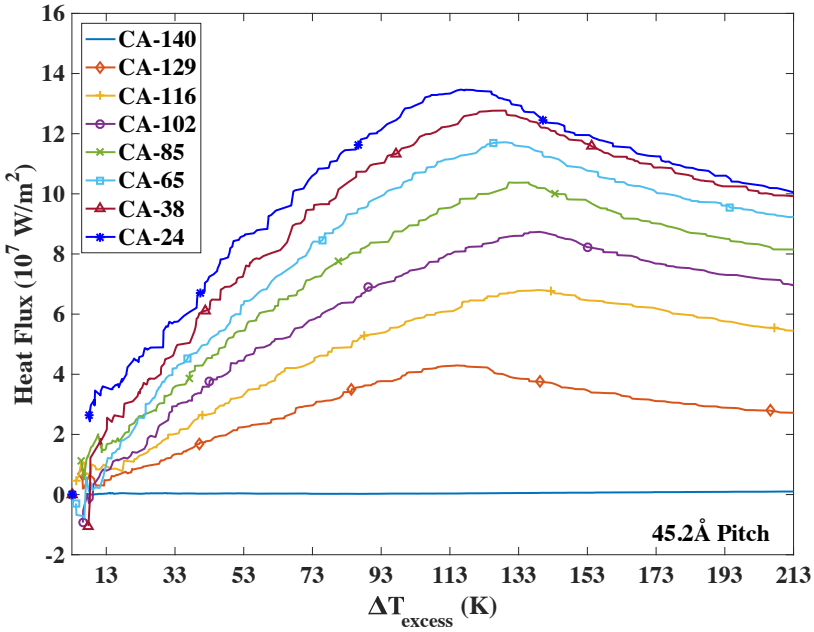
CA-140
CA-129
CA-116
CA-102
CA-85
CA-65
CA-38
CA-24
45.2Å Pitch
Heat Flux (10^7 W/m^2)
ΔT_{excess} (K)
16
14
12
10
8
6
4
2
0
-2
13
33
53
73
93
113
133
153
173
193
213

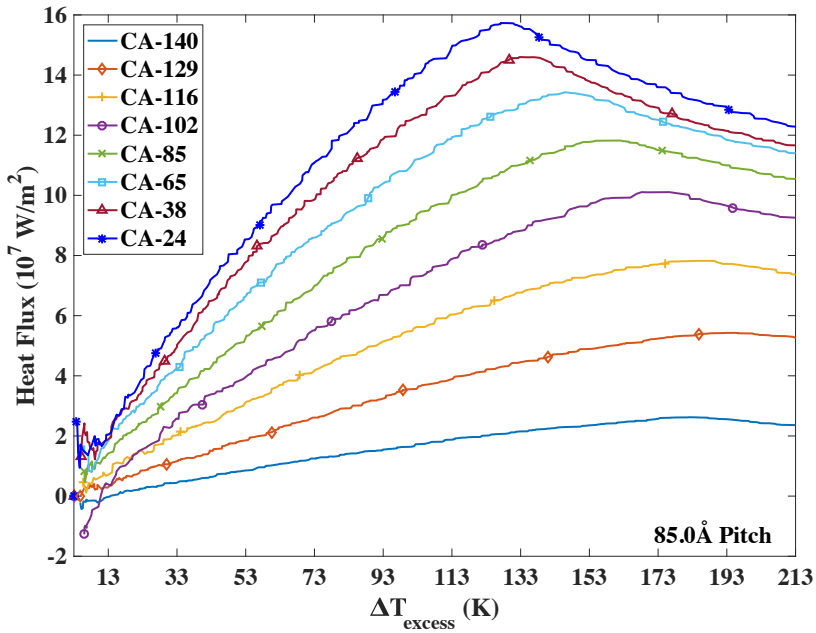

Figure B.5: Boiling curves (Ar heat flux vs. Cu temperature).

Appendix C

Additional Figures for Chapter 5

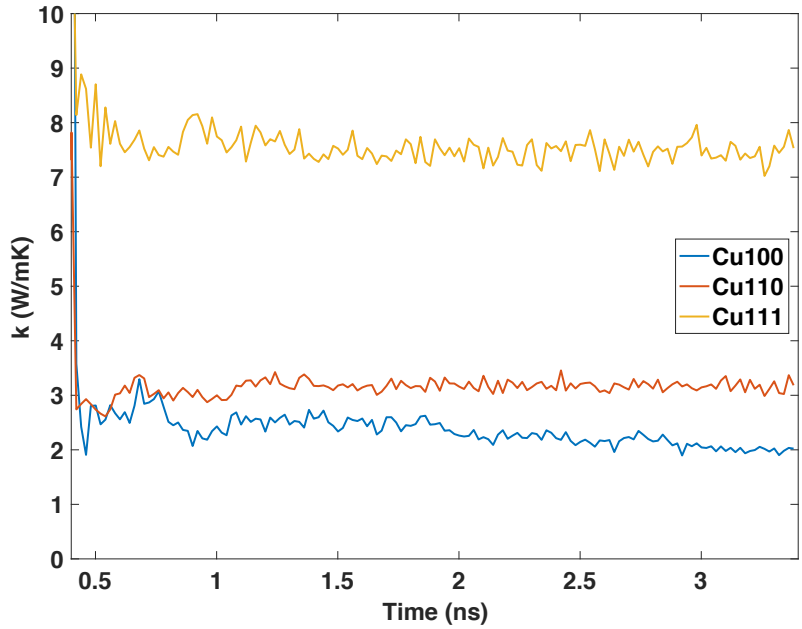

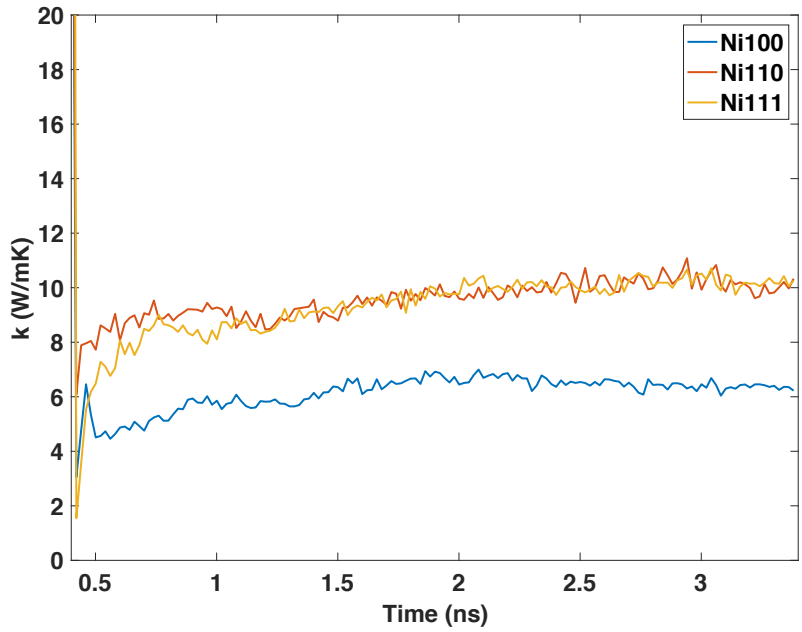

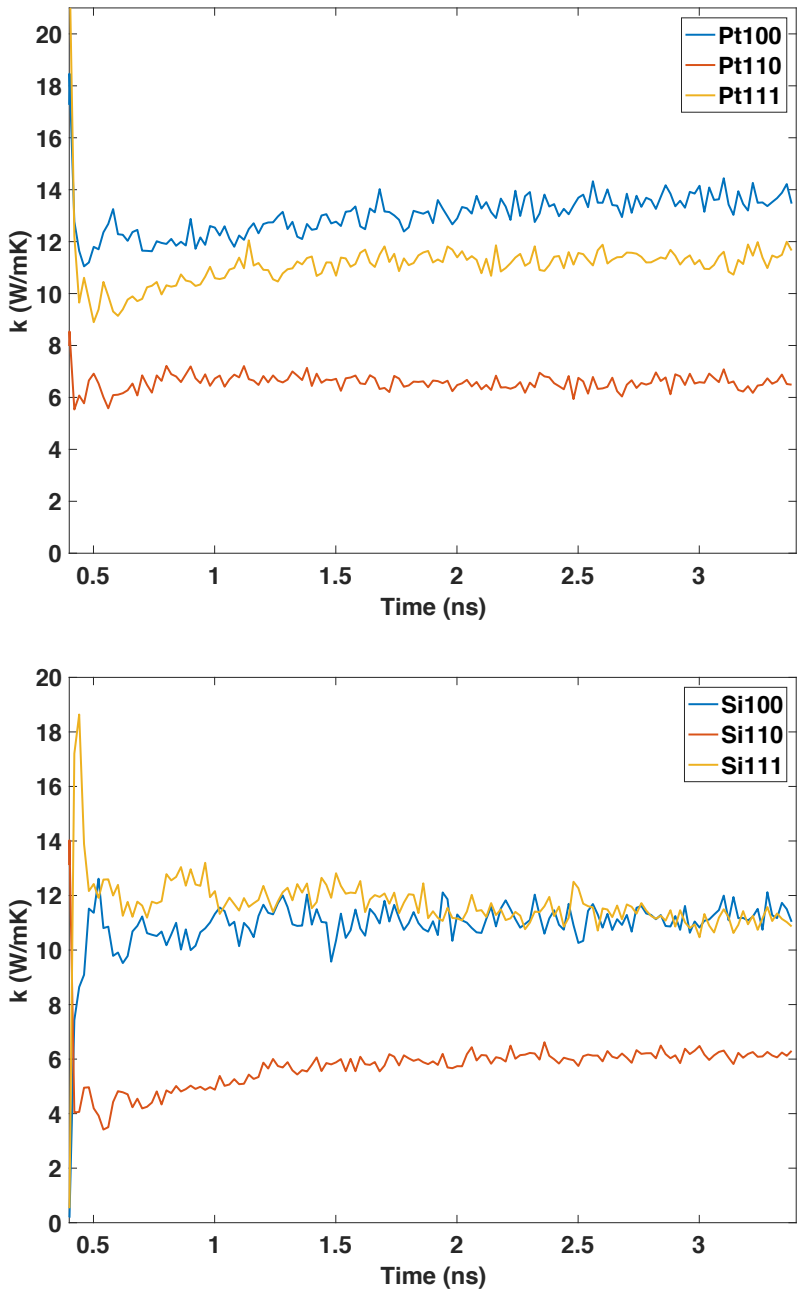

Figure C.1: Transient *z*-direction thermal conductivity profiles for substrates only (without graphene).

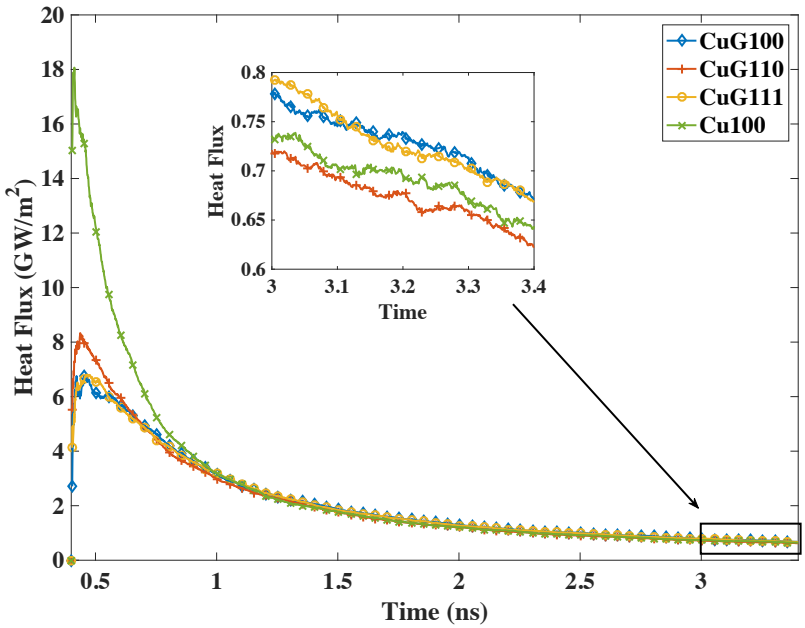
CuG100
CuG110
CuG111
Cu100
Heat Flux (GW/m^2)
Time (ns)
Heat Flux
Time

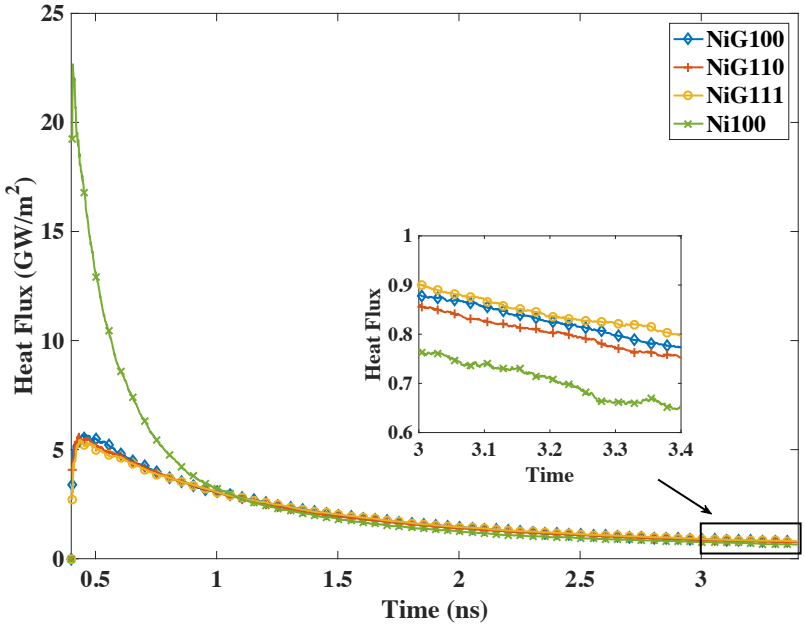
NiG100
NiG110
NiG111
Ni100
Heat Flux (GW/m^2)
Time (ns)
Heat Flux
Time

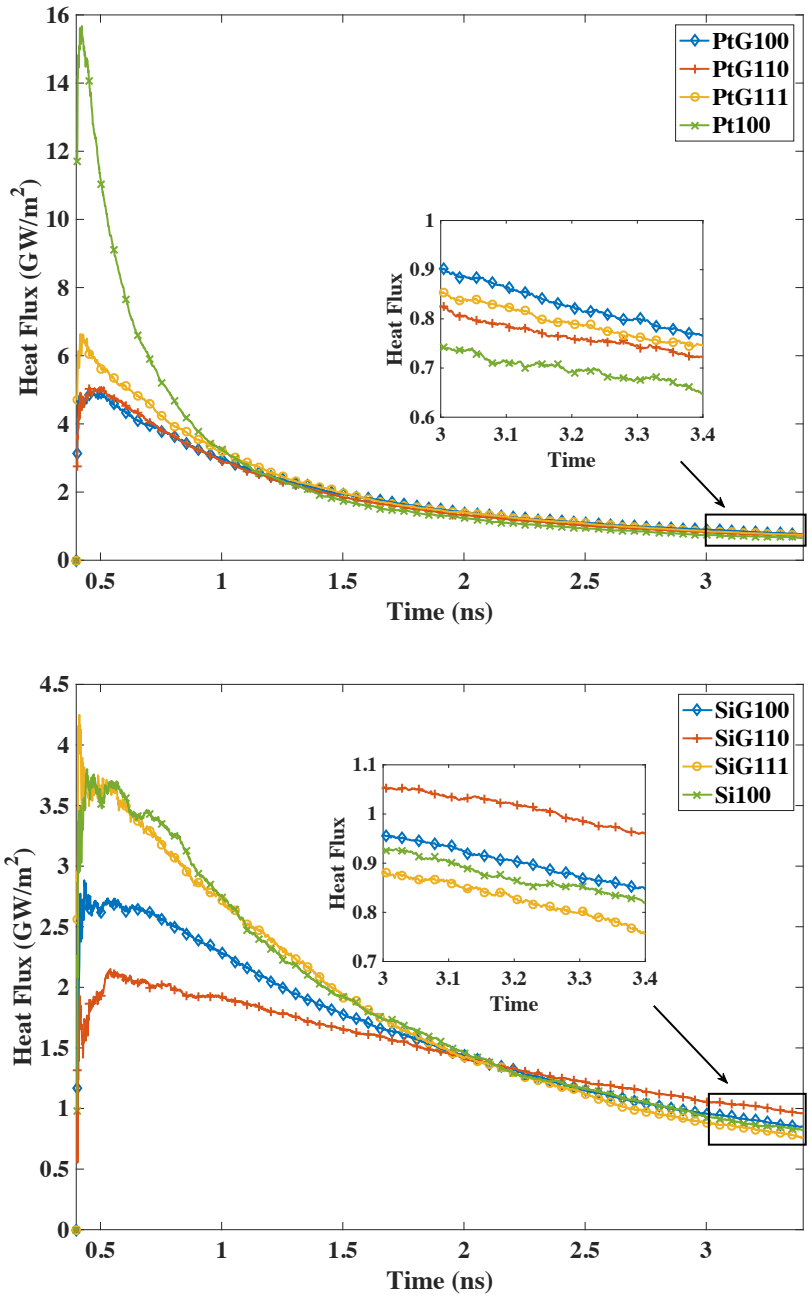

Figure C.2: Time-averaged heat flux profiles.

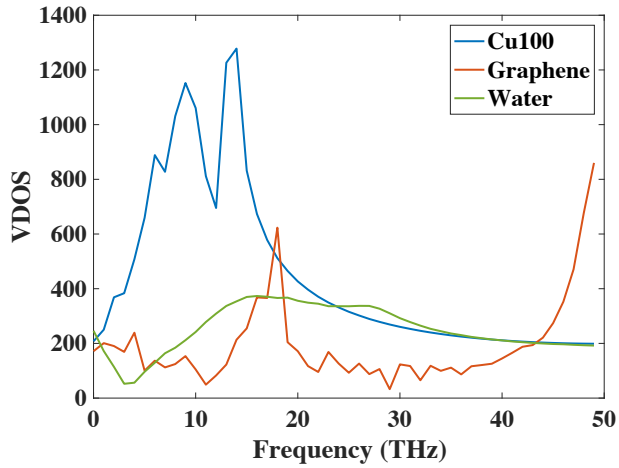
Cu100
Graphene
Water
VDOS
Frequency (THz)
0
200
400
600
800
1000
1200
1400
0
10
20
30
40
50

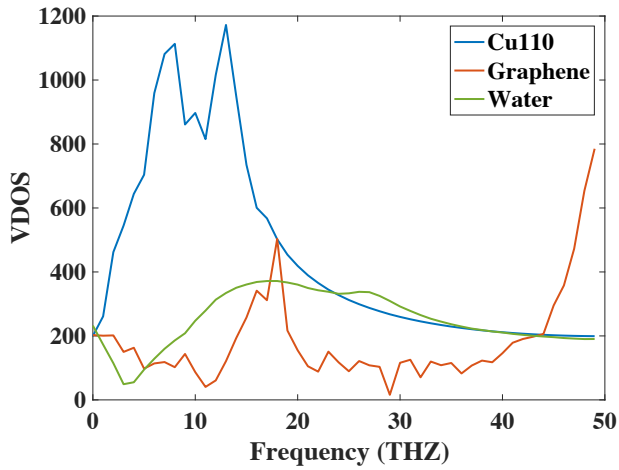
Cu110
Graphene
Water
VDOS
Frequency (THZ)
0
200
400
600
800
1000
1200
0
10
20
30
40
50

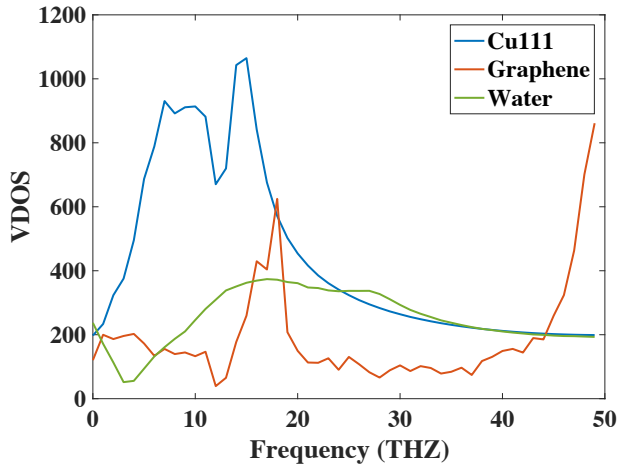
Cu111
Graphene
Water
VDOS
Frequency (THZ)
0
200
400
600
800
1000
1200
0
10
20
30
40
50

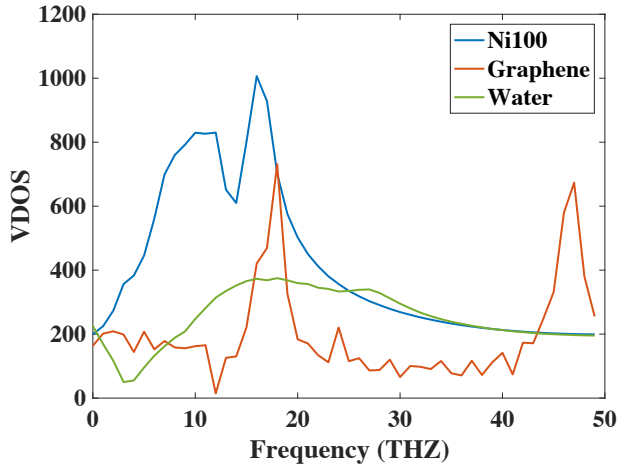
Ni100
Graphene
Water
VDOS
Frequency (THZ)
0
200
400
600
800
1000
1200
0
10
20
30
40
50

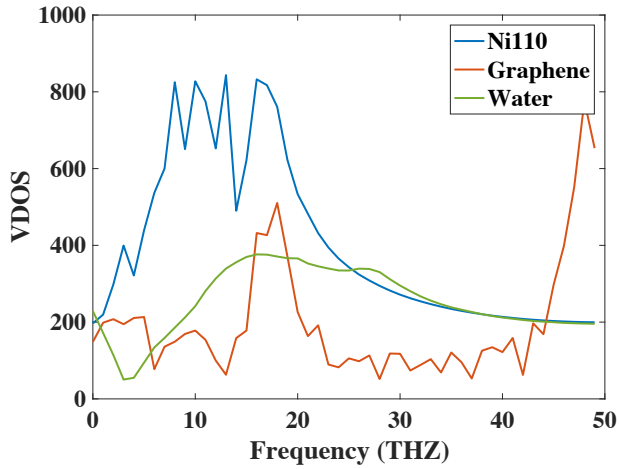
Ni110
Graphene
Water
VDOS
Frequency (THZ)
0
200
400
600
800
1000
0
10
20
30
40
50

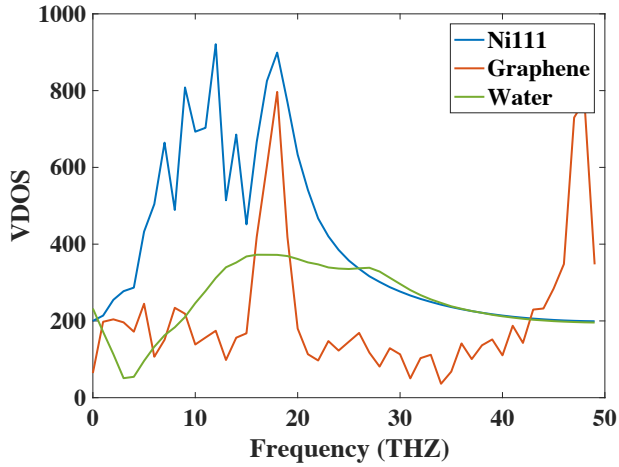
Ni111
Graphene
Water
VDOS
Frequency (THZ)
0
200
400
600
800
1000
0
10
20
30
40
50

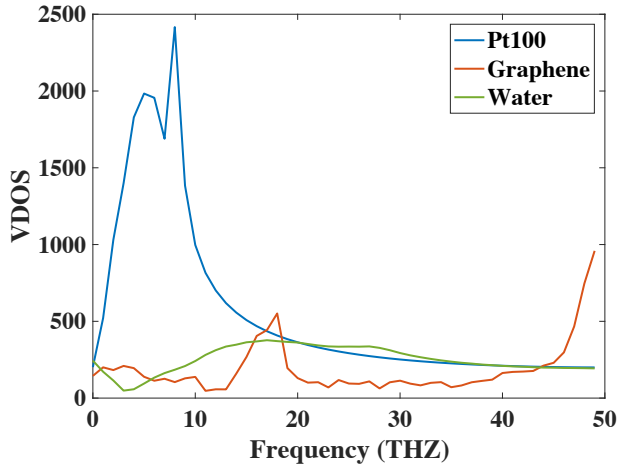
Pt100
Graphene
Water
VDOS
Frequency (THZ)
0
500
1000
1500
2000
2500
0
10
20
30
40
50

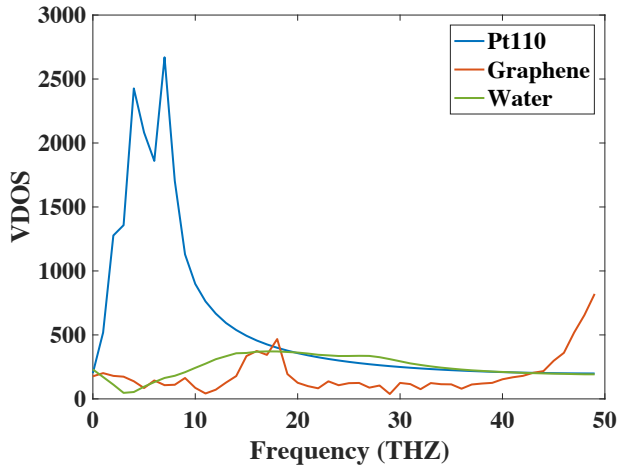
Pt110
Graphene
Water
VDOS
Frequency (THZ)
0
500
1000
1500
2000
2500
3000
0
10
20
30
40
50

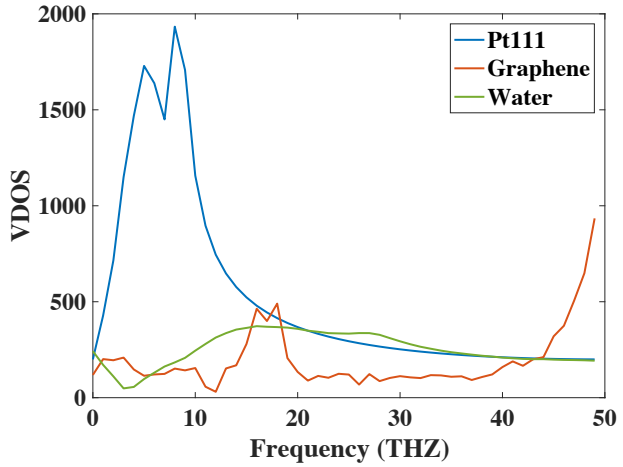
Pt111
Graphene
Water
VDOS
Frequency (THZ)
0
500
1000
1500
2000
0
10
20
30
40
50

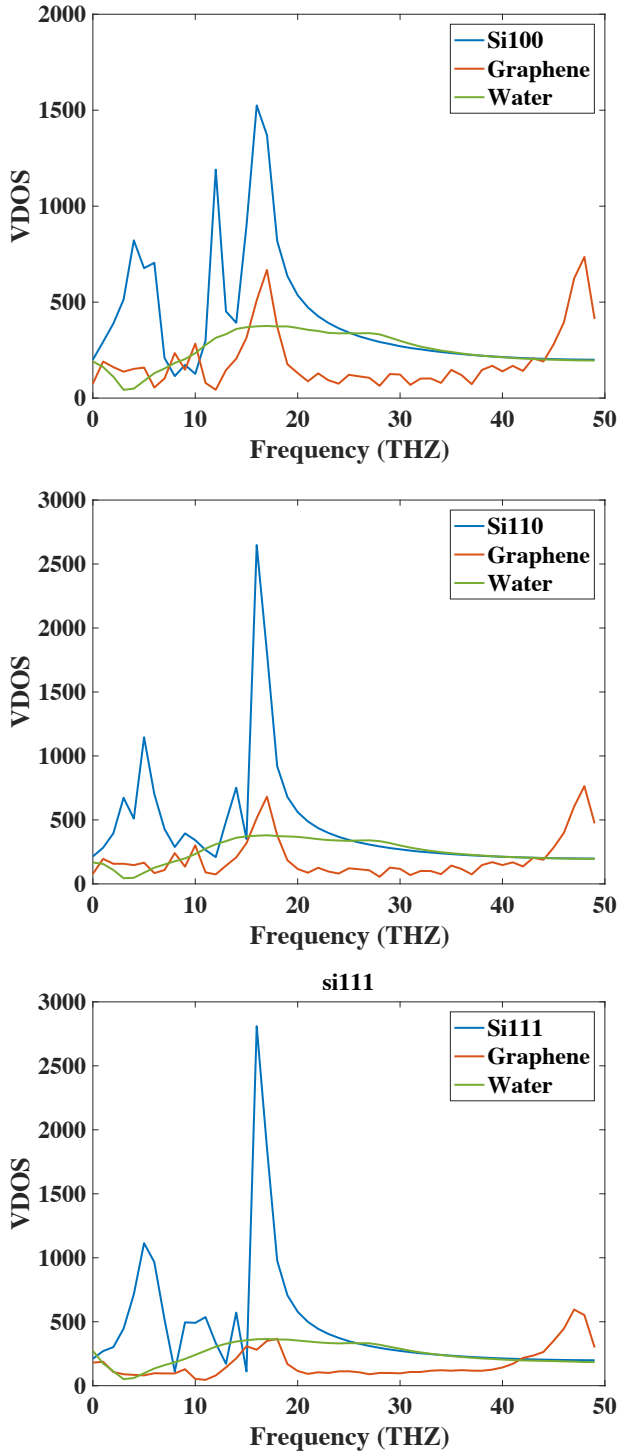

Figure C.3: VDOS profile comparisons of the substrate, graphene, and water.

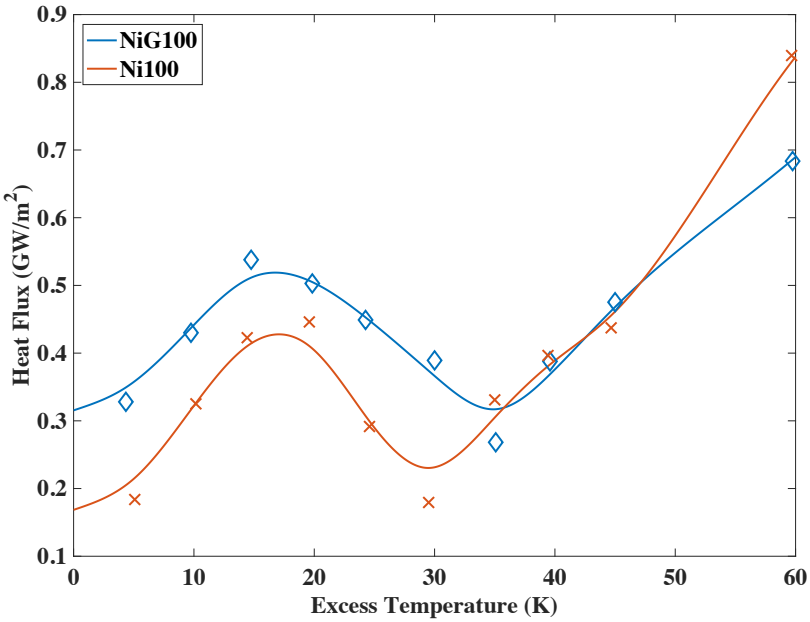

Figure C.4: Boiling curves comparing NiG100 and Ni100.

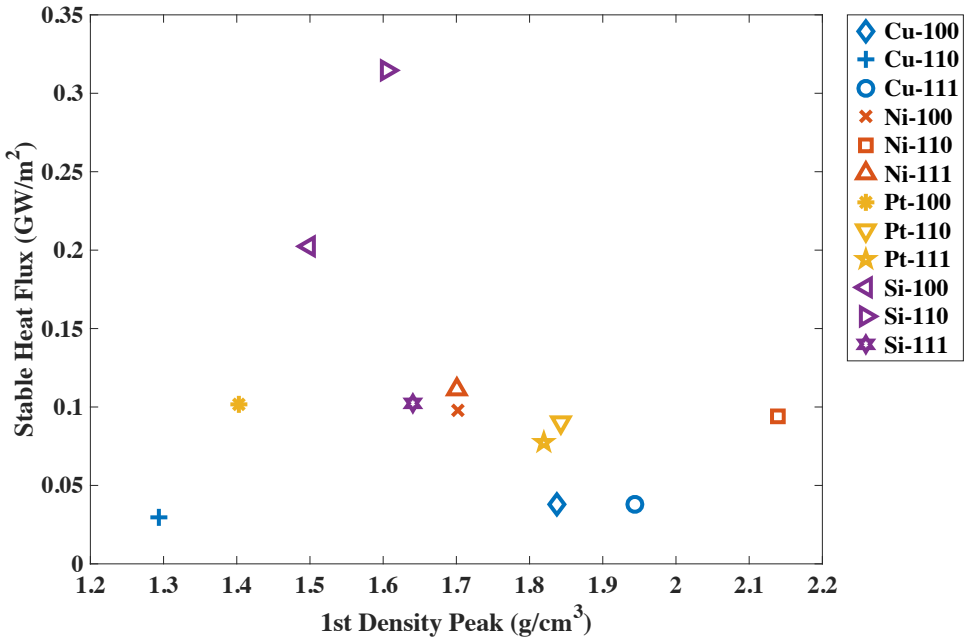

Figure C.5: Heat flux vs 1st density peak comparison.